UNIVERSITY OF OKLAHOMA

GRADUATE COLLEGE

THE EFFECTS OF RANDOM AND CONTROLLED LATERAL CONFINEMENT ON SURFACTANT ADSORPTION

A DISSERTATION

SUBMITTED TO THE GRADUATE FACULTY

in partial fulfillment of the requirements for the

Degree of

DOCTOR OF PHILOSOPHY

By

JOSHUA JACOB WYATT HAMON
Norman, Oklahoma
2018

THE EFFECTS OF RANDOM AND CONTROLLED LATERAL CONFINEMENT ON SURFACTANT ADSORPTION

A DISSERTATION APPROVED FOR THE
SCHOOL OF CHEMICAL, BIOLOGICAL AND MATERIALS ENGINEERING

BY

_____
Dr. Brian Grady, Chair

_____
Dr. Jeffrey Harwell

_____
Dr. Lance Lobban

_____
Dr. Edgar O'Rear

_____
Dr. David Sabatini

Dedicated to my family who has always believed in me

Acknowledgements

There are many people that helped me to get through this doctorate and I will try to acknowledge as many as I can but first, I would like to thank my parents, Brad and Beta, for always pushing me to do more, for helping me make the decisions that led me here, and for their unending support. I couldn't have done it without them and am eternally grateful for everything they've done for me.

A special thanks to my wife, Alyssa, who has been a patient, un-ending source of support and fun since my third day at OU when we met. Love you so much and thank you for putting up with my being easily distracted.

My sister, JoBeth, for making me feel like I can do anything and for always working to make wherever she is a better place.

Jacob Hibbard: For always believing in me, for brotherhood, for being constant, for conversations about books and movies, and for never letting me doubt myself.

My parents-in-law Perry and Kristi Streebin: For home cooked meals and a place to study or escape (depending on the day).

Kevin Carr, without whom the last few years of graduate school would have been a lot less rewarding and not nearly as fun. Thanks for the much-needed distractions and the occasional mid-day movie.

My OU advisor Dr. Brian Grady for giving me an outlet for my passion to design and tinker. He said this project would be difficult and he wasn't wrong, but I enjoyed the challenge and learned much along the way.

Dr. Preston Larson: For the many hours helping me on the SEM, for teaching me, and for interesting conversations.

My OU friends and lab mates Zahra Shahrashoob, Chris Lewis, Danielle Baker, Louis Jackson, and Tara Dinger: Graduate school is tough but you all made it so much better.

My Monash Advisor Dr. Rico Tabor: For allowing me to become a part of the SMaC group, for interesting conversations, and for sharing in my passion to build and tinker.

My housemates on Oliphant: Alex Fuglsang, Annie Thornton, Ebony Knox, and Tom Leigh: Thank you for your friendship, for walks around the neighborhood, for movie nights, for teaching me the proper way of pronouncing banana, and for making me feel at home every day during our time together.

Veena Kelleppan: For being a great friend, including me in the JLA, checking in on me from time to time, and introducing me to the greatness of TimTams and Schnitz chips.

Tom McCoy: For letting me bug you in the lab while waiting for the bus, for showing me how to kick a footie ball, and for believing in me.

Shane Meaney: For listening to me drone on about AFM, for letting me run ideas by you, and for sharing ideas and Python code.

Josh Marlow, Lauren Perillo, Matt Pottage, Ragesh Prathapan, Muthana Ali, Rajiv Thapa, Jackson Moore, Hana Shiraz, Luke Giles, Calum Butler, Josh King and Jesse Givens-Lamb: For making Monash a fun and interesting place and for making sure The Flixy becomes a thing.

Table of Contents

List of Tables

List of Figures

Abstract

The effects of temperature and surface roughness on the mass and viscoelasticity of an adsorbed surfactant layer were monitored using the quartz crystal microbalance with dissipation (QCM-D). Adsorption isotherms at 30, 40, 50 and 60°C and at two different roughnesses on gold were measured for cetyltrimethylammonium bromide (CTAB). All isotherms displayed an increase in mass and dissipation as surfactant concentration was increased to its critical micelle concentration (CMC). Above the CMC adsorption reached a peak followed by a slight decrease to a plateau at the equilibrium adsorption value. As the temperature was increased the adsorbed mass above the CMC decreased. The adsorbed mass decreased further by increasing substrate roughness, while the dissipation remained statistically unchanged. Dynamic adsorption experiments were also conducted at various temperatures for select concentrations above and below the CMC, providing evidence of different adsorption mechanisms as a function of both surfactant concentration and surface roughness.

Force curves collected using an atomic force microscope (AFM) in the presence of adsorbed surfactants are often used to draw conclusions about adsorbed film packing, rigidity and thickness. Force curves were collected from tetradecyltrimethylammonium bromide (TTAB) films adsorbed on highly ordered pyrolytic graphite (HOPG), silica, and silica that had been hydrophobized by functionalization with dichlorodimethyl silane. Break-through events in the force curves from several different trials were compared to show that the break-through distance, often reported as the adsorbed film thickness, increased with concentration below the critical micelle concentration (CMC) but was approximately 3.5 nm on all surfaces between 2× and 10× CMC; an unexpected result

because of the different surface chemistries for the three surfaces. We employed an AFM probe with a different force constant (k) value as well as a colloidal probe and the break-through distance remained approximately 3.5 nm in all cases. Gradient mapping, a variant of force mapping, was also implemented on the three surfaces and resulted in a new technique for visualizing adsorbed surfactant *in situ*. The resulting maps showed patches of adsorbed surfactant below the CMC and revealed that with increasing concentration, the size of the patches increased resulting in full coverage near and above the CMC. These results are, to our knowledge, the first-time force mapping has been used to spatially track patches of adsorbed surfactant. Finally, layers of surfactants on an AFM tip were investigated by collecting a force map on a single AFM tip using the tip of a separate AFM probe. A break-through event was observed between the tips, indicating a layer of surfactant was present on at least one, if not both tips.

Lastly, AFM force curves and nanoscale trenches and pillars were used to investigate the effects of lateral confinement on two cationic surfactants, TTAB and CPC. These laterally confined surfaces are model surfaces for rough surfaces; these surfaces allow for more controlled studies regarding the effect of surface roughness on adsorption. The trenches, formed in a PMMA layer on silica, were 50 nm and 80 nm. Break-through distances, break-through forces and adhesion forces were calculated from the curves on the polymer and on the silica trench floor. For both surfactants, adsorption on the polymer reduced all break-through values. Compared to unconfined values, TTAB in trenches had decreased break-through forces and adhesion forces but CPC forces were unaffected, indicating that surfactant identity could vary the confinement effect. Trench width had no effect on break-through values.

Lateral confinement induced by pillars was studied by noting changes in break-through event values near to the edge of the upper surfaces of pillars. Values decay or increase according to a single exponential with distance from the edge, with decay constants of 12.90 nm±1.84, 14.5 nm± 0.663, and 17.07 nm± 1.227 for the break-through distance, break-through force and adhesion forces, respectively. The break-through distance was found to decrease over its decay length while the break-through force and adhesion force increased. These trends suggest that surfactant layer becomes extended and less mechanically stable due to having to make the ~90° turn between the upper surface and side of the pillar; the former agrees with molecular dynamic simulations. However, decay lengths are much larger than have been found previously in molecular dynamic simulations and we discuss possible reasons for differences

Chapter 1: Introduction

1.1-What are Surfactants?

Surfactants are useful in almost any application where two or more phases meet, such as mineral flotation, regeneration of carbon found in adsorption beds, detergency, oil recovery, de-inking of paper in recycling, cleaning products for in home and industrial use, and many others.[1] Their usefulness stems from being composed of two different regions, typically a hydrophilic headgroup region and a hydrophobic tail group region (demonstrated in Figure 1.).

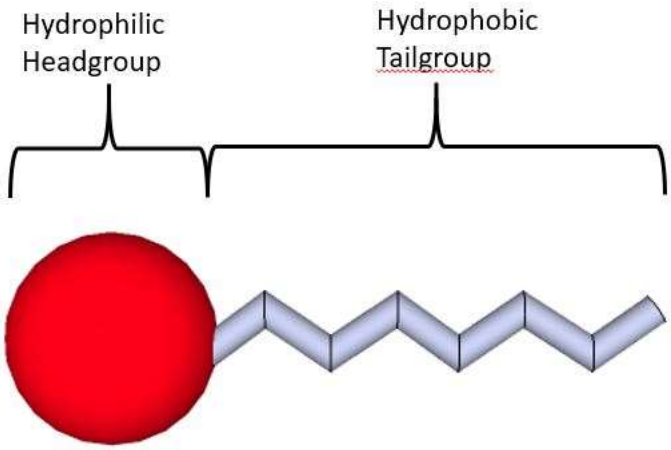

Figure 1. Diagram representing regions of surfactant molecule.

1.1.1-Why Do Surfactants Adsorb at Interfaces?

The hydrophilic nature of the headgroup drives it to be in an aqueous environment while the hydrophobic tail group (normally a carbon chain of varying length) is driven towards non-polar phases (such as air, oils, alkanes, etc.). These competing interactions cause the molecules to diffuse towards interfaces between surfaces and polar/non-polar phases, allowing the molecule to orient so that the

headgroup interacts with hydrophilic surfaces or solvents while the tail group interacts with hydrophobic surfaces, non-polar solvents, or gas phases such as air.

1.1.2-How Are They Classified?

Surfactants are normally classified by their headgroups, which can be ionic, non-ionic, amphoteric, or zwitterionic. Ionic surfactants can have positively charged headgroups (cationic surfactants) or negatively charged headgroups (anionic surfactants). Cationic surfactants will preferentially adsorb to surfaces with negative charges while anionic surfactants will adsorb to surfaces with positive surfaces charges. Non-ionic surfactants tend to have long headgroups made of chains of oligoethylene oxide (EO) groups and will therefore adsorb at surfaces allowing it to make hydrogen bonds.[2,3] Amphoteric surfactants may have a positive or negative charge, depending on the surrounding environment (pH, other ions, etc.), while zwitterionic surfactants have both a positive charge and a negative charge regardless of environment, and can therefore have the properties of both cationic and anionic surfactants.[4]

1.2-How Do They Act in Liquids?

1.2.1-CMC-Micelles

Surfactants will form 3 dimensional structures called micelles when the surfactant concentration in the bulk liquid exceeds a specific concentration, known as the critical micelle concentration (CMC), which varies depending on the surfactant. While there are many factors that can influence the CMC, such as temperature, ionic strength, and pH, a general rule is that as the surfactant hydrocarbon tail length increases, the CMC of the surfactant decreases.[5]

1.2.2-Why Surfactants Form Micelles (Entropic Interactions)

The reason for the decrease in CMC with increasing chain length and indeed why surfactants form micelles at all is a result of the hydrophobic nature of the tail groups and their interaction with water. Taking a simple example of a cationic surfactant in water, an entropic driving force is generated by water molecules surrounding the tail group. More specifically, the water molecules surrounding the tail are in an unfavorable environment (polar/non-polar interaction) and therefore form an ordered cage-like structure.[2] If the tail groups are moved closer together, the water molecules are expelled into the surrounding liquid, releasing them from the ordered state of the cage, and they are now free to take on more random configurations and positions, thereby increasing their entropy and making micelle formation entropically favorable.[5]

1.2.3-Critical Packing Parameter

Depending on the nature of the liquid and the dimensions of the surfactant molecules a variety of micelle shapes can be formed, including spherical, cylindrical, flexible lamellar (vesicles), planar lamellar, and inverted (reverse) micelles. The type of micelle morphology can be roughly predicted using the critical packing parameter (CPP), which is calculated using Equation 1

$$CPP = \frac{V}{A * l}$$

Equation 1. Critical Packing Parameter

where V is the tail group volume, A is the headgroup area and l is the tail group length. The headgroup area, however, is not fixed and can change due to variation in solution temperature, ionic strength, as well as other factors.[6]

1.2.4-How is the CMC Measured?

The CMC can be measured in a variety of ways but one of the most common is to measure the liquid-gas interfacial tension (the strength of lateral intermolecular forces at the interface) as a function of concentration of surfactant in the liquid.[7] As the concentration of surfactant in solution is increased, more and more surfactant molecules will accumulate at the interface and cause a subsequent decrease (normally linear when plotted against the log of surfactant concentration) in the interfacial surface tension. This decrease occurs because the surfactant at the interface reduces molecular packing of the liquid caused by the interface. As the concentration approaches the CMC micelles begin to form in solution and any additional surfactant will add to or form new micelles. This causes the concentration of free surfactant monomers at the interface as well as the concentration of free surfactant monomers in solution, to remain relatively unchanged even if more surfactant is added to the solution. -Researchers take advantage of this to measure the CMC by determining the

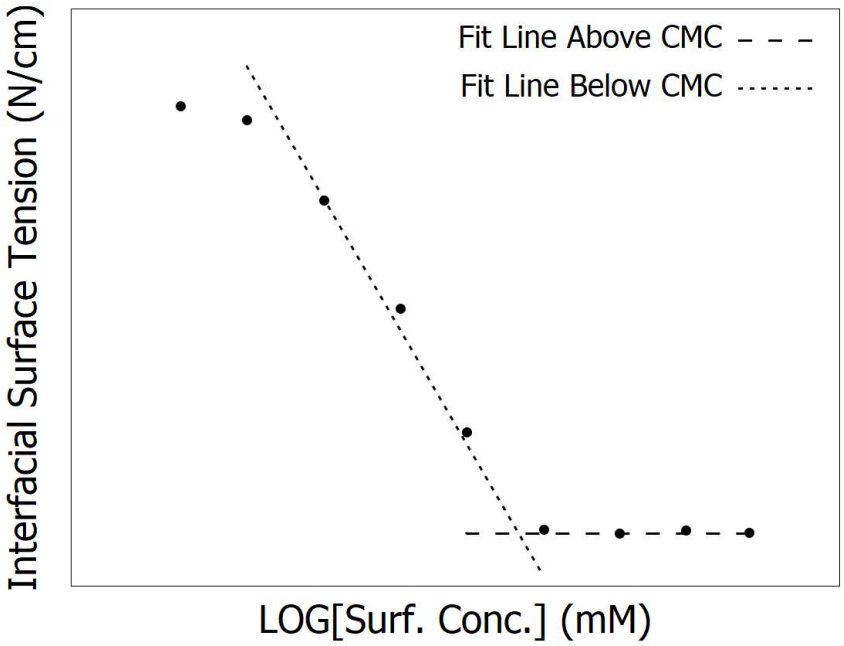

Figure 2. IFT vs. log(surfactant concentration). Fit lines show intersection which denotes critical micelle concentration.

intersection between the decreasing line below the CMC and the constant line above the CMC, demonstrated in Figure 2.

1.3-How Do surfactants Adsorb at Solid-Liquid Interfaces?

Entropy is also an important factor in considering adsorption of surfactant at a solid-liquid interface from water. However, the energetic interaction between the surface and the surfactant can also play a role. Adsorption at a solid interface is controlled by several factors, including the electrostatic nature of the surfactant head group, hydrophobic chain length, branching of the hydrophobic chain, temperature, characteristics of the solid (i.e. roughness, surface charge, etc.) and the characteristics of the solvent (polarity, chemical additives, pH, etc.).[8-12]

1.3.1-Methods Used to Measure Adsorption

Techniques to measure adsorption on a solid include gravimetric analysis such as the quartz crystal microbalance (QCM)[10,13-16], reflectivity (neutron reflectivity, optical reflectometry, ellipsometry)[17,18], surface or interfacial tension (dynamic contact angle, drop shape analysis, bubble pressure tensiometry)[19], electrostatics (zeta potential)[20,21], force interaction (atomic force microscopy, surface force apparatus)[22,23] , and a variety of other methods.

1.3.2-Regions of Adsorption

Adsorbed surfactant amount per unit of surface area is normally plotted vs. log concentration to obtain an adsorption isotherm. The dominant driving force for surfactant adsorption depends on concentration and is normally explained by separating the isotherm into different regions based on concentration ranges. [1,5]

The first region, Region I, begins at low concentrations where surfactant adsorption has been found to increase linearly following Henry's Law. The driving force in this region is dominated by interactions between the charges on the headgroup and the charges on the surface. Region II is denoted by a sharp increase in adsorption, caused by entropic effects (water molecules being freed as previously discussed). Surfactant aggregates on the surface begin to form, referred to as surface aggregates or hemi-micelles. The rate of adsorption in Region III is marked by a decrease in the rate of adsorption with increasing concentration relative to Region II and continues to decrease up to Region IV, normally beginning at or near the surfactant CMC, where a plateau in adsorption is found. In some cases, a maximum in adsorption at the CMC has also been found, followed by a decrease to a plateau. This maximum is due to impurities in solution adsorbing along with the surfactant molecules, which partition into the aggregates on the surface. Once the concentration in the bulk solution is capable of supporting micelles, impurities desorb from the surface aggregates and the amount adsorbed now only represents the surfactant adsorbed without the desorbed impurities.[24]

1.3.3-Surfactant Aggregates on Solids

Surfactant surface aggregates have been found on surfaces at concentrations lower than the CMC.[25] The six most common aggregates found on surfaces are demonstrated in Figure 3. They are the flat monolayer, the hemisphere, and the hemicylinder on hydrophobic surfaces and the flat bilayer, full sphere and full cylinder on hydrophilic surfaces.[25-29] In general, what determines whether a monolayer or bilayer structure is formed is the wettability of the surface (hydrophobic or hydrophilic respectively). The particular shape is driven primarily by the packing factor, although the interaction between the surfactant and the surface can also play a role. The driving force for surface aggregation is the same as the force that causes micelles to form in solution, the increase in the entropy of the system when ordered water molecules are released from a cage-like structure.

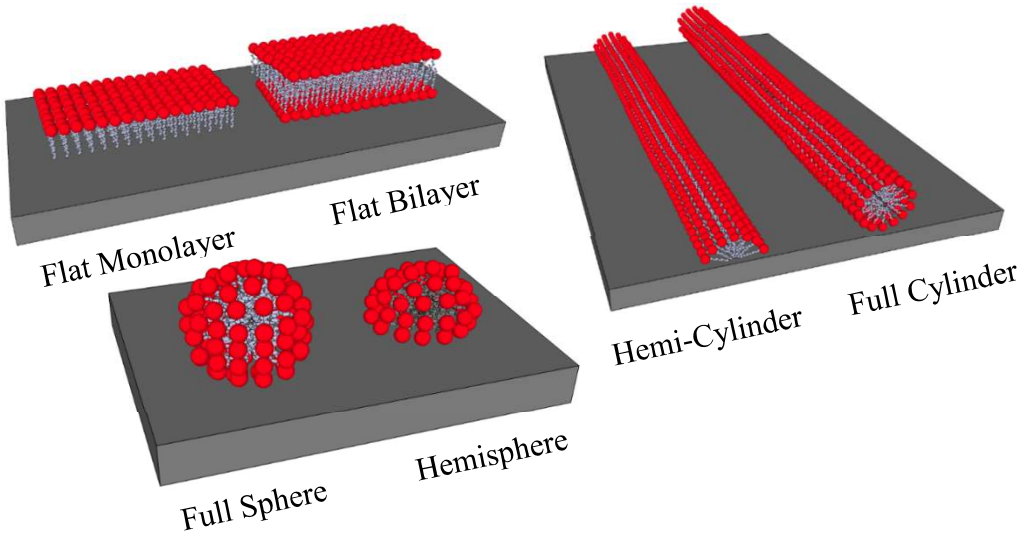

Figure 3. Six possible surfactant surface aggregate morphologies.

1.3.4-Change in Wettability

Obviously, tail-tail interactions (or more precisely, releasing water from a cage-like structure) plays a substantial role in the aggregation and adsorption of surfactants.

Due to the hydrophobic nature of the surfactant tail groups they will preferentially interact with hydrophobic surfaces, such as highly ordered pyrolytic graphite (HOPG), and will therefore adsorb in a "tail-down" configuration, leaving the headgroups pointed outwards towards the bulk solution. This type of adsorption leads to a change in the apparent wettability of the surface, because although the surface was hydrophobic there is now a layer of headgroups exposed to the surroundings causing the surface to act as a hydrophilic surface. This wettability change can also be controlled using the charge on the surfactant and the charge on the surface. In some cases, anionic surfactants will adsorb on negatively charged surfaces in a tail-down configuration to change the charge strength of the negatively-charged hydrophilic surface.

In cases where the surfactant is oppositely charged from the hydrophilic surface or the surfactant hydrophile is uncharged, the surfactant will adsorb "head-down". However, because a layer of surfactant adsorbed head-down would leave the hydrophobic tail groups exposed to the solution, a second layer of surfactant adsorbs tail-down to the first layer, interdigitating their tail groups with the tail groups of the first layer and exposing the headgroups of the second layer to the bulk solution. The "tail-tail" interactions of these two layers segregate the tail groups from the water and allow the hydrophilic interaction between the headgroup and the bulk solution.

Altering the wettability of a surface has large implications in areas such as oil recovery and surface cleaning. Wettability is usually measured and reported as the angle that a drop of liquid, normally water, forms on the surface at the point of contact. High contact angles (>90°) are taken as hydrophobic while low contact angles are taken as hydrophilic. For a surfactant-based cleaning method to remove liquid from a surface it

must increase the contact angle between the soil and the surface to which it clings. Surfactants facilitate this increase by adsorbing at the interface between the surface and the water as well as at the interface between the oil and the surface. This action lowers the interfacial tension between the surface and the oil and enables the "roll-up" of the oil from the surface and sequestration into micelles, allowing the oil to be washed away.[4,5,25,30]

1.3.5-How Does Temperature Affect Adsorption to Surfaces?

The effect of temperature on surfactant adsorption has been studied in the literature. These studies show that for ionic surfactants the adsorption process is exothermic.[31-34] Several published works discuss the inverse temperature dependence of ionic surfactants, i.e. as the temperature is increased the maximum equilibrium adsorption for ionic surfactants decreases.[1,12,32,34-40] This behavior is thought to be caused by an increase in the entropy loss upon adsorption at high temperatures, caused by the higher entropy of the surfactants in solution vs. the adsorbed species.[1,34,37,41]

In terms of experiments at different temperatures, the Krafft temperature and the CMC changes are both important to consider. The Krafft temperature is the temperature at which surfactant solubility matches the CMC.[42] The Krafft temperature of aqueous CTAB lies between 20°C and 25°C, and varies because of the presence of other compounds or contaminants in solution.[42-44]

1.3.6-How Does the Surface Roughness Affect Adsorption?

Typically, what one thinks of as surface roughness can be thought of as random lateral confinement, with variations in the size and shape of the area available for surfactants to adsorb. Studies using ellipsometry, quartz-crystal microbalance (QCM),

and atomic force microscopy (AFM) have demonstrated that increasing roughness can decrease the final amount adsorbed at equilibrium and alter the final surfactant morphology on various surfaces like gold and silica.[10,13,14,17,28,45,46]

Regular (or controlled) lateral confinement has been investigated primarily using simulations, where the surfaces can be confined on surfaces with dimensions on the order of a few surfactant molecule lengths. Work performed by Tummala et al. showed that the aggregate morphology of surfactant adsorbed on carbon nanotubes was dependent on the diameter of the nanotube, which agreed with neutron reflectivity experiments.[47] Tummala also investigated surfactant adsorption on graphene nano-sheets and nano-ribbons, which showed that as the diameter of the graphene decreased the effects of the lateral confinement became more pronounced, specifically at the edges of the confined area where the headgroups of the adsorbed surfactant oriented themselves radially towards solution.[48]

Simulations by Suttipong et al. were performed using trenches of varying depth, which demonstrated that the morphology of the aggregates adsorbed within the trench varied with trench depth and in some cases multiple morphologies could form within the same trench.[49] Also, when the floor of the trench was changed to a surfactant repellant material, the morphology of the aggregates closest to the floor shifted to accommodate the new, less optimal interactions. Suttipong et al. then performed simulations involving surfactant adsorption to stripes and steps, which had varying widths and heights, respectively.[50] On stripes, decreasing the width led to an increase in both the curvature of the aggregates and the density of head groups at the stripe edges. On steps, the edges were noted to cause the surfactant layer to be deformed, thinned

(less dense), and stretched as it traversed from the upper surface to the sides. However, if the height of the step was increased it was found that the surfactant layer would not adsorb to the upper surface of the step to avoid an energy penalty associated with bending the layer from the side to the upper surface. These findings agree with the conclusion drawn by Tummala, in that the effects of confinement appeared to be most apparent at the edges of confining structures. However, any effects beyond a few surfactant lengths (~7 nm) were not observed.

The effects of lateral confinement were observed experimentally at much larger distances in the work of Marquez et al., who used nanosphere lithography on highly-ordered pyrolytic graphite and template assisted admicellar polymerization to create nanostructures with polystyrene nanospheres of different sizes, inducing confinement both laterally and vertically.[51] Continuous honeycomb structures formed when using spheres larger than 500 nm while smaller spheres yielded discontinuous spikes; in all cases the polymer film was not completely filling the interstitial void space. A simple geometric argument revealed that the polymer-sphere separation distance varied between 4 nm and 250 nm, depending on nanoparticle size. By contrast, adsorbing polymer will completely fill the interstitial spaces up to the thickness of the polymer film. Surface roughness can affect surfactant adsorption by disrupting the interaction between tail groups in the adsorbed film. The increase in the thickness of the adsorbed layer has been shown via ellipsometry. Because surfactants are used in many surface-based applications, understanding how roughness affects adsorption is an important area of research. Studies have been performed using QCM, ellipsometry, AFM, and other apparatus to show that when the roughness of a surface changes the surfactant aggregate

morphology, amount adsorbed and packing of the film can change. The question is what is it about a rough surface that causes these changes?

1.4-The Purpose of This Investigation and Hypothesis

This work proposes to add to the understanding of how surface roughness affects surfactant adsorption. First, the effects of temperature and random lateral confinement were simultaneously investigated using the quartz crystal microbalance with dissipation (QCM-D) using the cationic surfactant CTAB on gold.

Then, atomic force microscopy (AFM) force mapping was used to gather break-through distance, break-through force, and adhesion force values using different surfaces, AFM probes, surfactant concentrations, and surfactant introduction methods. The precise meaning of the break-through distance as measured by AFM was then investigated and compared to the trends observed in the break-through force and adhesion force values, and the utility of AFM in collecting and analyzing this and other properties is reviewed.

Lastly, the force mapping methods developed in the previous section were used to investigate the effects of controlled lateral confinement, induced using nano-scale trenches and pillars, with the cationic surfactant TTAB on silica.

Based on the data presented in the literature, we hypothesize that the surface roughness will lead to a change in the amount of surfactant adsorbed and an increase in the thickness of the adsorbed layer, which was observed previously in simulation and neutron reflectivity studies. We also hypothesize a change in the morphology of the surfactant aggregates, as was observed visually in AFM studies.

What follows in this section is a brief introduction to the primary equipment used in this investigation: a quartz crystal microbalance and an atomic force microscope. More details are found in Appendices B and C respectively.

1.5-Quartz Crystal Microbalance

The quartz crystal microbalance with dissipation (QCM-D) has proven to be a useful tool for probing the mechanics of surfactant adsorption on a variety of surfaces at different temperatures and concentrations and by collecting this information over time the rate of adsorption can also be investigated.[1,10,40] This apparatus has two key advantages over previous methods: (1) its versatility and (2) the acquisition of viscoelastic data. Although QCM-D cannot be used to determine the exact structures of adsorbed molecules, the viscoelastic information collected from dissipation data has been correlated to the basic morphology of the adsorbed films.[10,52]

1.5.1-QCM Surfaces

Under ambient conditions, gold surfaces are made hydrophobic by the physisorption of organics.[53] However, the gold substrates used in our experiments have been found to have a surface that is primarily hydrophilic, as measured by both contact angle and x-ray photoelectron spectroscopy, a surface type which has been shown to induce CTAB and TTAB adsorption in the form of cylindrical aggregates.[54-56] Other studies have shown that gold and various other hydrophobic surfaces have supported the formation of bilayer films characteristic of a hydrophilic surface, although in some cases this was done purposefully by the addition of co-solutes.[13,17,57] The hydrophilic nature of the surface used in our experiments was found to be caused by the high concentration of oxygenated sites and the adsorption of halide ions, which have been

reported previously by ours and other groups to create a negative charge on the surface.[10,58,59] The gold surface provided by the manufacturer displays hydrophilic character even on the uncleaned surface, although further oxygenation and hydrophilicity is caused by the recommended cleaning procedure (RCA-1 solution), which has been shown to increase the hydrophilicity of silicon as well.[13,60-62]

1.5.2-QCM Roughness

Several publications reported the difference between QCM-D and optical methods for measuring the amount of surfactant adsorbed from bulk solutions.[14,59,62,63] Although QCM has been found to report higher adsorbed masses than optical methods, there is some debate as to whether solvent entrapped in the adsorbed layer is the cause. Macakova et al. hypothesized that entrapped solvent, specifically "hydration" solvent surrounding the surfactant head groups, was negligible when the cationic surfactants CTAB and two closely related analogues were used, but solvent trapped in the cavities caused by surface roughness (mechanically trapped) must be considered. The presence of trapped water had no effect on the dissipation of adsorbed layers unless the organization of the surfactant layer on the surface of the substrate changes.[14] Our group postulated that the over-estimation of the adsorbed mass sensed by QCM-D is not caused solely by trapped solvent, but also by a difference between the roughness of the surfaces used by QCM and other techniques which causes a significant underestimation of the surface area available for adsorption.[13] Our hypothesis stems from the fact that the typical substrates used in optical methods are extremely smooth when compared to those used in QCM experiments, as assessed by root-mean square roughness measurements, and therefore by using the nominal (non-roughness corrected) surface

area there would appear to be a greater amount adsorbed per unit area, leading to the misconception of entrapped solvent.[64] Following our interpretation, when the roughness corrected surface area was used, the mass adsorbed per unit area actually decreased vs. a smooth surface.[10,14,65]

Surface roughness could cause other phenomena as well. For example, Fragneto et al. found that CTAB formed a bilayer on both smooth and rough silicon surfaces, but that the surfactant film on the rough surface displayed an increase in the bilayer thickness and a decrease in surface coverage and degree of packing between adjacent surfactant molecules when compared to the smooth surface.[17] These and other surface roughness effects are attributed to the disruption of the hydrophobic interactions between surfactant tails which reduces their ability to exclude water, as well as a decrease in the number of surface sites favorable to adsorption.[10,13,17,66]

1.6-Atomic Force Microscopy

The use of the atomic force microscope (AFM) in surfactant research has helped make significant contributions to the understanding of adsorbed surfactant morphologies, dimensions, and orientation. Of specific interest to this study are soft contact imaging and force curves that are used to explore the characteristics of adsorbed surfactant layers.[26,27,67-69]

Early seminal papers in AFM studies of adsorbed surfactants concerned surfactants adsorbed on highly-ordered pyrolytic graphite (HOPG) explored by Manne et al.[23,70] These studies were possible due to the production of an electrical double-layer (EDL) at the surface generated by the surfactants and counter ions adsorbed to the surface. This type of imaging, known as “soft contact imaging”, is accomplished by

increasing the force applied by the AFM tip until it begins to register a response due to the presence of the adsorbed micelle layer. At this point, any lateral variations in the morphology of the aggregates become distinct. These variations are used to determine the morphology of the adsorbed surfactant aggregates before the tip breaks through the layer and images the underlying substrate. However, this technique lacks accurate information regarding the surfactant layer in the z-direction because the probe does not contact the surface beneath the surfactant during imaging. Therefore, the initial publication of Manne et al. included a force vs. distance curve and a thorough explanation of the details of such curves, which was necessary to achieve the required mechanical stability over the adsorbed surfactant necessary for sustained imaging.

Others have imaged surfactants and supported lipid bilayers adsorbed on a variety of substrates using soft contact imaging and force curves with a spectrum of pH, ionic strengths, and temperatures.[26,28,71-75] The force curves initially used to determine the required force for imaging are now also used to study other aspects of the surface and adsorbed species, such as the stability and electrostatic nature of the adsorbed surfactant and lipid layers.[23,28,46,76,77] Typical properties obtained from force curves are the break-through force, break-through distance, and adhesion force. The break-through force is the force at which the probe will penetrate the micelle layer to the underlying substrate during scanning and is manifested as an instability point in the force curve. The break-through distance is the distance between this instability and the point of contact with the underlying surface, and is often taken to represent the thickness of the adsorbed film.[26,29,65,69,73,75,77-81] However, this assumption is questionable since compression is occurring during the measurement, and some have assumed that the

distance where the force curve deviates from zero is a more accurate representation of the adsorbed film thickness.[28] The number of publications which utilize the break-through distance as well as the much higher degree of accuracy in the automated determination of the instability point was the reason that the break-through distance is investigated here. Lastly, the adhesion force is the force required to pull the AFM tip off the surface during retraction of the probe.

These properties (although primarily the break-through force) were used by Pera, Franz, Butt, Loi, and others to develop and test theories related to the energetic interactions between the approaching AFM tip and an adsorbed lipid DOTAP or DOPS layer.[78,82-84] The events leading to the instability are thought to start at the point the AFM tip begins to interact with the repulsive portion of the EDL, giving the curve its initial exponential increase with decreasing separation. At a certain distance the tip physically contacts the micelle layer; with increasing force surfactant is displaced from beneath the tip, and the film ruptures. Künneke et al. expanded on these studies and correlated topography, stiffness, and the adhesion force, and did so using the enhanced data collection method known as pulsed force mode (PFM), which increased the speed at which force curves could be collected.[74]

The histogram-based analysis implemented by these and other authors has since been used with several different adsorbed layers of lipids and surfactants, including cetyltrimethylammonium bromide (CTAB), tetradecyltrimethylammonium bromide (TTAB), sodium dodecylsulfate (SDS), and biological lipid layers with varying pH, concentrations of added surfactant and tail lengths.[75,77,79,85-87] From this short overview it is clear that many investigations use the break-through and adhesion forces primarily,

while the break-through distance values are commented on but are less used in analysis. If these distance values are mentioned or shown in force curves, they are often very similar (normally around 3.5-4 nm), even for different surfactants or concentrations, and there has yet to be a substantial investigation into their comparability and physical origin.[26,65,75,77-80]

As the prevalence of combination instruments implementing AFM continues to grow (e.g. combination AFM/ellipsometer and AFM/quartz crystal microbalance), the use of force curves to verify thickness models could become more and more useful, making the determination and understanding of the break-through distance more necessary. However, there seems to be some discrepancy in the literature as to whether force curves obtained on adsorbed layers includes some compression distance prior to the instability point and whether the AFM tip used during force curve collection is 'naked', in the sense that adsorbed layer thicknesses can be found without considering if there is surfactant adsorbed on the tip. In fact, there have been few in-depth studies performed to determine the effects of the tip or probe used to collect the force curves as opposed to the number of studies that make use of break-through events.

Chapter 2: Materials and Methods

2.1-QCM Investigation of Random Lateral Confinement and Temperature

Cetyltrimethylammonium bromide was purchased from Sigma Aldrich at approximately 99% purity. CTAB was purified by re-crystallization three times in HPLC grade ethanol to remove impurities before using it to prepare a 15 mM stock solution with Milli-Q H_2O (18 MΩ cm), purified using an arrangement of Milli-Q ion-exchange and activated carbon filters. Surfactant solutions were diluted in glass vials, which were previously cleaned in sulfuric acid containing Nochromix©.

2.1.1-CMC Determination

The CMC of CTAB was measured at various temperatures using a Mettler Toledo Seven Multi conductivity meter and plotting specific conductivity vs. concentration to find the break point in the slope.[88-90] The CMC data, shown in Table 1,

Temperature (°C)	CTAB CMC (mM)	Error (mM)
30	0.93	0.03
40	1.02	0.07
50	1.15	0.11
60	1.33	0.13

Table 1. CMC of CTAB measured at various temperatures

report the value and fitting error collected from the specific conductivity method and agree well with values found in literature.[89,91] As shown in Table 1, an increase in bulk solution temperature led to a modest increase in the CMC for CTAB in water as expected due to a decrease in the entropic driving force of micellization as temperature increases, as described in more detail in Chapter 1.

2.1.2-QCM-D Crystals

Quartz crystals were purchased from Q-Sense. Smooth crystals (termed smooth but as will be shown are not molecularly smooth) (QSX 301) are layered with ~100 nm of gold and have a nominal frequency of 5 MHz. A set of specially prepared rough crystals (QSX 999 Au Rough) with the same nominal frequency were also purchased.

2.1.3-Roughness Characterization

Roughness measurements on the crystal surfaces were performed with the Agilent 5420 Atomic Force Microscope. Images were obtained in air using the NSC15/ALBS silicon nitride cantilevers from MicroMasch, with a force constant of 46 N/m , a resonant frequency of 325 kHz, and a normal aspect ratio. Scan sizes were 2 μm x 2 μm and the pixel resolution was 512×512 pixels, taken at scan frequencies < 1 Hz. Root-mean square (RMS) roughness values are reported as the average for 3 independent areas on either a single smooth or rough crystal. The reported RMS data are averaged over two similar crystals and the error reported for each crystal below was found as the standard deviation. Before undergoing any washing procedures, the RMS roughness of the smooth crystals was found to be 0.9±0.07 nm using the program Pico Image, which agrees well with the manufacturer's reported value of 0.9 ± 0.2 nm. [92] Following the cleaning procedure the roughness of the smooth crystal had increased to 2.13 ±0.19 nm. The rough crystals (QSX 999 Au) had an RMS value of 5.72 ± 0.16 nm before the cleaning protocol; following a cleaning procedure the roughness increased to 6.17 ± 0.23 nm. The roughness increase following cleaning is likely due to the RCA solution attacking high energy sites on the surface of the crystal more than the low

energy sites causing the creation of additional "peaks and valleys" and creating a rougher surface with each washing.

All data presented in this paper were obtained assuming the nominal, not the actual surface areas of the sensing elements. Previously an RMS of 5.8 nm was considered to represent a surface area of 10.12 μm^2 (compared to a nominal 4 μm^2), using a fractal approach to calculate the surface area based on roughness measurements.[10]

2.1.4-Cleaning Procedures

QCM-D crystal washing protocols are divided into smooth and rough crystal sections for clarity, although both procedures follow similar steps.

2.1.4.1-Smooth Crystals

Crystals were used a maximum of four times because adsorption did not change significantly during the four runs; in a few cases crystals gave results very different than the results from the previous trial; in this case the crystal was discarded even if four runs had not been completed. The crystals were placed in a Harrick Plasma Cleaner (PDC-32G) and cleaned using the medium setting (10.5 W applied to RF coil) in air for 10 minutes. The crystals were then transferred to a Q-Sense sensor Teflon© holder and immersed in an 80°C RCA-1 cleaning solution (1:1:5 solution of NH_4OH:H_2O_2: Milli-Q H_2O) for 5 minutes.[60,61,93] The sensors were removed from the solution and rinsed individually with Milli-Q H_2O and dried under a nitrogen stream. The crystals were then immediately moved to the plasma cleaner for 5 minutes on the low setting (6.8 W applied to RF coil). Finally, the sensors were moved from the plasma cleaner directly into a QCM module for immediate measurement.

2.1.4.2-Rough Crystals

Rough crystals were removed from the box and placed directly into an RCA-1 cleaning solution at 80°C for 5 minutes. Afterwards the crystals were removed and individually rinsed and dried using the same procedure employed on the smooth crystals. They were then placed into a fresh RCA-1 solution at 80°C for another 5 minutes, then rinsed and dried. This procedure was repeated once more before placing the crystals in their modules as in the smooth crystal procedure. Rough crystals were only used once because the adsorption changed with subsequent cleanings. No plasma cleaning was performed on the rough crystals as it was found to alter the crystal surface area.[10]

2.1.5-QCM-D Data Collection and Experimental Protocol

The interpretation of QCM data is explained extensively in the literature.[15,52,62-64] During our measurements we observed that the data gathered from the first and third overtones for the oscillation frequency were routinely erratic and therefore were discarded; the 5^{th}- 13^{th} overtones were used to determine mass and dissipation values. Changes in mass adsorbed and dissipation were measured for CTAB at, 30° C, 40° C, 50° C, and 60° C using the Q-sense E4 microbalance. The temperature was controlled within ±0.05°C of the desired setpoint.

A peristaltic pump using Tygon© tubing was used to draw surfactant solutions through Teflon© tubing into the modules at a rate of 0.1 mL/min. At the beginning of each experiment the cleaned sensors were placed in their modules and pure Milli-Q water was used to obtain stable baseline frequency and dissipation values, (noted by a change in frequency of less than 0.03 Hz/min). The pump flow direction was toggled

periodically during equilibration to dislodge bubbles that sometimes formed on the crystal and tubing surfaces.

Once a stable baseline was acquired, the pump was stopped long enough to remove the tubing from the pure water and immediately placed in the vial containing a CTAB solution. Just prior to injection, each new concentration increment was sonicated for 10 minutes and then heated to within 5°C of the desired temperature, while being sparged with helium to remove dissolved gas.

In one set of measurements, adsorption isotherms were measured. During each isotherm the surfactant concentration was increased in increments of 0.1×CMC of CTAB until 0.6×CMC was reached. From there the concentration was increased by 0.2×CMC up to a bulk concentration of 2.0×CMC and then increased in one step to a bulk concentration of 2.5×CMC. All QCM measurements are susceptible to drift over time, which can introduce error and make the determination of equilibrium difficult. Equilibrium was considered achieved when the change in frequency for all crystals fell within 0.03 Hz/min.[92] The time needed to reach equilibrium ranged from 15-20 minutes for the higher concentrations to 30-45 minutes for the lowest concentrations. After equilibrium was reached, a new concentration was drawn through the apparatus by stopping the pump and moving the tubing as described above.

In separate kinetic experiments, mass adsorbed on gold as a function of time was recorded. In these experiments, the bulk concentration was increased from zero directly to the desired final concentration, without intermediate steps. A space-time calculation was used to determine when the surfactant solution was actually introduced into the QCM module and that time was set to zero in all graphs. The residence time of a QCM

cell was calculated to be roughly 25 seconds using the QCM module volume of 40 µl above the crystal and the volumetric flow rate. The slopes of adsorption in the different regions were averaged over four crystals in the smooth surface trials and two crystals in the rough surface trials.

At the end of an experiment, a 2% sodium dodecylsulfate solution was drawn through the tubing and modules for 1 hour followed by pure water for 3 hours, to remove adsorbed CTAB from the tubing and crystal surfaces. Subsequent experiments showed stable baselines with pure water, indicating adequate removal of any residual surfactant from the equipment.[57,93]

2.2-AFM Force Curve Characterization of Adsorbed Surfactant on Flat Surfaces

2.2.1-Surfactant Preparation

Tetradecyltrimethylammonium bromide (TTAB) was obtained from Sigma-Aldrich and recrystallized three times from ethanol before use. The CMC was found to be 3.52±0.43 mM using pendant drop shape analysis. No minimum was detected in surface tension, which indicates a relatively pure surfactant. This surfactant was used over the more commonly studied CTAB due to a lower Krafft point (0°C for TTAB versus ~23°C for CTAB), which made working around room temperature less likely to induce a phase change.[43]

2.2.2-AFM Probes and Probe Cleaning

Two types of probes were used throughout the investigation: PPP-BSI (NanoAndMore), standard silicon, and MSCT "f" probe (Bruker), silicon nitride. The PPP-BSI probe had a nominal force constant of 0.1 N/m, a resonant frequency of

28 kHz and tip radius of less than 10 nm (normal aspect ratio) and the MSCT probe "f" had a nominal force constant of 0.6 N/m, resonant frequency of 125 kHz, and tip radius of 10 nm (normal aspect ratio). Prior to use, the probes were cleaned in a UV Ozone chamber for 30 minutes.

2.2.3-Colloidal Probe Preparation

The colloidal probe, which was an AFM probe with a spherical glass bead on the end, was prepared by first taking a clean microscope slide and applying a small drop of UV curing glue and using a disposable needle to create glue streaks that were thinner than the initial drop. Around 25 mm away on the same side of the same microscope slide, a small quantity of glass beads (Polysciences, Inc.) were added by quickly inverting and righting the closed bottle containing the beads, removing the cap and tapping it on the glass slide. This procedure provided an array of separated glass beads from which to choose. A PPP-BSI AFM probe was loaded onto the JPK Nanowizard III AFM head and the laser was aligned on the back side. The head was moved towards the surface of the microscope slide using coarse steps until a streak of the UV curing glue was in roughly the same focus as the cantilever of the probe (as viewed through the viewing screen of the optical microscope used with the AFM). Using the AFM as a micromanipulator, the AFM tip was moved over the glue streak (using the optical microscope) and then lowered in small increments (5 μm or less) until the measured deflection value changed, indicating to contact with the glass bead. If contact with the glue was made, then retracting the probe from the surface would not occur until a few retraction steps were taken because the glue caused the probe to deflect adhesively.

Once the glue was applied to the cantilever/AFM tip, the tip was moved to a glass bead, chosen based on visual inspection of cleanliness and separation from other beads. The cantilever was lowered using small steps until the deflection deviated from zero and in some instances one additional approach step was taken to ensure good contact. A blue handheld laser with a wavelength of 405±10 nm and a max output lower than 5 mW was then directed towards the AFM probe covered in UV curing glue which was now in contact with the chosen glass bead. The light for the optical microscope used on the AFM was turned off and the blue laser was turned on and positioned so that the reflection of the blue laser could be clearly seen on the viewing screen attached to the optical microscope indicating that the laser was in the right spot to cure the glue. The laser was held here for 1 min and then the optical microscope light was turned back on and the AFM probe retracted 50 μm. If the glass bead went out of focus with the AFM probe then it was successfully attached, otherwise glue was reapplied to the AFM probe and a new bead was found. In most instances, between 1 and 3 attempts were necessary; this lack of consistency likely resulted from the limited contact area of the cantilever tip, which may inhibit effective sticking of the bead. Use of tip-less cantilevers would likely alleviate this issue.

2.2.4-Surface Preparation

2.2.4.1-HOPG

Force maps were obtained on highly oriented pyrolytic graphite (HOPG), UV ozone treated silica, and silica reacted with dichlorodimethyl silane (DCDMS). HOPG surfaces were obtained by cleaving the upper layer of a ZYH-grade planchet from Momentive Performance (Strongsville, OH) using double-sided tape. No further cleaning treatment was performed to this surface.

2.2.4.2-Silica

The silica used was cleaved into 1cm x 1 cm surfaces from a 4-inch diameter ellipsometry standard (J.A. Woolam) with a 60 nm thermally grown oxide layer using a diamond tipped scribe. The cleaved surfaces were then cleaned using a methanol soak with sonication to remove any particles present on the surface from the cleaving procedure. DI water was used to rinse the samples, which were then dried in a nitrogen stream. Next, the silica surfaces were placed in a Harrick Plasma Cleaner (PDC-32G) and cleaned using the 'medium' setting (10.5 W applied to RF coil) under vacuum for 10 minutes. The surfaces were then transferred to an 80ºC RCA-1 cleaning solution (1:1:5 solution of NH_4OH:H_2O_2: Milli-Q H_2O) for 25 minutes in a Teflon® sample holder. Next, the surfaces, removed from the solution, were rinsed individually with Milli-Q H_2O and dried under a nitrogen stream. Then they were immediately moved to the plasma cleaner for 5 minutes on the 'low' setting (6.8 W applied to RF coil) and finally removed to fluoroware for storage until use. Before a silica surface was used from storage it was exposed to UV ozone for 45 minutes and then placed at the bottom of the dish before adding surfactant solution.

2.2.4.3-Silanated Silica

To obtain a silanated silica surface, a silica surface cleaned in the manner described above was exposed to dichlorodimethyl silane vapor post UV ozone treatment by holding the silica surface inverted in the mouth of the silane bottle for 30 seconds. No further cleaning treatment was performed on the silanated surface.

The contact angles of water on the three surfaces post treatment were measured using the sessile drop method and are given in Table 2. The results agree well with literature values using the same surfaces.[64,94] The results showed that the silanated silica had the most hydrophobic character of the three surfaces used followed by HOPG. The UV ozone cleaned silica sample was completely wetted by water and was therefore the most hydrophilic.

Silanated Silica	96.1
HOPG	62.0
UV Ozone Silica	~0 (completely wetted)

Table 2. Contact angle of 18 MΩ water on silanated silica, HOPG and UV Ozone cleaned silica.

2.2.5-Surfactant Soft Contact Imaging

Soft contact imaging on HOPG and silica was performed using a JPK Nanowizard III (Berlin, Germany) AFM and PPP-BSI probes. To image surfactant assemblies on these surfaces the probe was approached and then image collection begun. The setpoint was decreased during scanning until the tip came fully away from the surface, overcoming adhesion forces, and then the setpoint was increased until surfactant was observed. An easy verification that surfactant is being imaged and is not an artifact is by changing the scan angle and size. If changing these parameters produces no apparent variation in the image, then the image features are most likely either artifacts or caused by feedback due to inaccurate tuning parameters.

2.2.6-Concentration and Probe Switching Methods

2.2.6.1-Batch Method

The simple setup of the batch method (a dish and surfactant solution) and the potential for combining data from several trials makes the batch method an attractive

means of collecting force curve data with surfactants. The surface was placed (double-sided tape was only used in the case of HOPG) at the bottom of a clean glass dish large enough to accommodate the AFM head and then approximately 12mL of surfactant solution at the proper concentration was added. The probe then approached the surface and force maps were collected. Then the probe was retracted and the solution and submersed surface were removed before a separate dish with a separate surface in a separate aliquot of the surfactant solution was put in its place. The probe was also removed from the AFM head, UV Ozone cleaned and then put back in the AFM head (or a different probe also UV Ozone cleaned was placed in the AFM head) before approaching.

2.2.6.2-Perfusion Method

The perfusion method, although having a more complicated setup than the batch method, ensures the collection of data from the same location between trials and removes the effects of tip cleaning and concentration switching. The perfusion method was carried out using the same glass dishes as used in the batch method, but syringes connected to Teflon® tubing were used to inject the solutions into the cell on one side of the dish and withdraw it from the other, removing the need to move the AFM tip laterally allowing for force maps and imaging to be performed in the same exact spot at different surfactant concentrations. First, water was injected into the cell and force maps were collected before retracting the AFM probe by 5 μm. Then the syringes placed in the dish were used to remove the solution in the dish at the same rate that the new solution, in this case 0.2×CMC TTAB, was injected. When twice the volume of the dish had been perfused, the system was left unperturbed for 10 minutes to allow for equilibration and then the AFM tip was approached, and mapping or imaging was

performed. Each map took approximately 20 minutes to collect and in some cases a map was collected immediately following another map. Comparing subsequently collected maps allowed for following the time evolution of adsorption or location of specific patches of surfactant. This procedure was repeated for the whole concentration series, which began with water and was increased by 0.2×CMC until 0.8×CMC and then the concentration was further increased to 2×CMC and then 5×CMC and finally 10×CMC.

2.2.7-Force Mapping on Various Surfaces

The force mapping feature of the Nanowizard software was used to obtain a 32×32 grid of force curves in desired areas with varying map sizes on HOPG, silica, and silanated silica using both the PPP-BSI probes and the "f" cantilever on a MSCT probe. However, the aspect ratio of the PPP-BSI tips varied between normal stock aspect ratio, upper image in Figure 4, for the flat HOPG, silica, and silanated silica force mapping and a much higher aspect ratio tip , shown in the lower image in Figure 4, used for characterizing and force mapping the trench and pillar structures. Before use, each probe was calibrated to determine the deflection sensitivity and the force constant by obtaining a force curve on

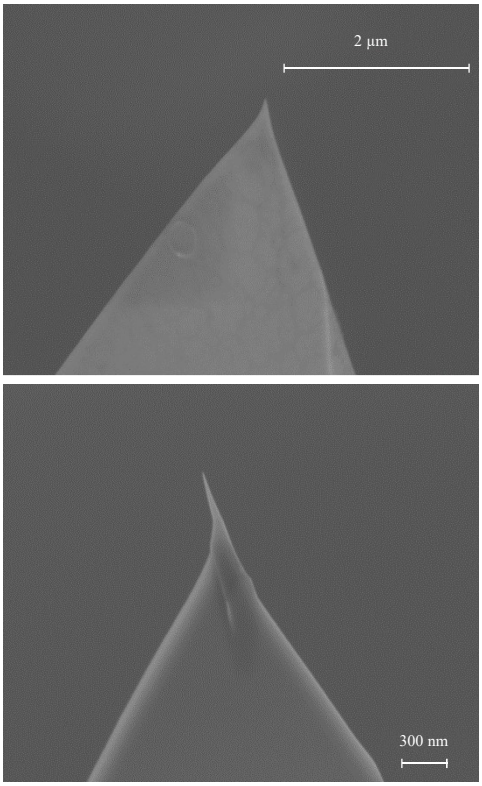

Figure 4. (Upper) Normal aspect-ratio probe, (Lower) High aspect-ratio probe

a clean microscope slide and fitting the gradient (slope) of the line where the probe was in contact and then by using the thermal method, respectively.

The probes were used only if the measured force constant fell within the specification parameters (~ 5 percent of the probes did not meet this criterion). The deflection sensitivity was measured again in solution on the substrate prior to any other measurements. Note that the cantilever shape for the PPP-BSI probe is rectangular while the MSCT cantilever is triangular; although this could cause a difference in the lateral bending of the cantilever, we are only using the vertical deflection for analysis and therefore the difference in shape should not be an issue if the force constants are known.

The curves in Figure 5 show the difference between a force curve obtained in water (Figure 5a) and one obtained in an aqueous medium containing surfactants (Figure 5b). The former shows only a snap to contact at ~5 nm caused by attractive surface forces while the latter shows a repulsive force beginning at approximately 15 nm (generated by the electrical double layer near the surfactant assembly) and ending with an instability at ~4 nm. Following the instability, the probe is in contact with the substrate underneath the surfactant layer. The force at which the instability occurs is taken to be the break-through force while the distance between the instability point and the substrate is taken to be the break-through distance. Each force curve within a force map was obtained with a tip velocity of 700 nm/s and over a range of 500 nm. The relative force setpoint (the force at which extension of the probe was stopped and retraction begun) was varied based on the force required to obtain a sufficient number of points post break-through, usually between 3 nN and 8 nN.

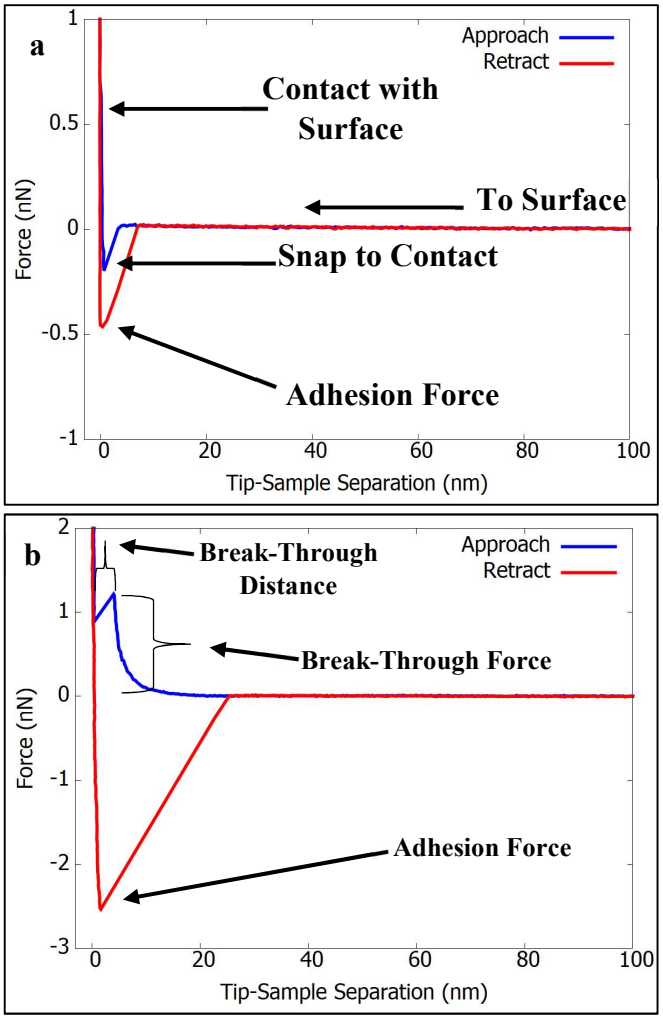

Figure 5. Actual data used to identify key parts of AFM force curves.
Top: water. Bottom: surfactant solution.

Once the probe reached this setpoint, it was retracted from the surface. Due to adhesive forces between the surface and the probe there was a distance during which the probe remained on the surface past the point of zero deflection. A snap-off the surface occurred once the force necessary to overcome adhesion was applied and resulted in a minimum in the force curve, which was taken as the adhesion force. In a force curve, a negative force is attractive, however, we will discuss both the break-through force and adhesion force as positive values given the conventions typically used for both forces.

2.2.8-Automated Analysis Post Collection (Python and Gaussian Fitting)

Post collection, the JPK data processing software was used to convert the gathered deflection and distance data into force and tip–sample separation before exporting each curve as a separate text file. The force curves were then analyzed using scripts developed in Python, which first separated the data into approach (extend) and retract curves and then identified the break-through points to obtain break-through distance, break-through force, and adhesion force. The data obtained from each force map was used to create histograms, which summarize the break-through distance, break-through force and adhesion force acquired from the force maps. Our analysis operates under the assumptions outlined by Butt and Franz, specifically that there is a probability distribution which describes the point at which the tip will break through the surfactant layer, and therefore a range of values are possible for any trial.[78] The

$$y = A \cdot \exp\left(-\frac{(x-\mu)^2}{2 \cdot \sigma^2}\right)$$ **Equation 2. Normal Distribution**

histograms were then fit to a normal distribution using Equation 2, where A is the normal distribution peak maximum and μ and σ are the mean and standard deviation respectively.

The fitted values were then compared using a variety of concentrations, surfactants and surfaces. In the event of multiple peaks, Equation 3, which uses the same variable designations

as Equation 2, was used to fit the histogram data,

$$y = A_1 \cdot \exp\left(-\frac{(x-\mu_1)^2}{2 \cdot {\sigma_1}^2}\right) + A_2 \cdot \exp\left(-\frac{(x-\mu_2)^2}{2 \cdot {\sigma_2}^2}\right)$$ **Equation 3. Two Peak Normal Distribution**

2.3-Fabrication of Laterally Confining Structures

2.3.1-Trench Fabrication

2.3.1.1-Polymers Used in Trench Fabrication

Polymers and development solvents used in the electron beam lithography process were obtained from Microchem Corp. The positive resist polymers were poly(methyl methacrylate) (PMMA) dissolved in anisole and two copolymers of PMMA/Methacrylic Acid (MAA) dissolved in ethyl lactate. All polymer and co-polymer solutions were received as 9wt.% dilutions and further diluted to various concentrations using the pure forms of their respective solvents. Silica was cleaned as described in the main text prior to spin coating.

2.3.1.2-Polymer Spin Coating and Curing

Cleaned silica pieces were placed on a Laurell Technologies WS-400-NPP spin coater using the instrument suction stage and 3-4 drops of one of the prepared polymer or co-polymer solutions was applied to the silica surface via pipette. The sample was spun at 4000 rpm for 40 seconds and then removed from the coater. This process was repeated for each silica sample in a set and the set was then cured in a vacuum oven for

2 hours at 160°C. Post cure the set was removed and allowed to cool to room temperature and then stored in individual fluoroware containers.

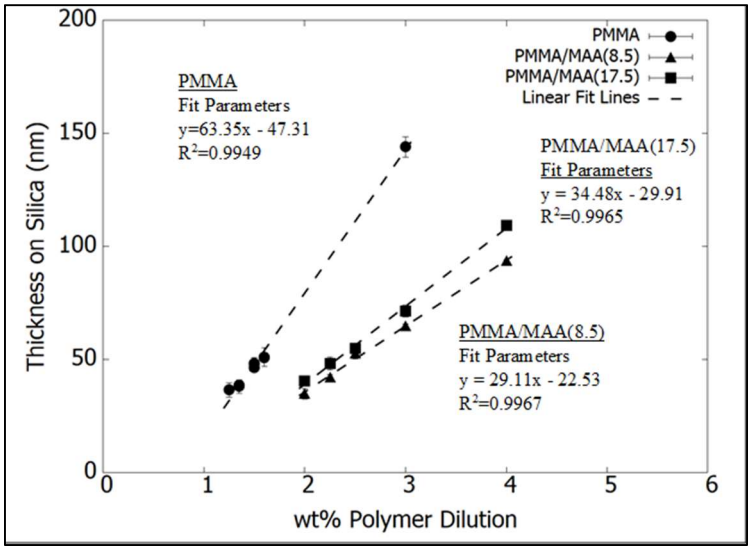

Figure 6. Thickness of polymer layer on silica vs. polymer dilution concentration for PMMA, PMMA/MAA(8.5), and PMMA/MAA(17.5).

Various thicknesses of the polymer on the silica were obtained by varying the wt.% of the polymer in the dilution. Calibration curves for polymer layer thickness vs. polymer concentration are shown in Figure 6. The resulting polymer thicknesses, which were measured by removing an area of the polymer on the silica with a razor blade and imaging with AFM, displayed linear trends at this spin speed and spin time. In this work the desired thicknesses were between 40-50 nm on the silica, which were respectively obtained using 1.35wt.% and 1.6wt.% with PMMA, 2.15wt.% and 2.5wt.% with PMMA/MAA(8.5), and 2wt% and 2.32wt% with PMMA/MAA(17.5).

2.3.1.3-Electron Beam Lithography and Metal Lift-off

Electron beam (e-beam) lithography was performed in an FEI Helios DualBeam scanning electron microscope equipped with the NanoPattern Generation System (NPGS). The scope was optimized and operated at 4 mm WD, 30 kV and 21-23 pA, verified by Faraday cup prior to each exposure session. Accurate measurement of the working electron beam current was necessary when using the NPGS to get reproducible exposure line widths between samples and exposure sessions. To prepare a sample for

e-beam lithography, first the polymer surface was scratched with a razor blade to make registration lines, which were used later to find the exposures with SEM or AFM post development. The sample was then exposed to the electron beam, which moved the beam over the surface to create patterns with different electron beam doses. The areas exposed to the beam were then soluble in the developer solvent (1:3 methyl isobutylketone:isopropyl alcohol solution) which the sample was immersed in at -5°C for 30 seconds. Once time had elapsed the samples were moved directly from developer to chilled IPA for 20 seconds and then room temperature water for 15 seconds. The samples were then dried in an N_2 stream and stored.

The resulting trench widths and depths were characterized by metal lift-off and AFM, respectively. Metal liftoff was performed by sputter coating a sacrificial sample with PtId to a thickness of 20 nm and then removing the polymer by soaking in a series of three 20 ml baths made up of the following. The first two contained NanoRemover PG at 50°C (10 minutes each) and the third was isopropyl alcohol at room temperature (10 minutes). Lastly, the sample was rinsed in a DI water stream and then dried under a nitrogen stream. The width of the deposited metal left behind was measured using SEM and showed the width of the floor of the trench where it meets the trench wall. This

technique should account for any widening of the trench at the bottom that may have occurred during trench formation because of the isotropic nature of metal sputtering (as opposed to the anisotropy of metal evaporation).

Tests were performed to determine which electron beam doses would yield the desired trench widths with the two polymer layer thicknesses. The resulting calibration curves are given in Figure 7 and show a linear trend of line width with increasing electron beam dose for all polymers used. It was also observed that the slope of the trend was lower for the 50 nm polymer layer than the 40 nm layer for each polymer used.

AFM investigation of trench characteristics using high

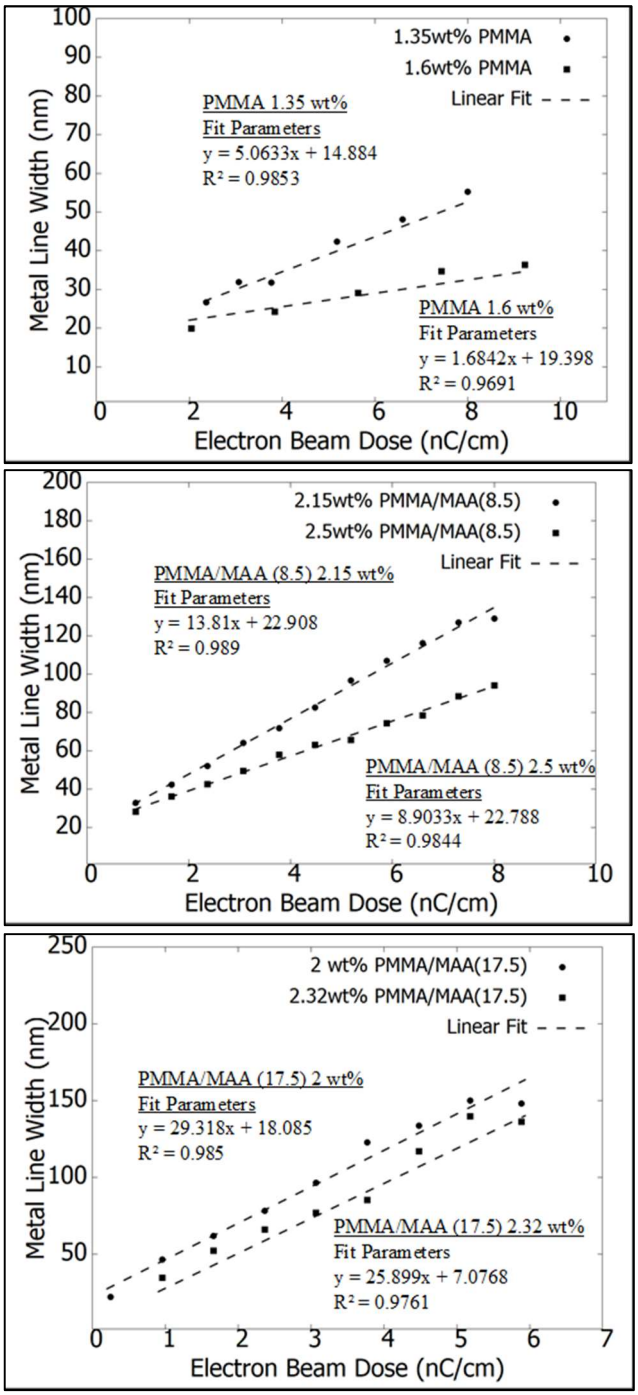

Figure 7. Metal line width on silica surface post polymer removal vs. electron beam dose used to make the line in the polymer. The various polymers, their dilution concentrations and the linear regression values for each data set are also provided.

aspect ratio probes was performed in both intermittent contact (tapping) and constant contact mode. To make sure that the trench characteristics were unaltered by AFM imaging, a series of images and line profiles were taken of a trench in tapping mode, then contact mode and then again in tapping mode. The tapping mode images before and after showed the same trench width even through contact mode showed larger widths, indicating any polymer stretching during scanning was elastic and temporary.

2.3.2-Trench Characterization

E-beam lithography was used to form trenches in ~50 nm thick spin-coated polymers. Polymers used were poly(methyl methacrylate) (PMMA) homopolymer and two copolymers with methacrylic acid (MAA), an 8.5 wt.% acid number (PMMA/MAA(8.5%)) and a 17.5 acid number (PMMA/MAA(17.5%)). The acid number is the weight fraction of acid comonomer units in the polymer. The sessile drop method was used to obtain contact angles of DI water on the spin-coated polymer surfaces and the results are given in Figure 8. PMMA had the most hydrophobic surface at 71.9°±1.2°, followed by PMMA/MAA(8.5) at 67.4°±1.0° and finally PMMA/MAA(17.5) with a contact angle of 64.3°±1.3°. These results show that an increase in the MAA content caused an increase

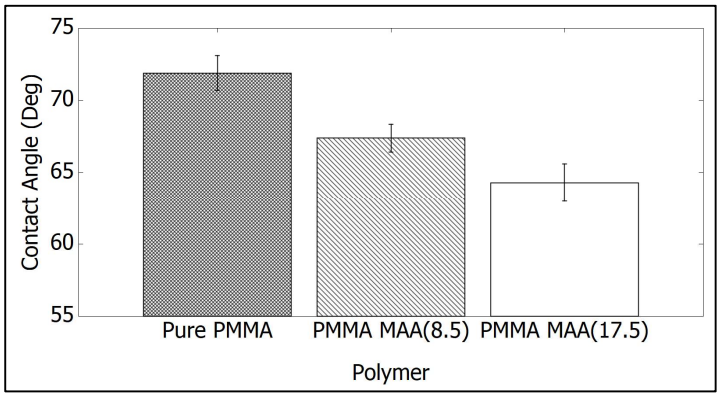

Figure 8. Contact angles of DI water on PMMA, PMMA/MAA(8.5), and PMMA/MAA(17.5), measured using the sessile drop method.

in the hydrophilicity of the polymer layer as expected; which in turn varies the hydrophilicity of the walls for the trenches.

2.3.2.1-AFM Intermittent Contact Mode Imaging

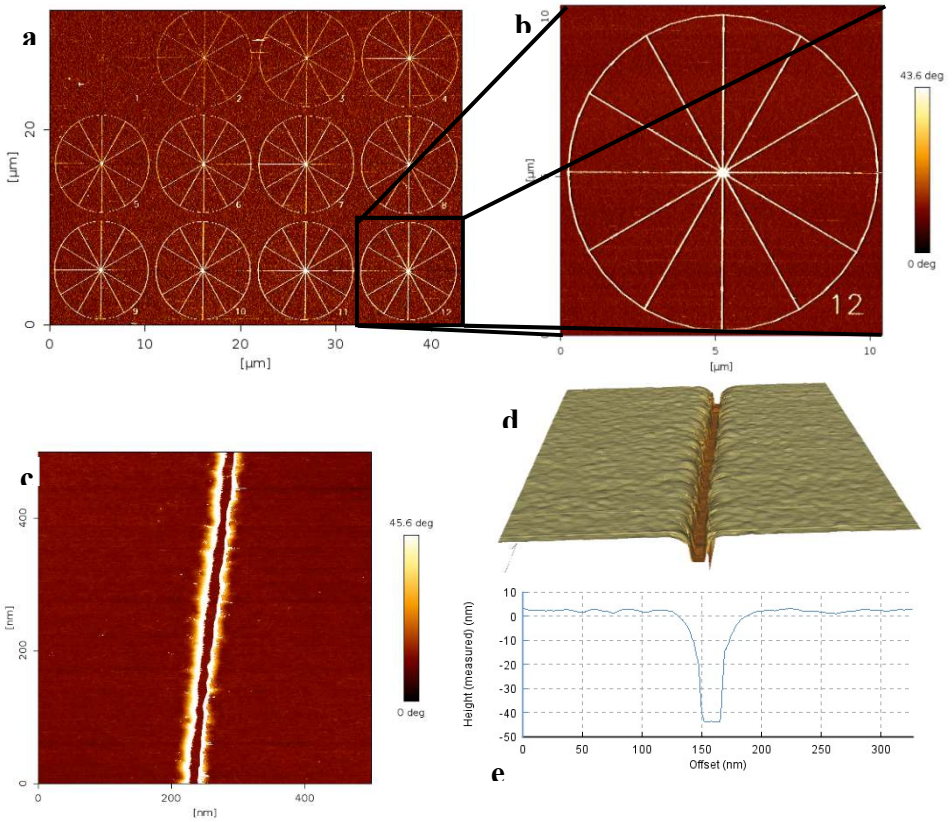

Figure 9. Results of electron beam lithography on PMMA. Images are AFM phase images collected in air, a 3D model of the 500 nm scan and a line profile from the height image of the same scan.

The results of AFM imaging a wheel array produced via e-beam lithography, wheel 12 of that array, and a spoke of that wheel are shown in Figure 9. The imaging was performed in tapping mode using our high aspect ratio PPP-BSI tips. The array (Figure 9a) was found by positioning the AFM cantilever with the registration scratches made in the polymer prior to e-beam exposure. The array itself was not visible with an optical microscope but was found with a large area AFM scan and then imaged further. The array has varying dosage for each wheel, with wheel 1 having the lowest dose

(lines with lowest width) and wheel 12 (Figure 9b) having the highest (lines with highest width). In fact, wheel 1 was given a dose that was too low to fully remove the polymer down to the substrate and is therefore difficult to see in the array. An example image of a spoke from wheel 8 is given in Figure 9c, and a 3D model and line profile are given in Figure 9d and Figure 9e, respectively. Other wheels with smaller line doses were investigated but only the floors of wheel 8 and higher, which had metal-lift off widths of 50 nm, was able to be reached even when using the high aspect ratio AFM probe.

2.3.2.2-AFM Force Mapping of a Single Trench

The trench was then investigated using contact mode force mapping and the results are shown in Figure 10 in the form of an adhesion map collected using the high aspect ratio PPP-BSI tip. It is possible to distinguish the upper surface of the polymer, the edges, and the lower surface of the trench. Due to the finite size of the tip, the exact nature of the polymer wall-silica floor intersection could not be precisely determined. Unfortunately, PMMA and silica without surfactant adsorption display similar snap-to-contact and adhesion values so this could not be used to distinguish the identity of the bottom of the trench. However, the widths of the upper mouth of the trench (~50 nm from the line profile in Figure 9e), which should not be affected by tip convolution, were statistically the same as the widths determined by metal lift-off experiments for each trench. This suggests a mostly vertical trench wall and square wall-floor intersection.

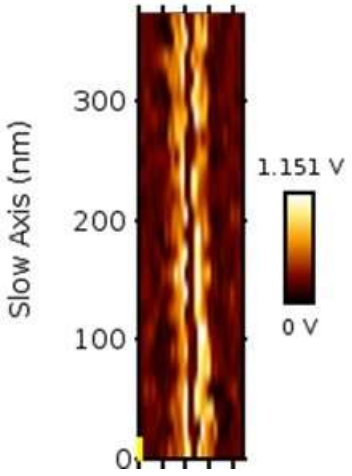

Figure 10. Slope map collected on a trench in air.

The lower surface of the trench spans 2-3 map indices in the x-dimension which over the length of the map provides 50-60 points to analyze. Given the width of the trench and the resolution of the tip, the 2-3 map indices indicate that only the center of the trench is being imaged and this statement is true for all trench measurements. Hence, we considered all points imaged in a trench to be equivalent and clearly points at or very near the center of the trench are being sampled.

2.3.3-Pillar Fabrication

Pillars were fabricated by reactive ion etching (RIE) of a surface coated with metal that had been selectively evaporated through the interstitial sites of 200 nm polystyrene microspheres. RIE left pillars in the areas where the metal was on the surface and the original silica surface was obtained by etching the metal with CR 9051 chrome etchant (obtained from Transene Co.). For further details regarding the preparation of the pillar surfaces, please see the Appendix.

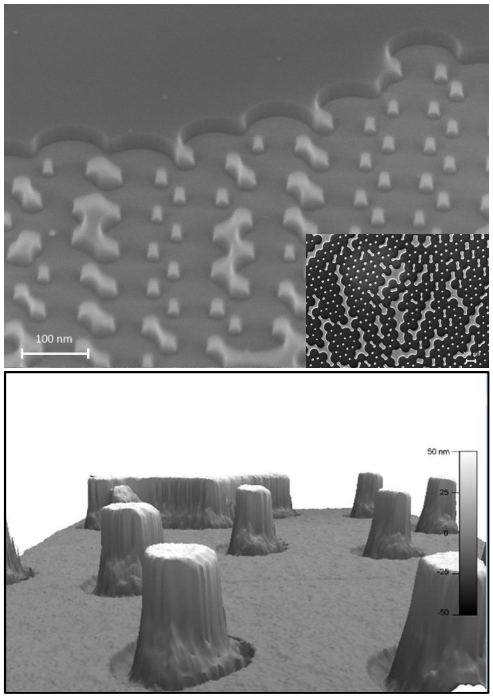

Figure 11. Results of 30 second etching trial performed with 200 nm diameter polystyrene nanospheres. Upper image is SEM and lower image is AFM.

2.3.4-Pillar Characterization

The results of a 30 second etch trial are shown in the SEM image in Figure 11 (upper), collected in a Zeiss Neon SEM using an accelerating voltage of 10kV. The etch rate was found to be 1.5 nm/sec, resulting in pillar heights of approximately 45 nm. The images in Figure 11 also shows a distribution of nano-structure types, including dumbbell shapes, stretched zig-zag patterns and peninsula like formations extending from larger islands. The wide variety of shapes were caused by the nanosphere mask having defects due to agglomeration during layering. SEM images were difficult to collect because the features were mostly edges and therefore highly sensitive to electrons scattered within the silica surface leaving from the structures resulting in a decrease in edge contrast. There were also issues with "double vision" at the edges, which is believed to be caused by the electron beam interaction volume traveling deeper than the structures were wide, causing the edges to look somewhat transparent further from the etch floor. However, vertical side walls are apparent, indicating a mostly anisotropic etch.

Further characterization of the pillars was performed using AFM, the results of which are given in the lower image in Figure 11. This 3D rendering of the surface demonstrates the high-resolution capabilities of the higher aspect ratio AFM tips. An imaging artifact, striated walls, appears on the right side of the nanostructures. However, all the structures show this same feature on only the right side indicating that the feature is not real. The AFM imaging supports the conclusions drawn from SEM micrographs regarding the vertical nature of the substrate sidewalls as well as showing a flat upper pillar surface. The diameter of the top of pillar structures had diameters

between 35 nm and 15 nm, respectively, measured using SEM and confirmed with AFM. The RMS roughness of the upper surface (previously masked by metal) was measured and found to be 0.181±0.017 nm while an unprocessed silica surface was found to be 0.170 ± 0.00866 nm, indicating the surface was well protected during etching. For a more in-depth explanation of the processes used, as well as results of the fabrication performed using 100 nm polystyrene nanospheres and longer etching times, please see the Appendix.

Chapter 3: Results and Discussion

3.1-QCM Investigation of Random Lateral Confinement and Temperature

3.1.1-Equilibrium Adsorption on Smooth Surfaces

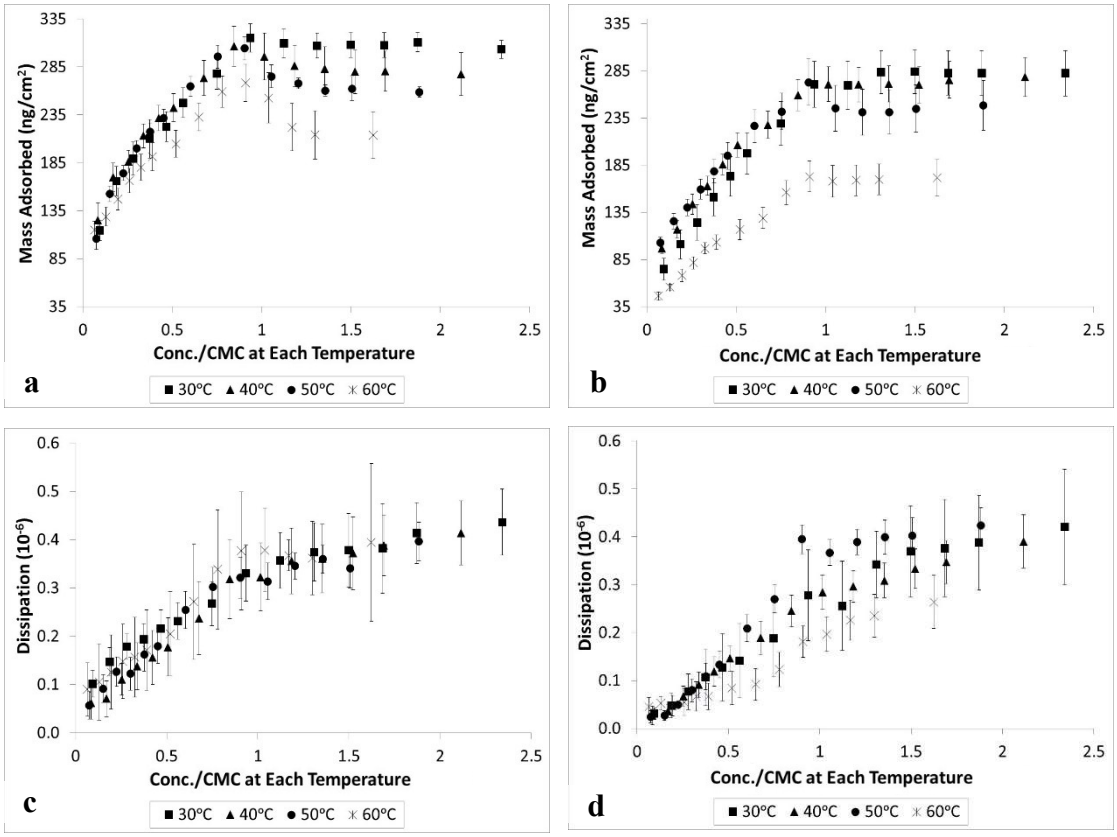

Figure 12. Top Row - CTAB adsorption per unit of nominal surface area vs. bulk concentration normalized by the CMC at, 30, 40, 50, and 60°C on smooth (a) and rough (b) gold surfaces. Bottom Row - Dissipation vs. bulk concentration normalized to CMC at each temperature and roughness.

The amount of CTAB adsorbed per unit of nominal surface area vs. bulk concentration normalized to the CMC of each temperature on the smooth surface is shown in Figure 12a. Below the CMC, as the bulk concentration increased the amount of surfactant adsorbed per area increased for all temperatures, with no statistical difference between the results obtained at different temperatures. Once the CMC was reached all results shown in Figure 12a at temperatures 30°C and above show a slight maximum in adsorption, followed by a decrease to a plateau as the concentration was

increased further. The highest amount adsorbed at the plateau was obtained at 30°C ($3.1x10^2$ ng/cm^2). As the temperature increased, adsorption decreased, with the minimum obtained at 60°C (~ $2.1x10^2$ ng/cm^2).

The maximum in adsorption at the CMC is associated with the formation of bulk micelles at the CMC. Maxima in adsorbed mass have also been noted by others, although explanations for the phenomena are varied.[1,24,26,35,36,95-97] In our case, we believe that surface-active impurities were adsorbing within the supported film below the CMC. Once the CMC is reached, these impurities and some surfactant desorb from the film and partition to the newly formed micelles, yielding a decrease in the mass adsorbed. Impurities could be isomeric variations of the primary surfactant, which have been suggested to yield the maximum seen for mass adsorbed below the CMC.[97] A study by Furst et al. also supports the possibility that the maxima were caused by non-surfactant associated impurities.[24] These authors found that maxima in amount adsorbed occurred most often when their silicon surface was exposed to concentrations below the CMC before being increased above the CMC, leaving trace amounts adsorbed following a rinsing step. For surfaces exposed to concentrations above the CMC only, nothing was left on the surface after rinsing, which suggested that any impurities were completely solubilized by micelles in solution. The impurity in question was later determined as being caused by the poly(vinyl chloride) tubing used in the experimental set-up.[26]

Our group reported maxima in adsorbed amount near the surfactant CMC previously.[57] Maxima reported in our previous work were much more substantial than those shown here, although the same surfactant and similar surfaces were used.[10] However, previously sonication and helium sparging of the surfactant solutions were

not used. We conclude that the sonication/sparging removed impurities from the solutions. Even though we recrystallized three times, a comparison of the amount of surfactant adsorbed to the amount present in solution for adsorption experiments on our relatively flat surfaces suggests that the ratio of impurities to surfactant must be on the order of 1 $x10^{-5}$ or less to fully exclude the possibility of impurity adsorption; obtaining this level of purity based on recrystallization alone is very difficult.

Dissipation data as obtained on the smooth surface are shown in Figure 12c. The dissipation, and consequently the morphology, of the adsorbed aggregates were not strongly affected by temperature within the tested temperature range. The greatest dissipation measured was roughly 0.44 $x10^{-6}$ at 30°C at 2.0×CMC, which is below the criteria reported in the literature for a rigidly bound film (<1.0 $x10^{-6}$).[59] This low value for the dissipation supports the use of the Sauerbrey equation to determine mass adsorbed from frequency data. As the concentration increased, the dissipation increased for all isotherms. A slight decrease in slope for the dissipation vs. concentration curve was observed once the bulk concentration reached the CMC, but unlike mass adsorbed there was no maximum, suggesting that desorbing impurities had a negligible influence on the flexibility of the supported films. The very slight dissipation increase above the CMC with increasing surfactant concentration is attributed to an increase in the viscosity of the bulk fluid.

3.1.2-Equilibrium Adsorption on Rough Surfaces

The adsorption isotherms obtained on rough surfaces followed the same trend observed on the smooth surfaces. As the bulk concentration increased mass adsorbed per unit area on the rough surface increased, as shown in Figure 12b. In this Figure the

nominal surface area is used for estimating the amount adsorbed from the QCM data instead of the actual surface area; the latter requires an assumption such as a fractal surface. [10] When comparing the isotherms above the CMC in Figure 12a and Figure 12b, on average the equilibrium values were lower on the rough surface than the smooth surface, a result our group reported previously.[10,57] This decrease in adsorption is caused by disruption of surface aggregates and intermolecular tail-tail interactions by surface roughness.[17] Since nominal surface areas were used in the calculation of the surface area, the actual decreases in adsorption densities were larger than shown in the graphs.

On the rough surface, below the CMC mass adsorbed at 30°C was less than for 40°C and 50°C. However, mass adsorbed at 30°C becomes greater than at 40°C and 50°C near the CMC. The only peak in mass adsorbed occurs in the 50°C isotherm, while the other isotherms display rather monotonic transitions to their plateau values. The largest amount of mass adsorbed in the plateau region on the rough surface is $2.8x10^2$ ng/cm^2 and occurs at 30°C at 1.4×CMC, while the smallest value is $1.6x10^2$ ng/cm^2, found at 60°C for 1.6×CMC. As with the smooth surface, an increase in temperature led to a decrease in mass adsorbed above the CMC. Data collected on the rough surface shows a greater separation between the 50°C and 60°C isotherms, which may be an effect of extra washing cycles increasing the surface roughness, as three extra washing cycles were necessary to repeat the 60°C trial following the failure of the first trial from bubble formation in the tubing.

Dissipation data collected using the rough surface can be found in Figure 12d. The data are again consistent with a rigidly bound surfactant film on the surface of the

crystal. The data did not show any statistical difference between temperatures, except for 50°C, which showed greater dissipation near the CMC. No observable maximum in dissipation was found. Above the CMC, there was a slight increase in the dissipation with concentration, attributable to a slight increase in bulk viscosity. Although we expected that the dissipation would show some evidence of a change induced by an increase in the surface roughness, no statistical distinction between dissipation values gathered on the two surfaces was observed. This suggests that the films formed on rough substrates were of similar morphology to those formed on the smooth substrates, although they were present in lower amount, as suggested by the lower amount adsorbed. This result also implies that some portions of the rough surface are not covered by surfactants.

3.1.3-Time Dependence of Adsorption

3.1.3.1-Adsorption at 0.1xCMC

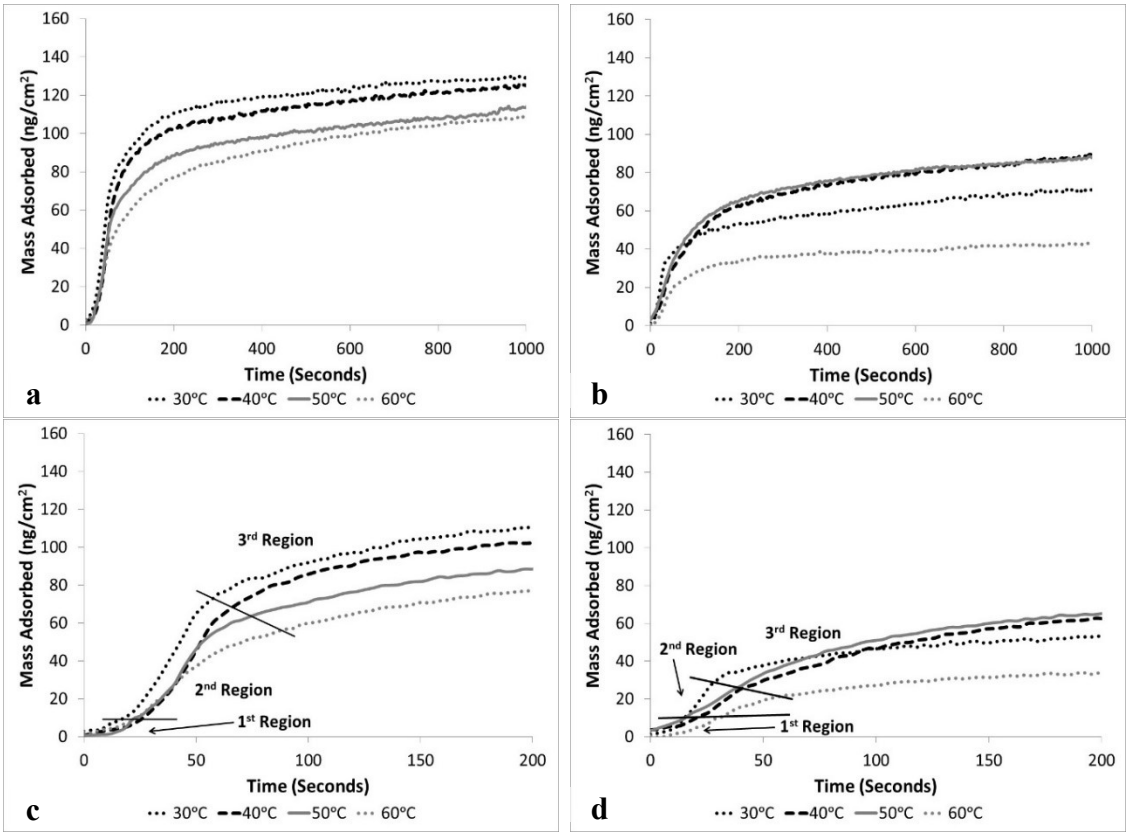

Figure 13. Mass CTAB adsorbed per unit of nominal surface area as a function of time on both smooth (a, c) and rough (b, d) surfaces at 0.1xCMC.

Figure 13 shows the adsorption per nominal surface area from a 0.1×CMC solution at different temperatures on both smooth and rough surfaces as a function of time. Mass adsorbed increased quickly until a plateau was reached for both the smooth and rough surfaces. The plateau in adsorption on the smooth surface decreased with increasing temperature. Surprisingly, on the rough surface the effect of temperature on adsorption was not consistent. The 60°C isotherm yields the lowest adsorption equilibrium value; the 40°C and 50°C curves nearly overlapped and showed greater adsorption than results collected at 30°C. Based on smooth crystal data the 40°C and 50°C equilibrium values should be lower than the 30°C value. A likely cause is that

slight variations in the activity of available surface sites, caused by the cleaning procedure, became more apparent at low surfactant concentrations.

When the kinetics results are viewed on a large time scale, Figure 13a and Figure 13b, there appear to be only two regions of adsorption, a region of fast adsorption (~0-200 seconds) and a region of slow adsorption (time>200 sec), which were characterized previously through the use of kinetic models.[10,40] When the fast region is viewed on a smaller time scale (Figure 13c and Figure 13d) it becomes apparent that there were actually three regions. These regions have been quantified as 0-10 ng/cm^2 for the first region, 10-50 ng/cm^2 for the second region and above 50 ng/cm^2 for the third region. The first region represents the time interval where the concentration in the cell is changing with time; the residence time of the fluid in the cell is consistent with the time interval characteristic of this first region. At low concentrations, single molecule adsorption can be assumed in this first region. The second region also likely represents primarily single molecule adsorption. Some cooperative effects could be present, although at 0.1×CMC the number of adsorbed molecules where cooperative effects are significant is probably small. The third region is dominated by a plateau, indicating that the equilibrium adsorption is being reached.

To examine the differences between adsorption rates in the first two regions a one-step adsorption model, $q_i = q_{i-1} + m_i t_i$, was used.[40] In the equation, q_i, m_i and t_i are the mass adsorbed, slope of mass adsorbed over time and time elapsed values for the i^{th} region, while q_{i-1} is the final mass adsorbed value of the preceding region.

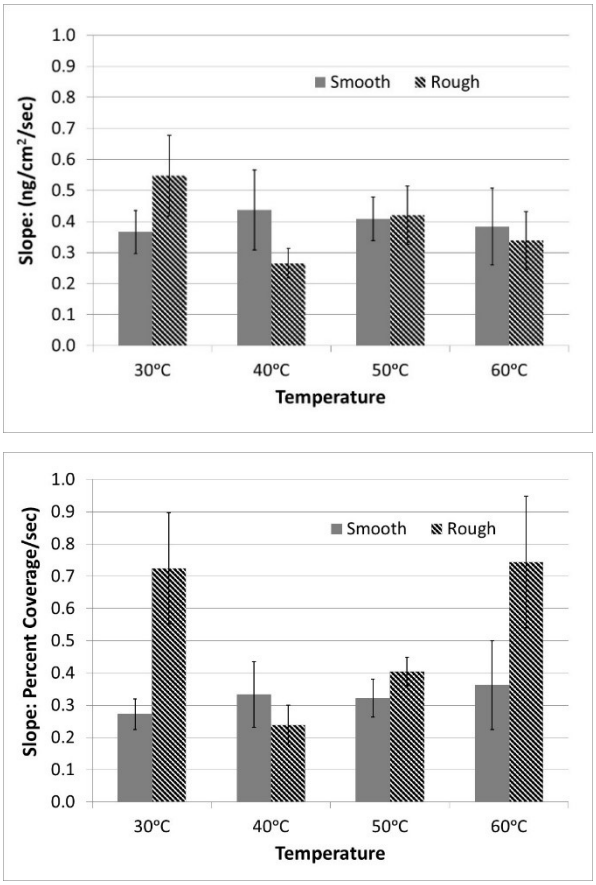

Figure 14. Average slopes of adsorption in areal mass per time and percent of equilibrium coverage in the first region for 30, 40, 50, and 60°C isotherms (left to right respectively) for a bulk concentration of 0.1×CMC on the smooth and rough gold surfaces.

Figure 14 reports the average slopes of adsorption for the first region for an increase from pure water to 0.1×CMC on smooth and rough surfaces. This region includes effects related to the flowrate used, but since the flowrate was constant for all trials any measured differences should only reflect differences due to temperature or surface differences. The averages presented are taken over 2 trials (4 crystals per trial) for the smooth crystals and 1 trial (2 crystals per trial) for the rough crystals. As shown in the top portion of Figure 14, no change in slope of mass adsorbed over time was found in this region by varying temperature between 30°C and 60°C or by changing the surface roughness.

A higher temperature should lead to faster adsorption in the low concentration region since the surface is not completely covered and the diffusion constant increases with temperature. Adsorption occurs through single molecule adsorption via electrostatic interactions between the polar head group and charges present on the surface, which are negative from the adsorption of bromide ions. [1,59,98,99] However, any

expected increase in the kinetics of adsorption is lower than the uncertainty in the measurements as represented by the error bars in Figure 14.

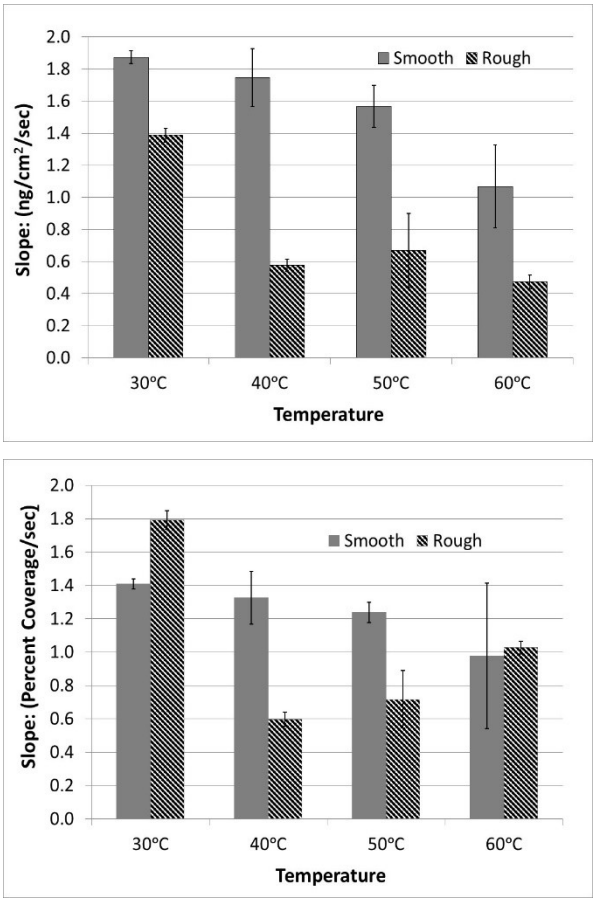

Figure 15. Average slopes of adsorption in the second region for 30, 40, 50, and 60°C (left to right respectively) for a bulk concentration of 0.1×CMC on smooth and rough gold surfaces.

Slopes of adsorption (amount vs. time) in the second region are shown in Figure 15. On the smooth surface the slope was greatest at 30°C and decreased with increasing temperature. For the rough surface, the slope at 30°C was the largest and there was statistically no difference between 40, 50, or 60°C. On an absolute mass adsorbed basis, the slope on the smooth crystals was higher than that for the rough crystals; this trend was reversed in some cases when taken on a basis of percentage of equilibrium value. The decrease in slope with increased roughness follows the same trend as was found above the CMC. As adsorption in the second region for 0.1×CMC is primarily an enthalpically-driven (i.e. non-cooperative) process, these results indicate that the effects of roughness extend even to regions of adsorption not entropically controlled. A similar finding was expressed previously where adsorption was slowed on a rougher surface by surface rearrangement, even at concentrations well below the CMC.[10] The fact that the kinetics

of adsorption decreases with an increase in temperature suggests that the heat of adsorption becomes less exothermic at higher temperature,[66] which counteracts increases in rate due to a diffusion constant increase. However, in one study with cetylpyridinium chloride, increasing temperature has been shown to lead to more exothermic processes, even though the amounts adsorbed were decreasing.[32]

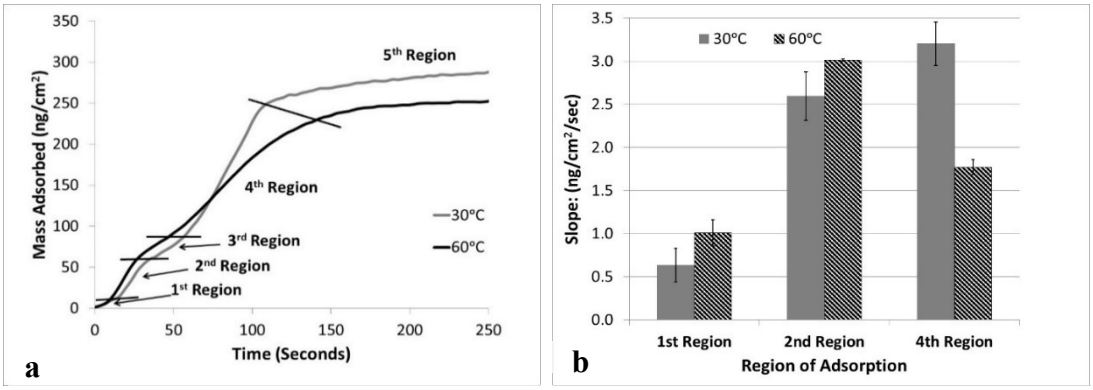

Figure 16. (a) Mass of CTAB adsorbed as a function of time on a smooth gold surface at 30°C and 60°C. (b) Average slopes of adsorption in the 1st, 2nd and 4th regions (left to right, respectively) at 30°C and 60°C for a bulk concentration of 1.8×CMC on a smooth gold surface.

3.1.3.2-Adsorption at 1.8xCMC and Two Different Temperatures

To better explore characteristics of other regions at higher concentrations, data for the step increase from pure water to 1.8×CMC were collected at 30°C and 60°C on a smooth surface and the associated slopes of adsorption for the different regions are shown in Figure 16. Five regions of adsorption are identified, with the first region beginning at time zero and ending where mass adsorbed is ~10 ng/cm^2. The second and third regions are designated as 10-50 ng/cm^2 and 50-75 ng/cm^2, respectively. The fourth region spans from 75 ng/cm^2 to where mass adsorbed begins to transition to a plateau. The fifth region is where the adsorption slowly approaches a plateau value. Here the monomer concentration is in such excess that region I is thought to have an effective concentration of 1.0×CMC almost immediately. The slope of adsorption in this first

region appeared to increase with an increase in temperature, whereas at low concentrations there was no observable trend with changing temperature. This behavior is possibly an effect of micelles in solution at high concentrations, even though Region I is still single molecule adsorption.[1,98,99] The slope of Region II was three times higher than that of Region I, where the 60°C slope is greater than the 30°C slope. These results support a diffusion controlled adsorption mechanism in Region II, where the increase in temperature caused an increase in the coefficient of diffusion.[100]

The third region observed at the higher concentration is a transition region between the different adsorption mechanisms characteristic of the second and fourth regions. The 30°C slope in the fourth region increased slightly compared to the second region but was much higher than the 60°C slope. The decrease in slope of adsorption with temperature indicates that the decrease in driving force for adsorption with an increase in temperature occurs in the same manner as the decrease in the entropic driving force observed for micelle formation in solution. Adsorption is entropically driven at high concentrations, where adsorption in the fourth region is driven by cooperative lateral interactions between surfactants adsorbed on the surface (analogous to region II of the four-region explanation for isotherms as a function of concentration).[1,66] The lateral interactions are a result of the entropic driving force which occurs as a result of the increase in the entropy gained by water molecules surrounding surfactant tail groups.[66,101] Upon adsorption and organization into a structure where the hydrocarbon chains associate with one another, these water molecules are released from their cage-like structure surrounding the surfactant, which increases the system entropy because the entropy loss due to the association between

the hydrocarbon tails is insignificant compared to the entropy gain of the water.[102] At higher temperatures the entropy gain is lower because the cage-like structure formed by water molecules around a surfactant tail is already less organized at higher temperature. Figure 16 shows that the overall decrease in adsorption of ionic surfactants with increasing temperature at high surfactant concentration occurs primarily because adsorption is less in the fourth region, where cooperative interactions dominate, due to a decrease in the entropic driving force for adsorption with an increase in temperature.

The gradual approach to a plateau seen in the fifth region (analogous to region III of the four-region explanation for isotherms as a function of concentration) is characteristic of rearrangement of adsorbed surfactant aggregates and filling of remaining surface sites.[1,99]

The regions described here show similarity to the four-region isotherm developed by Somasundaran and Fuerstenau, with the main difference being the currently presented analysis has a kinetic basis instead of concentration.[5,99] The most notable effect of this difference is the absence of a diffusion controlled region in the four region model which is self-evident since the four-region model is an equilibrium model. The Region II results for 0.1xCMC in this work do show agreement with the conclusions of Somasundaran et al. and their respective Region II regarding adsorbed single molecules nucleating increased adsorption.

3.2-AFM Force Curve Characterization of Adsorbed Surfactant on Flat Surfaces

3.2.1-AFM Force Mapping of an AFM Tip

Unless explicitly stated, throughout this paper the terms monolayer and bilayer refer to the number of layers forming the structures on the surface (e.g. monolayer refers to flat monolayers as well as hemi-cylinders and hemi-spheres, while bilayer refers to a flat bilayers as well as full cylinders and spheres). We have no reason to believe that our methods can distinguish the various types of single-layer type structures from one another, nor the various types of multilayer-type structures from one another.

Many previous publications interpret the break-through distance as the thickness of the adsorbed surfactant layer directly, which assumes there is no surfactant adsorbed to the probe. However, Ducker et al. investigated the surfactant adsorbed to the tip by collecting force curves, however without collecting a force map, on a silicon nitride surface using a silicon nitride probe with the zwitterionic surfactant dodecyl dimethyl ammoniopropanesulfonate.[103] They assumed that using the same material would yield similar structures on both the tip and the surface and determined that the thickness measured using force curves was based on the applied load. The latter conclusion is a result of designating thickness as any point between the point of initial increase in force and the instability point and not the break-through distance. In our work, this method of using a probe and surface of the same material is taken a step further by mapping an AFM tip using another AFM tip in 10×CMC TTAB solution, which provides not only the same material, but also the same surface geometry. Only single force curves could be obtained at the tip-tip interaction as compared to 1024 curves we could obtain for flat surfaces; therefore, similarly robust statistical data-sets were not possible. However, our data

demonstrate the concept of force mapping on an AFM tip, and they permit to draw conclusions based on the presence and appearance of break-through phenomena.

The mapping probe was positioned over the to-be-mapped probe using a top-down optical microscope. The to-be-mapped probe was prevented from deflecting away from the mapping probe by positioning it over the chip portion of a separate AFM probe (see Figure 17a), which, by design, was at the same height as the underside of the AFM cantilever. Prior to mapping the tip, a 32×32 force map was collected on the cantilever of the probe being mapped. This was obtained as a benchmark comparison to a flat surface of the same material at the same time and with the same probe being used to map the tip surface. The break-through distance, break-through force, and adhesion force were found to be 3.39 nm ± 0.61 nm, 0.33 nN ± 0.04 nN and 0.05 nN ± 0.007 nN on the cantilever, respectively.

Next, the tip itself was mapped using a 16×16 force mapping grid. The smaller grid size was used on the tip because a 32×32 grid experienced significant drift during the experiment. Even with the smaller map there was still a fair amount of drift, likely due to mechanical coupling within the complex arrangement of cantilevers and chips, but it was less of an issue because of the increased speed of collection with the smaller grid. Of the 10 maps collected, 3 were successful in collecting a force curve at the apex of the two tips.

The maps and a representative force curve are shown in Figure 17. The curves collected at the maximum height of the maps did display break-through forces above zero, indicating the presence of a repulsive force near the surface. The break-through distances, break-through forces, and adhesion forces for the three maps were found to be (3.3 nm, 0.28 nN, and 4.76 nN), (4.29 nm, 0.18 nN, and 2.23 nN), and (5.05 nm, 0.65 nN, and 0.33 nN), respectively.

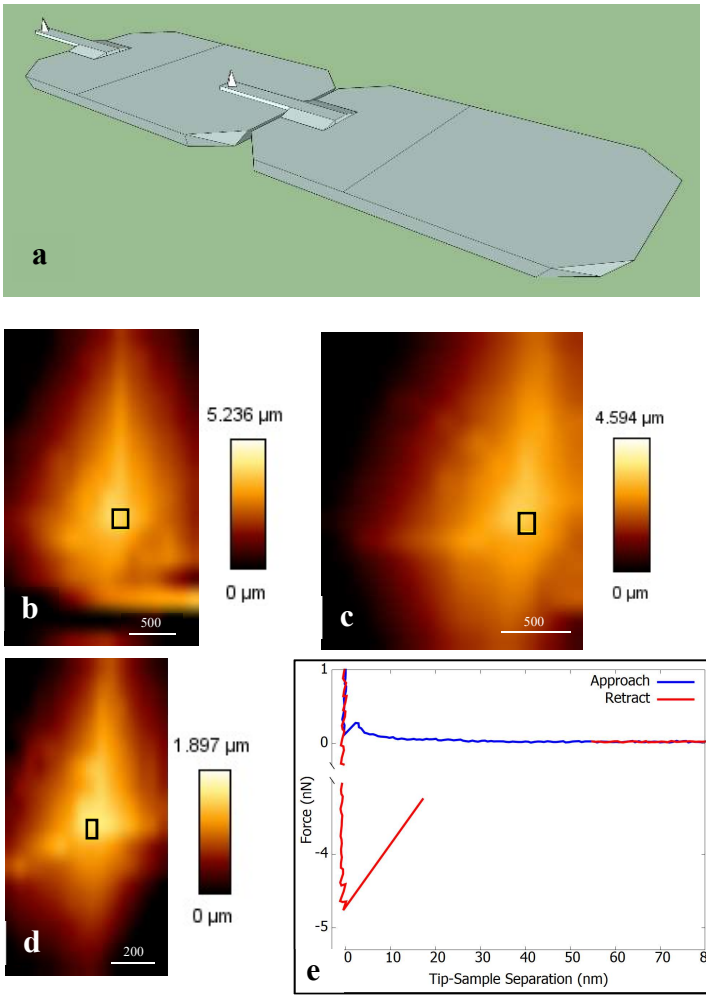

Figure 17. (a)-Scheme showing the AFM tip to be mapped positioned over the chip of another AFM probe to prevent deflection during mapping.

(b), (c), (d)-the three (separate) successful force maps of a PPP-BSI probe in a 10×CMC TTAB solution. the black boxes in the images are the point of maximum height measured value, taken to be the interaction between the two tips.

(e)-Example force curve (with a split y-axis) from between the two AFM tips at the maximum height.

Although there is substantial variation in these measurements, our results indicate that there is adsorbed surfactant with some thickness present. The symmetry of the system strongly supports the possibility of an adsorbed layer on both tips. This layer

is assumed to be a monolayer, since it has been previously stated that AFM tips should be incapable of supporting the formation of a bilayer without chemical modification.[104] To investigate surfactant adsorbed to a different type of probe, a colloidal probe was used on a flat HOPG surface.

3.2.2-Colloidal Probe Trials

A 58 µm colloidal sphere attached to PPP-BSI AFM tip was used and the results of a 32×32 force map obtained in 10×CMC TTAB using this colloidal probe on the TTAB layer on HOPG are shown in Figure 18. The force curve shown, Figure 18a, had a low gradient region at 3 nN, which was taken to be the break-through event. The break-through force was found to be ~3 nN in this curve and the retraction curve had noticeable bowing leading up to a flat region at 6 nN. This flat region was caused by the measured value exceeding the limit of the measurable deflection (12

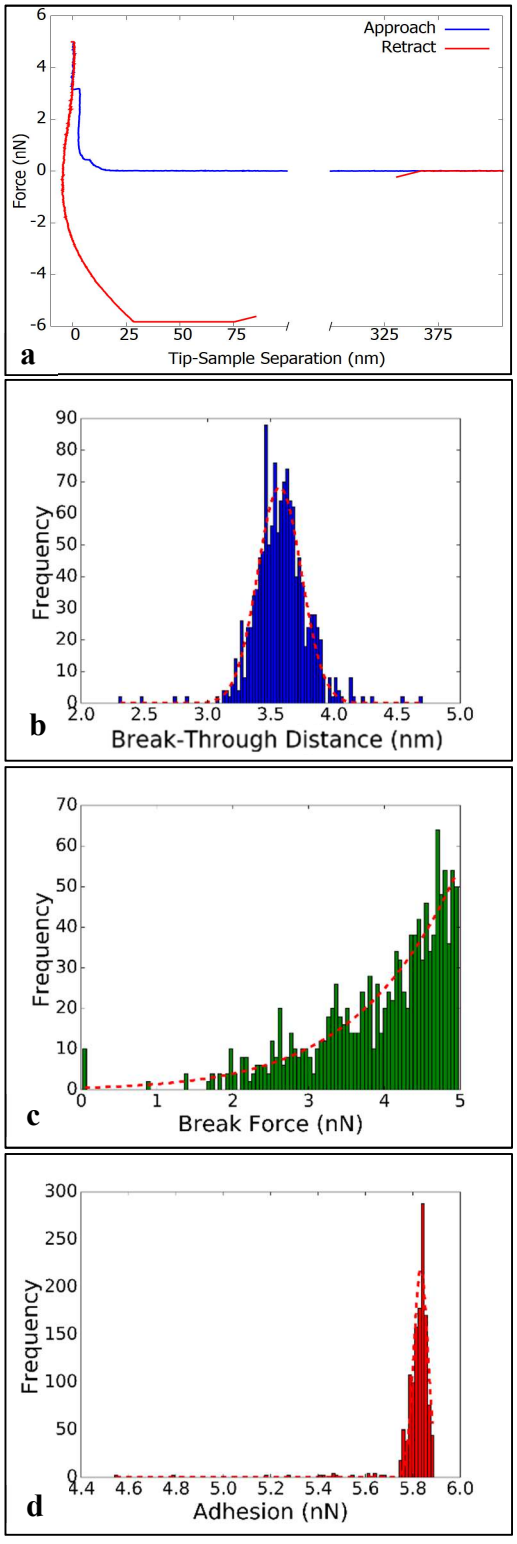

Figure 18. Example force curve (with split x-axis) and histograms of break-through distance, break-through force and adhesion for a colloidal probe on HOPG with 10×CMC TTAB

V, which corresponds to 6 nN after accounting for deflection sensitivity). The break-through distance obtained from the histogram in Figure 18b was 3.57 nm ± 0.17 nm, which is in the same range as values found in literature using various surface geometries. [26,87,105] As with the force curve, the histograms in Figure 18c and Figure 18d demonstrate how the measurable deflection limit affected the break-through force. Below the instrument limit of 5 nN the break-through force histogram shows what appears to be half of a normal Gaussian curve.

The low gradient at the break-through event resembles the curves found by Donaldson et al. when using a surface force apparatus (SFA) to study azo-TAB on mica.[22] In their work, there was a distinct difference in the appearance of the force curve and the break-through force for a light-switchable surfactant monolayer or bilayer. In the case of the bilayer, the break-through force was greater, and the force curves had a much lower gradient at the break-through event. Compared to the force curves found here, there is a resemblance between our colloidal probe curve profile and the azo-TAB bilayer, which would suggest hemifusion is occurring here, as was concluded in theirs and other work.[106]

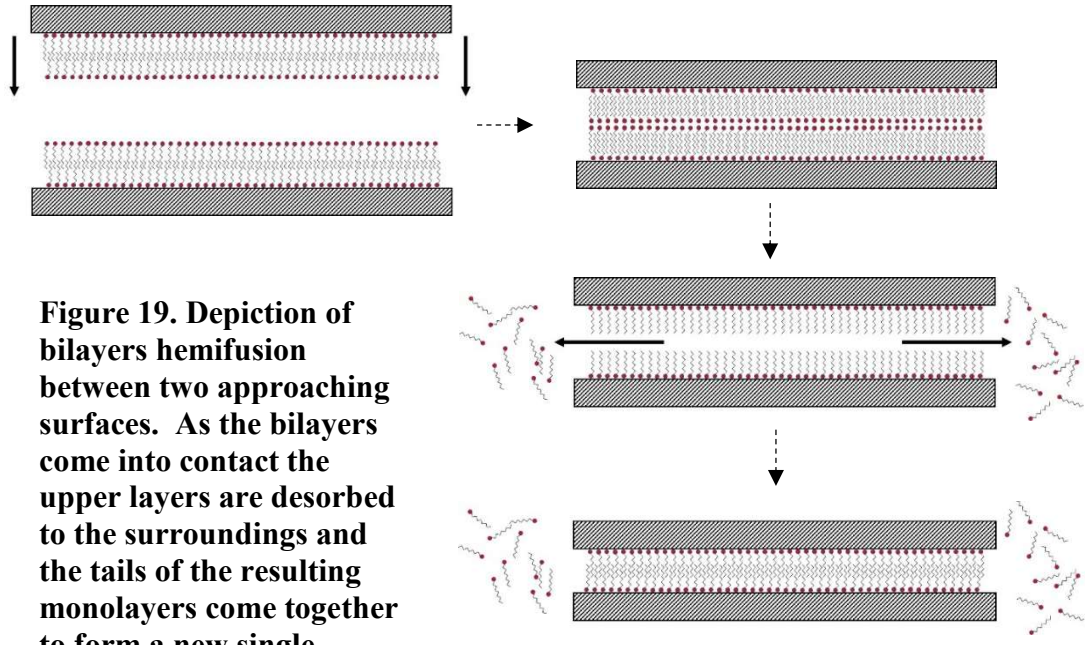

Figure 19. Depiction of bilayers hemifusion between two approaching surfaces. As the bilayers come into contact the upper layers are desorbed to the surroundings and the tails of the resulting monolayers come together to form a new single bilayer.

Hemifusion, represented in the scheme given in Figure 19, describes what happens when two hydrophilic surfaces, each supporting a bilayer, come into close contact. The repulsive forces generated by the bulk-facing headgroups lead to disruption of the opposing bilayers, resulting in the compression and rearrangement of the two separate aggregate layers to form a single layer between the two surfaces, with the simultaneous ejection of some surfactant.[22,106-108] Hemifusion also implies that adsorbed surfactant morphologies may change through interaction with another surface (two bilayers initially and one bilayer after interaction). Visual inspection of the force curves presented in the work of Donaldson et al. suggests a break-through distance (jump-in), which is approximately equal to the hemifusion distance, suggesting the possibility that the break-through distance represents the hemifusion distance rather than the surfactant layer thickness. However, previous work differs substantially from the work described in this section. Since HOPG has been shown to support the formation of a monolayer surfactant structure; i.e. instead of two bilayers with two mica SFA surfaces the

expected situation with HOPG and our colloidal probe is a monolayer and a bilayer. However, the measured break-through distance is characteristic of bilayer thickness, not monolayer plus bilayer.

To further investigate the identity of the break-through distance, force maps were collected on HOPG using regular AFM probes.

3.3.3-Flat Surfaces Sampled with Regular AFM Probe

3.3.3.1-HOPG Above the CMC

The data shown in Figure 20 represent the break-through event parameters for 10×CMC of TTAB on HOPG from a force map with side lengths of 500×500 nm.

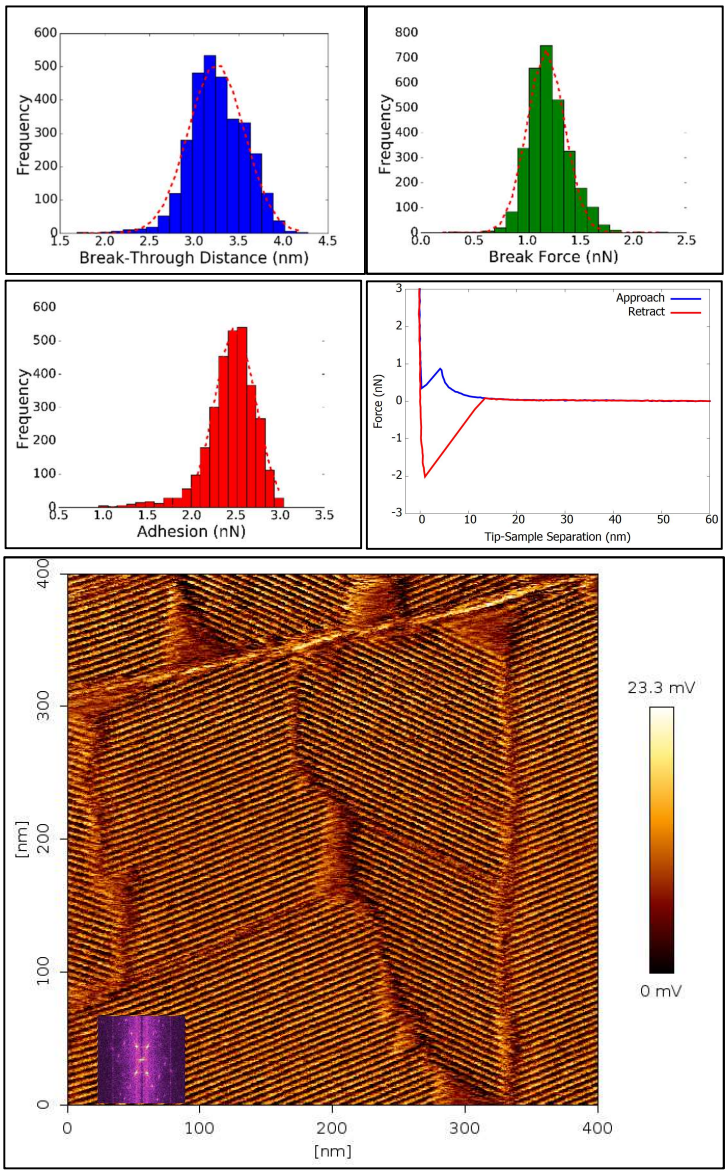

Figure 20. Histograms with Gaussian fitting results (red dotted line) and soft contact image of 10×CMC TTAB on HOPG with PPP-BSI probe

The mean and standard deviation from fitting the break-through distance, break-through force and adhesion force histograms were found to be 3.25±0.31 nm, 1.18±0.18 nN and 2.49±0.2 nN, respectively. Imaging at this concentration showed parallel rows of

surfactant arranged in different orientations caused by grain boundaries on the HOPG surface, which agrees with imaging found in previous investigations.[23] The parallel alignment and even spacing of the rows are due to the surfactant adsorbing conformally with the symmetry axes of the graphite substrate.[68,109] Fast Fourier Transform (FFT) analysis (overlay in the lower left of the soft contact image in Figure 20) was used to determine the period (rationalized as the sum of the width of a micellar aggregate and distance between aggregates), which was 4.7 nm, matching values found in the literature.[70]

Comparison of several surfactant break-through distance values on HOPG shows a similar range of values as observed in our work, suggesting that a future force mapping/histogram study involving surfactants of various chain length and headgroup charge would be beneficial in verifying the nature of the break-through distance.[23,25,27,81,103]

For the purposes of this paper, it is noted that the HOPG break-through values obtained using the regular AFM probe here are like those found on HOPG using a colloidal probe discussed above. It is well accepted that ionic surfactants form monolayers or hemi-spheres/hemi-cylinders on hydrophobic surfaces (e.g. HOPG) and bilayer or full sphere/cylinder aggregates on form on hydrophilic surfaces.[7,17,69,110] Therefore, this agreement is surprising; for the case of a colloidal probe and HOPG a bilayer and a monolayer are expected while in the case of an AFM tip and HOPG a monolayer and a monolayer are expected. Therefore, we expected a greater break-through distance for the colloidal probe vs. the normal AFM tip. This curious discrepancy will be elaborated upon in the “further discussion” section.

3.3.3.2-HOPG below the CMC

Adsorption of 0.5×CMC TTAB on HOPG was investigated using a 500×500 nm side length force map and soft contact imaging, and the results are given in Figure 21. The mean break-through distance, break-through force, and adhesion force were found to be

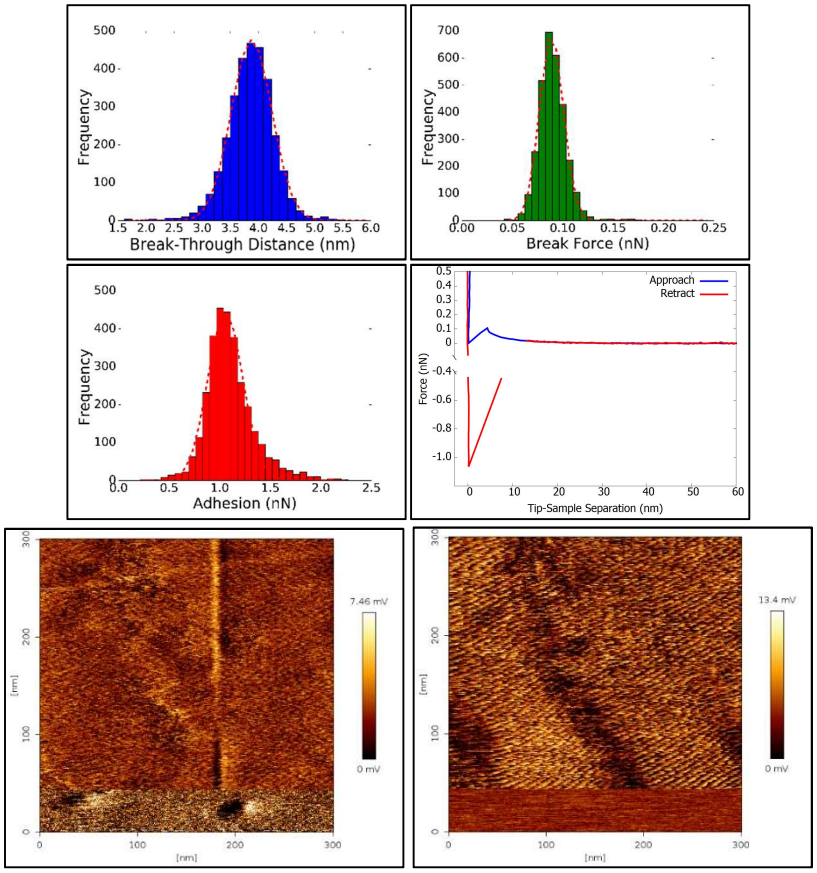

Figure 21. Histograms of break-through distance, break-through force and adhesion force of 0.5×CMC TTAB on HOPG along with the Gaussian fit results (red dotted line) and an example force curve (with split y-axis). Below are the error (left) and lateral deflection (right) images at the same concentration. In these images the scan direction is from bottom to top.

3.88±0.37 nm, 0.09±0.012 nN, and 1.06±0.17 nN, respectively. The break-through distance obtained at 0.5×CMC is about 0.5 nm higher than that obtained at 10×CMC TTAB, while the break-through force is 10% that obtained at 10×CMC. The large difference in break-through force was expected, given that SFA experiments showed a drop in break-through force below the CMC to 15% of the value measured above the CMC.[87] Given the patchy nature of adsorption that will be proven later in this paper,

the low break-through force is likely a result of surfactant being more easily moved by an approaching AFM tip.

With soft contact imaging, scanning 'above' the surfactant layer without breaking through to the underlying substrate was difficult below the CMC. The typical indication of break-through during scanning was the disappearance of surfactant from the image (either in height or error signals) mid-scan, or a sudden change in the lateral deflection signal (i.e., increased friction once the probe contacts the surface). Also, there was very little resolution of surfactant in the height or error images until post break-through, after which the parallel lines of surfactant are observable, albeit with rougher edges between the rows of surfactant when compared to images obtained above the CMC.

The ability to image surfactant aggregates below the CMC indicated that the surface concentration where cooperative interactions are responsible for adsorption of TTAB was less than 0.5×CMC, which is not surprising given that SDS has been imaged at 1/3 of its CMC.[25] As the surfactant assemblies on the surface are patchy below the CMC, the approach of an AFM tip could cause dynamic surface reconfiguration, a process which is expected to be much faster than scanning timescales (individual surfactant adsorption-desorption times tend to be on the order of milliseconds). Therefore, a probe at the hard surface could be scanning within the micelle layer, which could yield a variation in the friction sampled by the probe, accounting for the similar imaging in the friction signal post break-through (bottom right image in Figure 21).

3.3.3.3-HOPG Concentration Gradient

Next, a concentration gradient was performed using the batch method of data acquisition. The data in Figure 22 show break-through distance, break-through force, and adhesion force for TTAB on HOPG for concentrations between 0.5×CMC and 10×CMC using two different PPP-BSI probes, nominally with the same characteristics. The break-through distance did not change appreciably over the concentration range from 0.7×CMC to 10×CMC, remaining between 2.8 nm and 3.4 nm. Ignoring the data at 0.7×CMC, the break-through force does seem to increase with concentration through the CMC. This result differs from a previous SFA investigation for lipid bilayers, in which the break-through forces below the CMC varied and achieved a plateau above the CMC.[87] However, the behavior of the break-through force with concentration was also measured with different results in perfusion experiments, which will be detailed later. Comparing different concentrations in perfusion experiments is expected to yield better results vs. comparing different concentrations in batch experiments as will be discussed more completely below.

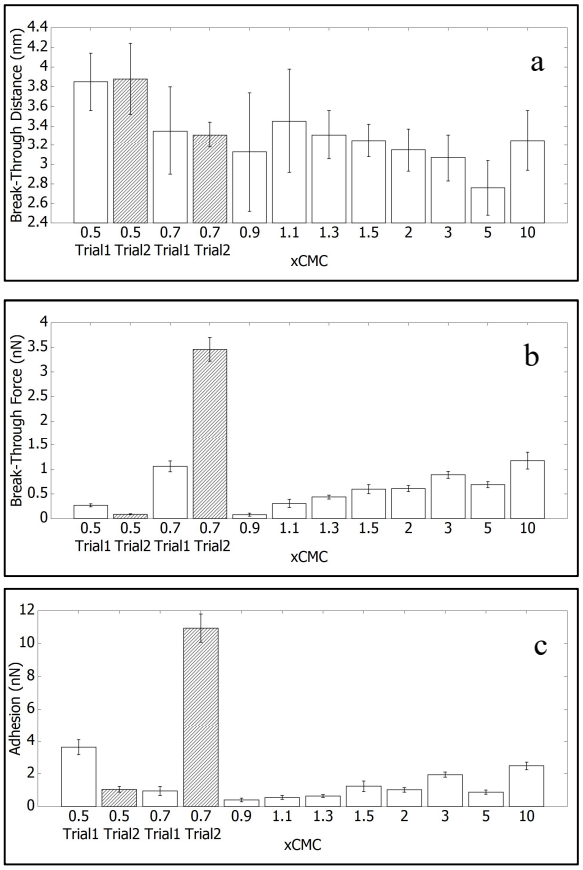

Figure 22. Break-through distance (a), break-through force (b) and adhesion (c) results for various concentrations of TTAB on HOPG. Different colors represent different probes.

The clear difference in break-through force and adhesion force values for trials 1 and 2 of the 0.5×CMC and 0.7×CMC indicates a variation not previously reported in the literature. This difference in break-through force between different trials using conventional AFM probes with nominally the same characteristics is attributed to differences in probe geometry at the nanometer scale, a conclusion supported by the fact that the break-through forces obtained with the colloidal probe were substantially different not only in value but also in appearance (a very low positive gradient in the force vs. distance curve, which was instead high when using the regular AFM probes). However, the break-through distance values between a regular AFM probe and a colloidal probe were unchanged which indicates that the probe shape and size had no effect on the break-through distance measurements. The effects of using a probe with a different force constant on the break-through values were investigated next.

3.3.4-MSCT Probe "f" Trials

To study the effect of probe characteristics on break-through behavior, an f probe of the MSCT cantilever which had a stiffness ~6 times greater than the PPP-BSI probes was used. The results from force maps obtained using the PPP-BSI probe and the f probe of the MSCT cantilever for HOPG, silica and silanated silica in 10×CMC TTAB are shown in Figure 23. Break-through distances did vary moderately beyond experimental error for some samples, but the unvarying nature was maintained between all surfaces and probes used.

Comparison of break-through force and adhesion force shows more substantial variations between surfaces and between distinct types of probes. It was found that the MSCT probe yields higher values in all cases, except for the adhesion force on silica.

However, no consistent proportional relationship between the data collected with the different probes was observed. Overall, these results support our conclusion that the cantilever type does not strongly affect the measurement of the break-through distance; the average values of all three surfaces is about 3.65 nm for both probes. Conversely, both the break-through force and adhesion force are strongly probe/cantilever dependent.

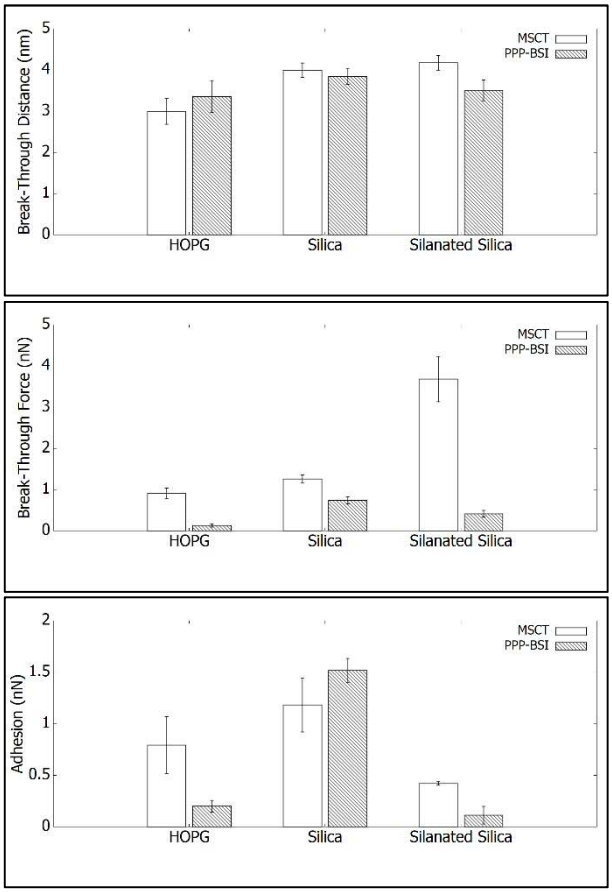

Figure 23. Break-through distance, break-through force and adhesion force using the PPP-BSI probe and the MSCT probe f at 10×CMC TTAB.

3.3.5-Perfusion Experiments

The following section will present data collected using the perfusion method on HOPG, silica and silanated silica. Visual data will be compared using gradient maps and then quantitative data will be obtained using the histogram analysis.

3.3.5.1-HOPG

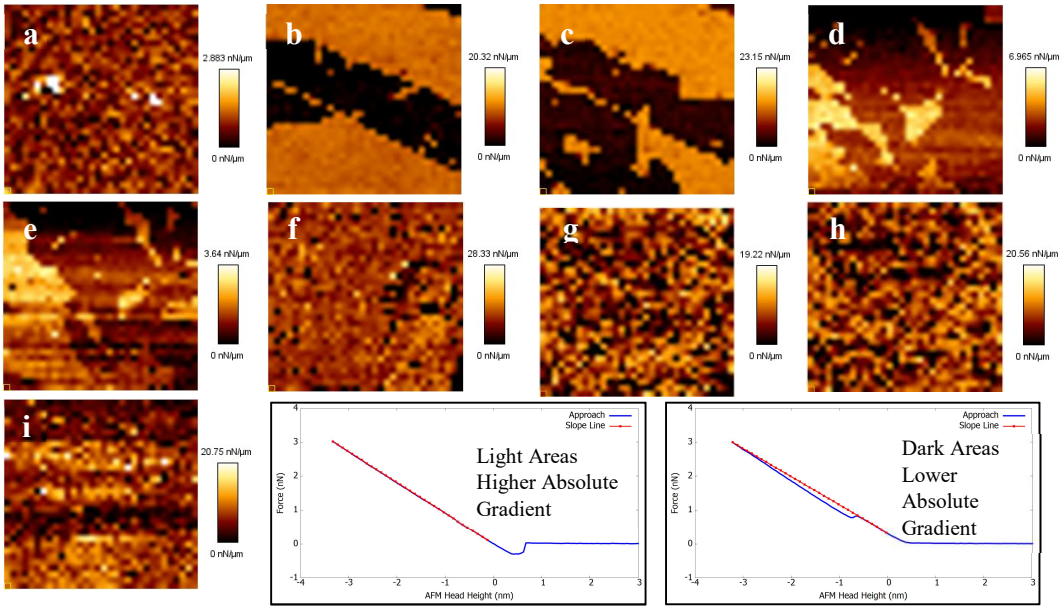

Figure 24. TTAB on HOPG-32x32 gradient maps. (a) Water (b)0.2×CMC (c) 0.2×CMC Scan 2 (d) 0.4×CMC (e) 0.6×CMC (f) 0.8×CMC (g) 2×CMC (h) 5×CMC (i) 10×CMC. All images are 5µm × 5 µm. The force curves explain the difference between the areas of high absolute (i.e. more negative) gradient (light color on gradient map) and low absolute gradient (dark color on gradient map).

During perfusion experiments the same area of adsorption can be studied as the concentration varies, reducing the opportunity for any change in the cantilever properties to occur. Our results are described below, starting from a discussion on the qualitative features of the micrographs. Discussion of the break-through force, adhesion force and break-through distance will follow.

Figure 24 shows the results of perfusion experiments for pure water and TTAB at concentrations between 0.2 and 10×CMC of TTAB on HOPG. In the bottom right of Figure 24 are shown force curves, which differ from those shown previously in that there is no adjustment for deflection of the AFM cantilever and therefore the trace does not become vertical at zero on the x-axis. By calculating gradient values in the approach curve between ~ zero on the x-axis and the maximum value before retraction was begun, it was possible to distinguish force map indices with and without break-through events during map collection. The light-colored areas in panels b–e are those in which a small or no break-through force was detected (the absolute value of the gradient is high) while the darker areas have yielded larger break-through forces (lower absolute gradient). The former is representative of little or no surfactant adsorption while the latter is representative of significant surfactant adsorption. Speckle patterns indicate insignificant variation in break-through force across the entire area of the image and are representative of little or no surfactant adsorption over the entire imaged area or a surface fully covered with surfactant (a and f-i, respectively).

In pure water (Figure 24a) the gradient image has no values that stand out appreciably from any of the others. When the surface is exposed to 0.2×CMC TTAB (Figure 24b), areas of largely differing gradient appear. The presence of areas of varying gradient suggests patchy adsorption of TTAB on HOPG. The map collected using 0.2×CMC was repeated immediately, and the second dataset is shown in Figure 24c. A similar patchy structure was observed, but additional patches appear in the second scan suggesting either additional adsorption over the course of one scan (20 min.) on areas previously without break-through events or rearrangement of already

adsorbed surfactant (i.e. adsorbed surfactant outside the field of view moving to inside the field of view). A more in-depth kinetic argument will be provided later in this section.

The height and lateral deflection maps (not shown) displayed no correlation with the gradient map, indicating that the break-through force heterogeneity was *not* caused by surface topography. As the bulk surfactant concentration was increased, the area of surface covered with high break-through forces also increased, as can be seen at 0.4 and 0.6×CMC (Figure 24d and Figure 24e, respectively). When 0.8×CMC was reached, Figure 24f, almost all the force curves displayed a break-through event which caused only small differences in gradient throughout the 5×5 μm region, resulting in the same speckle pattern noted previously, indicating the layer was complete in the observed region. Further increases in surfactant concentration, Figure 24g-i, do not change the appearance of the layer, supporting the conclusion that the layer was complete and unchanged above the CMC.

3.3.5.2-Silica

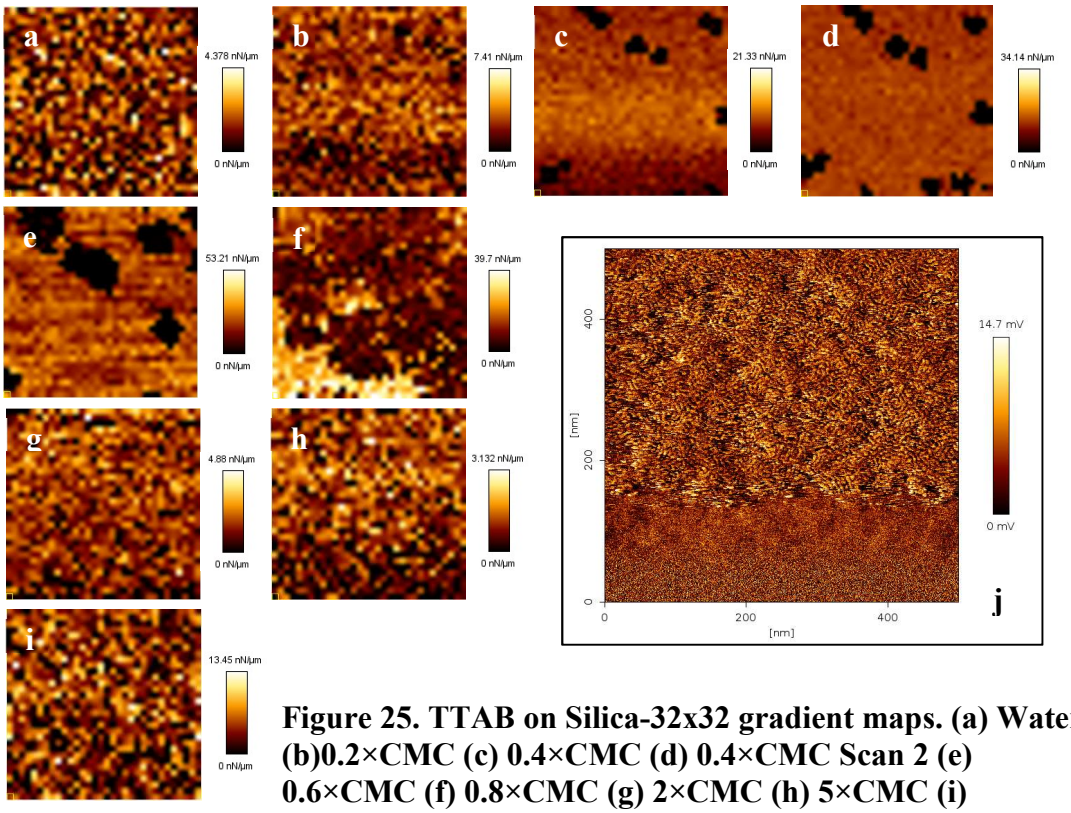

Figure 25. TTAB on Silica-32x32 gradient maps. (a) Water (b)0.2×CMC (c) 0.4×CMC (d) 0.4×CMC Scan 2 (e) 0.6×CMC (f) 0.8×CMC (g) 2×CMC (h) 5×CMC (i) 10×CMC. All maps are 5 µm × 5 µm. (j) 500 × 500 nm soft contact image of 2×CMC TTAB on silica (obtained separately using batch method) using the normal aspect ratio probe.

Despite the difference in surface chemistry and wettability, the gradient maps obtained on silica (results shown in Figure 25) were like those observed on HOPG. For both pure water and 0.2×CMC TTAB, the appearance of the gradient maps (Figure 25a and Figure 25b, respectively) is the random speckle pattern, indicative of no variation in adsorption across the area of the surface. At 0.4×CMC, shown in Figure 25c and Figure 25d, small dark areas indicative of surfactant patches began to appear between subsequent scans. The fractional area covered by these patches increased between Scan 1 and Scan 2, although in this case the size of the patches was relatively constant with time. Conversely, on HOPG the size of the patches increased without an increase in their number. In fact, on HOPG the nucleation probability seems to be much less than

the growth rate (compare 10c, 10d and 10e vs. 9b and 9c). Such a result is not surprising given the templating effect of the bottom layer of adsorption on HOPG. Larger patches of adsorbed surfactant appeared upon increasing the concentration to 0.6×CMC on silica, Figure 25e. Increasing the concentration to 0.8×CMC, Figure 25g, further increased the surface coverage to completeness, which remained complete for concentrations above the CMC.

None of the temporal experiments showed a lower fraction of patch-covered area with increasing time, indicating that increases in the fraction of covered area with increasing time are primarily due to increases in adsorbed amounts. In fact, our quantitative results for the fraction of covered area suggest that AFM images could be used to quantitatively measure adsorption isotherms.

Soft contact imaging of 2×CMC TTAB on silica was performed to investigate the structure of the adsorbed aggregates. The image in Figure 25j was scanned from bottom to top and the force set-point was increased until disorganized bundles of wormlike micelles became visible at around the 150 nm mark. Some difficulty occurred in acquiring images of these surfactant aggregates on silica as the probe did not remain stably above them long enough to obtain complete images, despite the several attempts we made. The reason for this difficulty is thought to be that the force required to image the surfactant aggregates was too close to the break-through force to allow for sustained soft contact imaging.

3.3.5.3-Silanated Silica

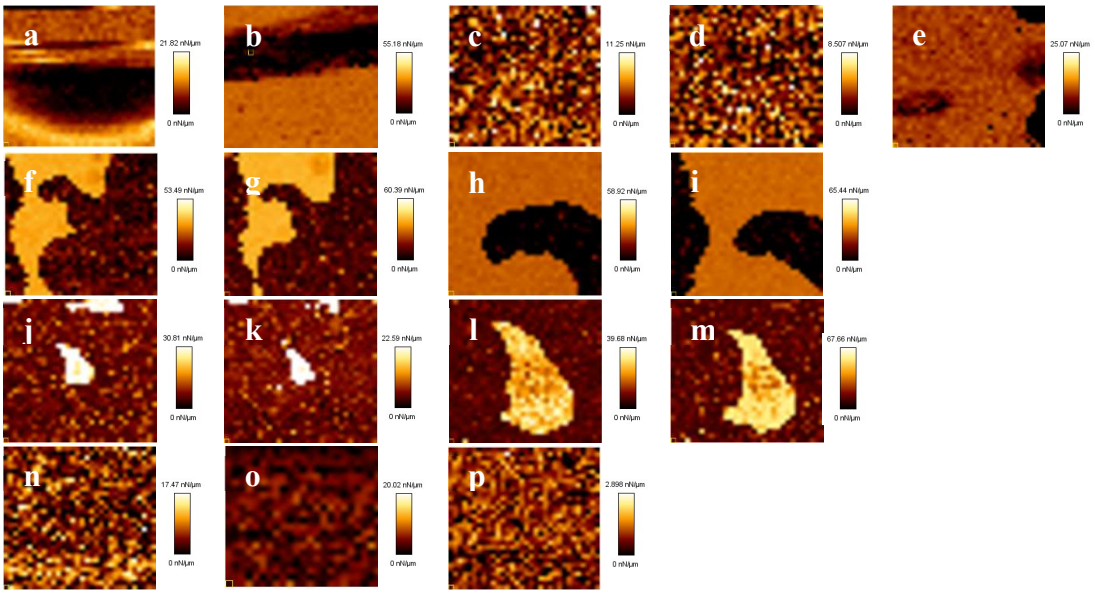

Figure 26. TTAB on Silanated Silica-32×32 force maps

(a) Water-5 µm
(b) 0.2×CMC-5 µm
(c) 0.4×CMC-5 µm
(d) 0.6×CMC-5 µm
(e) 0.6×CMC-5 µm- Scan2
(f) 0.6×CMC-50 µm
(g) 0.6×CMC-50 µm-Scan2
(h) 0.6×CMC-15 µm
(i) 0.6×CMC-15 µm-Scan 2
(j) 0.8×CMC-50 µm
(k) 0.8×CMC-50 µm-Scan 2
(l) 0.8×CMC-15 µm
(m) 0.8×CMC-15 µm-Scan 2
(n) 2×CMC-50 µm
(o) 5×CMC-25 µm
(p) 10×CMC-50 µm

Gradient maps obtained on the silanated silica surface are shown in Figure 26. Although no break-through events were observed in the force curves obtained in water (Figure 26a), there was some variability across the map, likely caused by a bubble on the surface. Introduction of 0.2×CMC TTAB also displayed some differences in the gradient of the curves over the 5 µm area investigated, which again were likely caused by a bubble present on the surface, which moved during the collection of the force map. Surprisingly, increasing the concentration to 0.4×CMC showed a featureless surface, which appeared unchanged even when exposed to 0.6×CMC, as seen in Figure 26c and Figure 26d, respectively. However, the second 0.6×CMC map shown in Figure 26 did

show two areas with break-through events in areas previously without such a feature (upper and lower right corners).

To investigate these low gradient areas further, the map size was increased to 50 μm for the two subsequent maps shown in Figure 26f and Figure 26g. Acquiring these datasets correspond to adsorption times of 70 minutes and 90 minutes at the end of each scan, respectively. The maps we collected showed non-uniform patterns, which were dynamic, as demonstrated by the slight differences in appearance between the two maps. The fractional area covered by surfactant corresponding to Figure 26f and Figure 26g was not statistically different, indicating that the different patterns were due to slight rearrangement of the patches. The resolution of the observed area was increased by decreasing the map side length to 15 μm for Figure 26h and Figure 26i, which were also collected immediately following the map in Figure 26g and hence correspond to adsorption times of 110 and 130 minutes, respectively. Again, differences between the two maps are present, which establish the dynamic nature of the features displayed in the maps and supporting the conclusion that these were patches of adsorbed surfactant.

It was also noted from Figure 26h and Figure 26i that the distance from the left most edge of the map to the left most edge of the patch in Figure 26h is larger than the distance between the two patches in Figure 26i, by ~2 map indices. In our opinion, this result not only supports the conclusion that the changes observed between maps are not caused by the lower resolution of the larger maps, but also that the appearance of movement by the surfactant patches is not caused by AFM drift. Our reasoning is that if the apparent movement of the patches was caused by drift of the area being mapped then the distance between the two patches would not change between maps.

Furthermore, since all movement of the AFM probe near the surface is vertical, the changes with time and concentration noted here are almost certainly not caused by lateral migration induced by the AFM probe.

The concentration was increased to 0.8×CMC and two subsequent scans were acquired with a size of 50 μm, shown in Figure 26j and Figure 26k. The area of lower gradient has grown to include almost the entire map area and the size of the only remaining area without an elevated break-through force shrinks from the first to the second scan, as can also been seen in Figure 26l and Figure 26m. Further, the relative change in the fraction of covered area at 30 and 50 minutes is smaller at higher concentrations as would be expected. Further increasing the concentration to 2, 5 and 10×CMC, displayed in Figure 26n, Figure 26o and Figure 26p, led to the disappearance of the areas with lower break-through forces, again supporting the conclusion of a fully developed layer at concentrations above the CMC.

The data displayed on HOPG, silica and silanated silica in the perfusion experiments clearly demonstrate patchy adsorption (patchy adsorption was not imaged in batch experiments because the image area was much smaller in those experiments), which has been commented on in literature, usually as a part of an overall adsorption scheme involving multiple regions.[1] At low concentrations, adsorption occurs via electrostatic interactions and the fraction of surface coverage begins to rise linearly, analogous to Henry's law used with gas adsorption. Further increases in concentration yield continued adsorption to the substrate, and lateral interactions between adsorbed molecules begins to occur, promoting the aggregation of adsorbed molecules and adsorption has a dependence on the concentration. Finally, near the CMC, adsorption

begins to reduce its dependency on concentration and eventually plateaus as an equilibrium between adsorption and desorption from the surface is reached.

The data obtained in this work agrees well with this phenomenological description, in that low concentrations displayed the expected patchy adsorption and those patches appear to grow with increasing concentration. Slightly below and above the CMC the maps become featureless which denotes the final region. We believe that this transition from patchy to featureless adsorption as concentration increases is the first time AFM force mapping has been used to show this behavior.

A kinetic argument can be used to determine whether changes in the maps on silica are due to adsorbing surfactant or to the migration of already adsorbed surfactant. Prior investigations studied the rate at which the similar cationic surfactant CTAB adsorbs to silica at different concentrations.[111-114] These studies agree that for concentrations above the CMC, adsorption reaches equilibrium within 30 seconds. Below the CMC the kinetics are varied, with reports of equilibrium being reached in seconds at concentrations below 0.5×CMC and the rate slowing significantly at concentrations near 0.6 mM (0.67×CMC). Both Pagac et al. and Atkin et al. observed equilibrium requiring between 11 and 3 hours at concentrations of 0.56×CMC and 0.67×CMC, respectively. As the concentration was further increased to 0.9×CMC, 90% of equilibrium was reached in only 25 minutes. In other words, the rate began decreasing at ~0.5×CMC and then increased as it was raised above 0.6×CMC.

Therefore, if we assume that TTAB behaves similarly to CTAB, we can infer that at low concentrations changes between maps are caused by surfactant migration rather than continued adsorption because each individual map was begun at least

10 minutes after surfactant was added and according to literature equilibrium is reached much more quickly. At 0.6×CMC, because equilibrium may not be reached for several hours, we cannot discriminate whether changes between maps were caused by surfactant migration or continued adsorption (although because the differences are in patch shape and not patch size, migration is more likely). At 0.8×CMC, changes were most likely due to migration rather than adsorption since 25 minutes were required for equilibrium for CTAB at 0.9×CMC in literature. For concentrations above the CMC, equilibrium should have been reached long before the maps were begun. Unfortunately, to our knowledge, no detailed kinetic studies have been reported on HOPG with a tetramethylammonium surfactant.

3.3.6-Histogram Analysis of Perfusion Experiments

A typical break-through distance, break-through force and adhesion force histogram for a force map on silanated silica is shown in Figure 27. As expected from the gradient maps, two peaks are found in the break-through distance and break-through

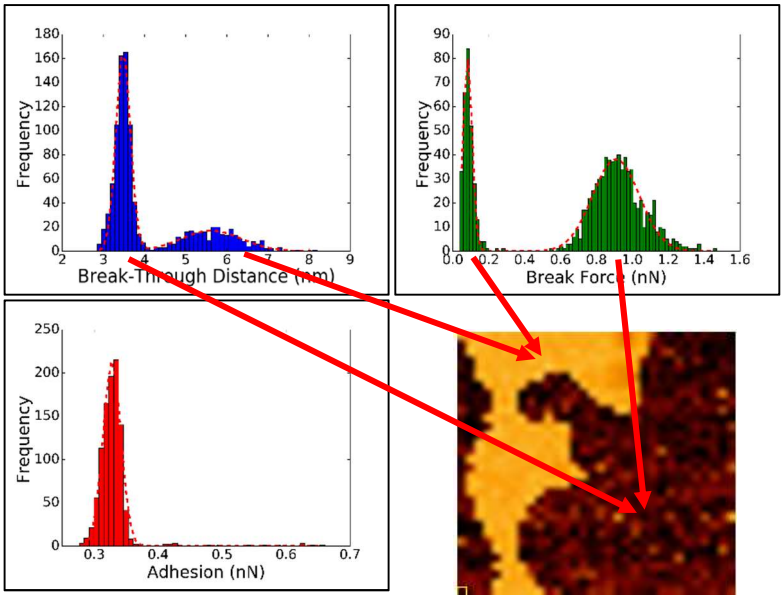

Figure 27. Break-through distance, break-through force and adhesion force histograms shown with gaussian fit results (red dotted line) for 0.6×CMC TTAB on silanated silica (Figure 26f, map shown here for reference).

force histograms, representing the two distinct areas. Equation 2 was used to fit the two means and standard deviations for the break-through distance and break-through force, and these values are given in Table 3. Note the break-through distances in batch experiments only showed one break-through distance and force peak because only areas with surfactant that could be soft contact imaged were mapped.

	Break-Through Distance (nm)		Break-Through Force (nN)	
	Peak 1	Peak 2	Peak 1	Peak 2
μ	3.48	5.62	0.08	0.91
σ	0.17	0.73	0.03	0.13

Table 3. Break-through distance and break-through force means and standard deviations for two peak fitting for 0.6×CMC TTAB on silanated silica (Figure 26f)

The presence of two distinct peaks in the histograms and areas in the gradient maps are consistent with the dark areas (low gradient) being those with a surfactant layer capable of resisting the probe while the light areas (high gradient) have a layer which repulses the probe very little or not at all. Because the break-through force in these areas was not zero (as it was for force curves in water) the presence of an adsorbed surfactant layer adsorbed in a flat configuration was considered. However, a flat layer does not make sense with a break-through distance larger than 3.48 nm because the break-through distance should be very small (i.e. the width of a surfactant molecule). The small break-through force could result from the surfactant present on the tip generating a weak and long-ranged electrostatic double layer. Although force interactions between surfactant on a tip and a lightly-covered surface has not been shown before, a weak, long-ranged electrostatic double-layer would explain the small

repulsive force between the tip and the substrate in areas with large break-through distances and makes more sense than a surface without some surfactant adsorbed.

The adhesion histogram had one main peak with mean 0.32±0.05 nN, which represents the dark (surfactant-rich) areas in the gradient map. Looking carefully at the adhesion force in Figure 27, the adhesion force in the light areas is represented by a spread of adhesion values greater than the main peak, demonstrated by the histogram bins between 0.4 nN and 0.65 nN. This spread of values occurs due to the fewer number of points in the areas without a substantial break-through force being spread out compared to the main peak, indicating the adhesion force was

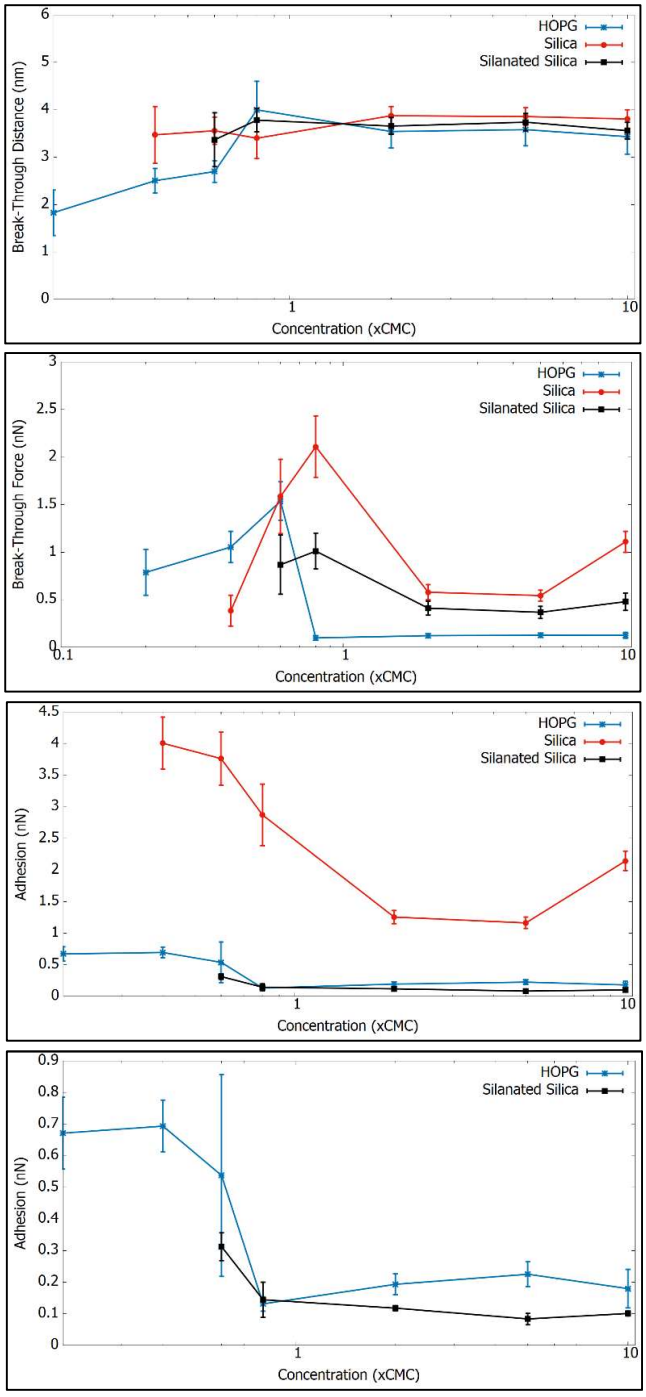

Figure 28. Break-through distance, break-through force and adhesion force from areas with surfactant on HOPG, silica and silanated silica at 0.2, 0.4, 0.6, 0.8, 2, 5 and 10×CMC of TTAB on logscale x-axis. The bottom image is a duplicate adhesion force without silica, to highlight the details of the other two surfaces.

more uniform in the dark areas compared to the light areas. Qualitatively, the adhesion force plots for the other two surfaces resembled those in Figure 27, as did the break-through distance and break-through force.

Using histogram analysis, the break-through distances, break-through forces and adhesion forces for the dark regions of the maps below the CMC and the entire map area above the CMC in Figure 24-Figure 26 were obtained and plotted in Figure 28. Values for the adhesion and break-through forces obtained across the three different surfaces should not be compared qualitatively because the same probes were not used. However, information obtained on one surface will be discussed as a function of surfactant concentration, as the tip was the same during each of these experiments.

The trend of the data on each surface shows that the break-through distances increased with increasing concentration until the CMC and then plateaued between 3.5 and 4 nm. The error associated with each value was greater below the CMC and decreased above the CMC, which we interpret as indicative of the micelle layer becoming more tightly packed above the CMC. We note that although isotherms in literature have also reported reaching the plateau region below the CMC, by far the most common result is that the start of the plateau region corresponds to the CMC. [13,115]

Break-through forces increased with increasing concentration until just below the CMC, where the values then decreased to a plateau for each surface. This is not the first time that the break-through force has been shown to increase using AFM force curves. Liu et al., Lokar et al. and Rabinovich et al. demonstrated increases in break-through force, with Liu et al. observing these increases over time at a constant

concentration and the other groups observing these results using with mixed surfactant systems.[28,116,117]

In our work, a temporal explanation for the increase is less likely as the values showed no increasing trend over the course of a single map. However, the works of Lokar and Rabinovich suggest that adding a second component to a surfactant solution led to the changes in break-through force, which lends support to the theory of adsorbed impurities as the cause for the increase in the break-through force seen here. Such impurities would adsorb below the CMC and then above the CMC partition to micelles; hence a larger break-through force just below the CMC. QCM results in our laboratory demonstrated the same qualitative type of behavior that were also caused by impurities at a very small level. Similar synergistic adsorption has been noted by Shi et al., who demonstrated increased adsorption and packing by using a co-solute.[57]

Above the CMC, the adhesion values for HOPG and silanated silica were constant with an increase of approximately 0.5 nN for the silica sample between 5×CMC and 10×CMC. We do not know the source of the increase.

3.3.7-Further discussion

Break-through distances between 3.5 and 4 nm are often found in literature using AFM and these values agree well with bilayer thicknesses found using other techniques such as neutron reflectivity and ellipsometry.[17,18,26,118] Soft contact imaging has revealed spherical or cylindrical micelles on silica both here and in other publications and as previously mentioned it is accepted that monolayer thickness structures (monolayers and hemi-cylinders/spheres) form on hydrophobic surfaces and bilayer thickness structures (bilayers and full cylinders/spheres) form on hydrophilic

surfaces. [26,65,68,77] Why then do the break-through distances differ only slightly between the hydrophilic and hydrophobic surfaces? Compression via the AFM probe was considered as to why the break-through distance values are so similar. However, using compression to explain the equivalence seems unlikely because other techniques involving no physical contact have been used to show a difference in the thickness of adsorbed surfactant when AFM could not, even when using similar surfaces.[17,18,64]

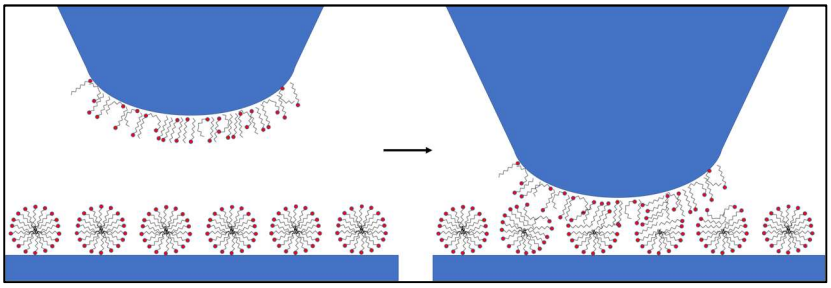

Figure 29. (Upper) Two AFM tips each with an adsorbed monolayer interacting and hemifusing to make a bilayer break-through distance. (Lower) AFM tip with adsorbed monolayer interacting with cylindrical layer on hydrophilic silica surface. Hemifusion between the upper part of the cylinder and the layer on the probe leads to bilayer break-through distance.

While our results alone are not irrefutable proof, the fact that the break-through distance of a surfactant layer on an AFM tip was found to be like those found on flat surfaces using colloidal and regular AFM probes increases the doubt that the break-through distance is a reliable measure of an isolated surface adsorbed surfactant layer thickness. Rephrasing our question, why is the break-through distance the same for two hydrophobic surfaces, two hydrophilic surfaces or one hydrophobic and one hydrophilic surface? Figure 29 addresses these some of these points.

First, we take the case of two monolayers, such as would be found between two AFM tips or between an AFM tip and a hydrophobic surface. In the case of an AFM tip, little is known about the orientation/packing of this layer, but we hypothesize that due to geometry and surface conditions the layer is not well packed and there are possibly molecules adsorbed in multiple orientations (although a majority will be tail down). As the two surfaces come into contact, there will be repulsion from molecules whose headgroups are facing the layer on the other surface and once the layers are in contact the tip breaks through both layers simultaneously to yield a bilayer thickness break-through distance.

Second, we consider the cases which have a bilayer present. Figure 19 and the associated discussion describes what happens when two bilayers are present as determined via SFA studies; the upper layers from each bilayer diffuse to the surrounding solution or reorient so that the tails of the surface adsorbed layers may interact and again a bilayer break-through distance results.

Next, the situation visualized in Figure 29, wherein a hydrophilic silica surface, which would have a bilayer, is approached by an AFM tip with an adsorbed monolayer. Reorientation of the bilayer (or perhaps desorption of surfactant from the tip given the likely disordered nature of the monolayer on the tip) results in a single bilayer between the probe and the surface prior to break-through. The same argument can be made in the case for a colloidal probe (adsorbed bilayer) and HOPG (hydrophobic flat surface); however, complete desorption of surfactant from HOPG seems unlikely as literature has shown that the monolayer on HOPG is irreversibly adsorbed due to the strong interaction between the tails of the surfactant and the graphene rings of HOPG.[119]

We were surprised in the case of one bilayer and one monolayer that the break-through distance matched that of a single bilayer because of the difficulties suggested by Figure 29. If correct, then this hypothesis regarding the hemifusion of surfactant between the surface and tip layers would explain why bilayers measured using contact free methods agree so closely with surfactant layers measured using AFM. It would be interesting to use a chemically-modified tip such as Pera et al. used to study lipid bilayers using force curves.[84] In their work, if the tip or surface were independently modified (so that only one bilayer was present) there was only one break-through event. However, if both the tip and the surface were modified then two break-through events were observed. Their chemical modification was thought to strengthen the adsorption of the lipid and produce bilayers on their AFM tips, which, along with the typical differences between adsorbed layers of lipid and surfactant, is most likely why we saw no double break-through events in our work. Also, we only studied the case where the surfactant was of opposite charge from the flat surface and tip; the case of like charge would be interesting to study although the surfactant/surface interaction would be decreased due to same charge repulsion.[120]

The ability to distinguish adsorbed patches using AFM gradient mapping has several implications for future research. For example, surface chemistry could be varied in a regular manner and adsorption as a function of surface chemistry could be measured. Once this is accomplished, the dimensions of the surface variation could be altered. Such a study would allow one to determine the length scale over which surface chemistry variation is important. This type of study would have relevance for corrosion since non-adsorption of a corrosion inhibitor at a very local area could be distinguished.

Real surfaces are very rarely molecularly smooth or chemically homogeneous; the techniques described in this paper are ideal for exploring how variations in topology or surface chemistry affect adsorption, providing experimental validation for recent simulation results.[49,50]

3.4-Surfactant Under Lateral Confinement

3.4.1-Soft Contact Imaging of Surfactants on Unconfined Silica

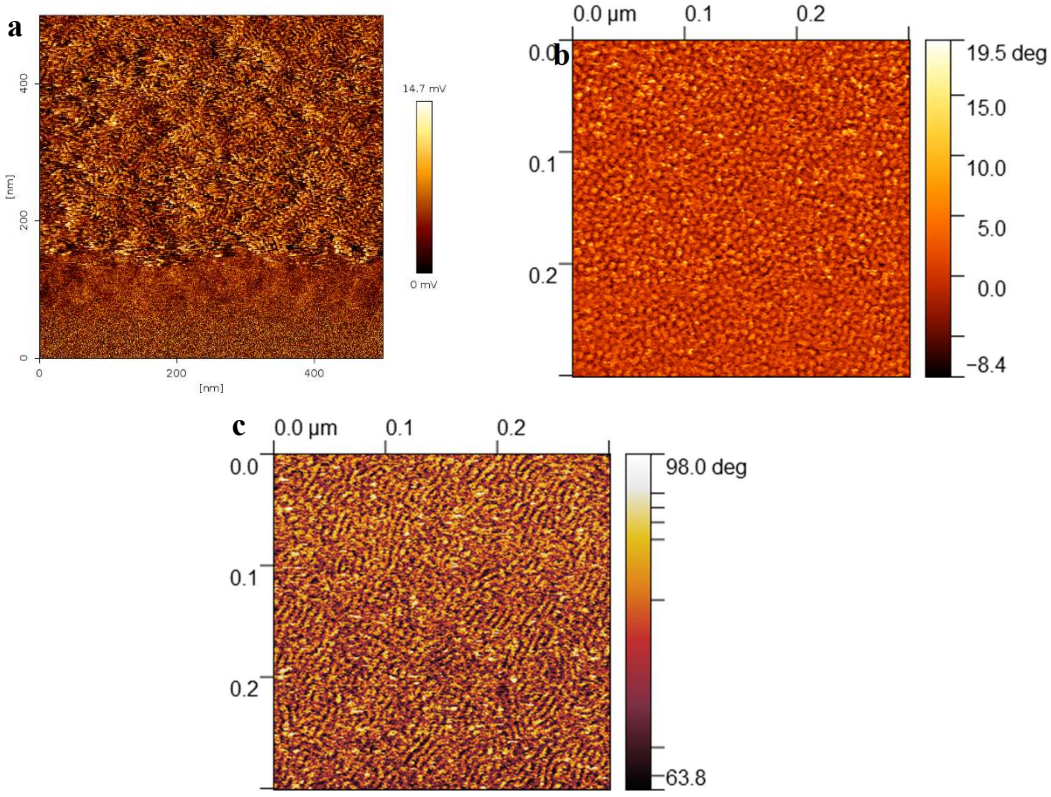

Figure 30. AFM images collected using the soft contact imaging method with (a) 2×CMC TTAB, (b) 10×CMC CPC at 20 minutes surfactant immersion and (c) 35 minutes surfactant immersion on silica. The TTAB image was collected using the JPK Nanowizard III while the CPC images were collected using an Asylum Cypher.

Soft contact imaging was used to collect images of 2×CMC TTAB on unconfined silica (meaning the surface was cleaned only and had no fabricated structures) using the JPK Nanowizard III. The image in Figure 30a is a deflection signal

and was scanned from bottom to top and the force setpoint was increased until disorganized bundles of wormlike micelles became visible at around the 150 nm mark. There was some difficulty in acquiring images of these surfactant aggregates on silica as the probe did not remain stably above them long enough to obtain complete images, despite several attempts. The reason for this difficulty is thought to be that the force required to image the surfactant aggregates was too close to the break-through force to allow for sustained soft contact imaging.

An Asylum Cypher with blueDrive technology was used to collect phase images of 10×CMC CPC aggregates on silica, shown in Figure 30b and Figure 30c. After 20 minutes immersion in CPC the aggregates were spherical, noted by the circular dots in the scan in Figure 30b. However, after 15 more minutes in solution the aggregate morphology had changed to worm-like micelles, seen as the disorganized rod like structures in Figure 30c. The morphology remained unchanged after another hour of imaging, suggesting the worm-like micelles were the equilibrium structure. Given that the surfactant concentration was significantly above the CMC, evaporation should not have caused this result. We are unsure of the reason for this shift in morphology, but one possible explanation could be that the hydrophilicity of the silica acquired from the UV Ozone cleaning was changing with time to an equilibrium value, causing the morphology on the surface to shift as well. Force maps were collected after a minimum of 35 minutes in solution to eliminate any temporal effects on the surface aggregates.

3.4.2-Force Curve Comparison and Validity

Force maps on unconfined silica were collected and analyzed at 10×CMC TTAB using a procedure described in a previous publication by our group.[121] The UV-

Ozone cleaned silica had break-through distance values between 3.5 nm and 4.0 nm, while the break-through force values varied from 1.1 nN to 0.1 nN and the adhesion force values varied from 2.2 nN to 0.18 nN. Previously we showed that break-through distance varied with concentration below the CMC but did not vary with concentration above the CMC and was independent of surface and or tip characteristics. The break-through and adhesion forces, however, did vary with tip characteristics and should only be compared when the tip is precisely the same, i.e. no tip cleaning between trials. Therefore, values on single surfaces (polymer, trench, and wheel center values) can be compared, but unconfined clean silica values cannot be quantitatively compared except with respect to breakthrough distance.

3.4.3-Trenches

In this section the force mapping characterization is applied to surfactant adsorbed on the floor of trenches fabricated in polymer with different surface chemistries. The break-through event values are compared for different trench widths and polymer content and a discussion on various aspects of the interactions between the surfactant solution and the polymer is provided.

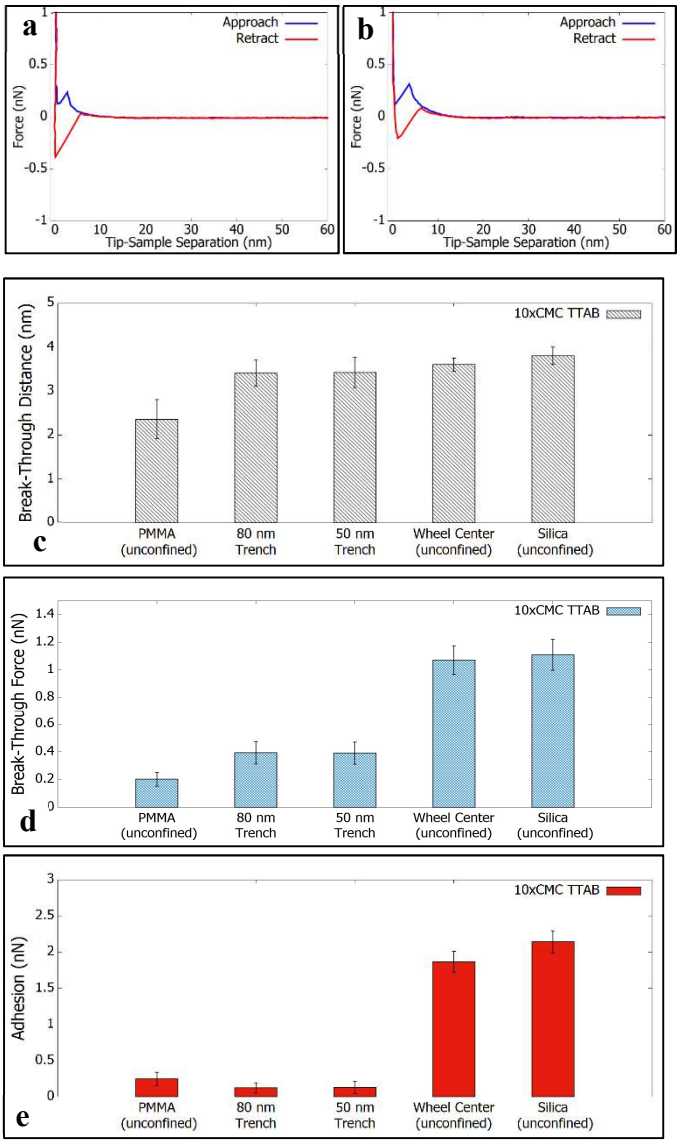

Figure 31. Force curves using 10×CMC TTAB on (a) unconfined PMMA and (b) in a 50 nm PMMA trench and (c) break-through distance, (d) break-through force and (e) adhesion force values collected from force maps in various locations

3.4.3.1-10×CMC TTAB-PMMA

A concern was that the polymer would not remain stable immersed in the surfactant solution. However, PMMA showed no noticeable effects of being in solution during data collection. Longer times in solution were tested and it was found that at ~5 hours small bubbles would develop at the surface of the polymer. However, even there were no observable effects

of swelling or polymer deformation, the data shown here was collected in less than 3 hours of sample immersion.

Example force curves from the unconfined PMMA and at the bottom of the 50 nm trench are shown in Figure 31a and Figure 31b, respectively. Break-through events occurred in both locations, indicating adsorbed surfactant with a stable structure able to resist the force of the AFM probe. The break-through values obtained from multiple force curves on unconfined PMMA, at the center section of the PMMA wheel (serving as an unconfined silica surface which was previously covered with polymer) and from the 80 nm and 50 nm wide trenches are shown in Figure 31c-e. The values from unconfined PMMA and PMMA wheel centers were obtained using a full 32 × 32 grid while the values confined at the bottom of the trenches were obtained from all viable curves collected on the floor of the trenches, typically between 40 and 50. A clean unconfined silica surface (which had never been in contact with polymer) was also measured at the same surfactant and concentrations used for the confined surface trials.

Comparing just the trench-related surfaces (PMMA, in trenches and in wheel center) it was found that the break-through distances did not vary except on the PMMA surface. In our previous paper, we examined 3 surfaces with 3 different types of tips and found no difference in break-through distance above the CMC even though surfaces were chosen to encompass both monolayers and bilayers.[121] The unconfined PMMA breakthrough force suggests only a monolayer is being probed, which means that surfactant was either not adsorbing on PMMA (break-through of the layer on the tip only) or surfactant was lying flat on the PMMA.

The break-through distance did not vary between the 80 nm trench, 50 nm trench, and the unconfined wheel center. The values in those locations were like those found on clean silica as well. The break-through forces, however, did vary with location. Force maps collected on the unconfined PMMA surface had the smallest break-through forces, about ½ of the 0.4 nN collected for the 50 and 80 nm trenches. The unconfined wheel center had break-through values of ~1.1 nN. Similar but inverse trends were found in the adhesion values, which decreased from the wheel center to the trench values and then increased slightly on the unconfined PMMA surface. We found previously that an increase in break-through force was observed with an increase in concentration below the CMC; consistent with this observation, these results indicate confinement caused a reduction in ordering of the adsorbed layer which in turn was responsible for the reduction in adhesion and break-through force.[121]

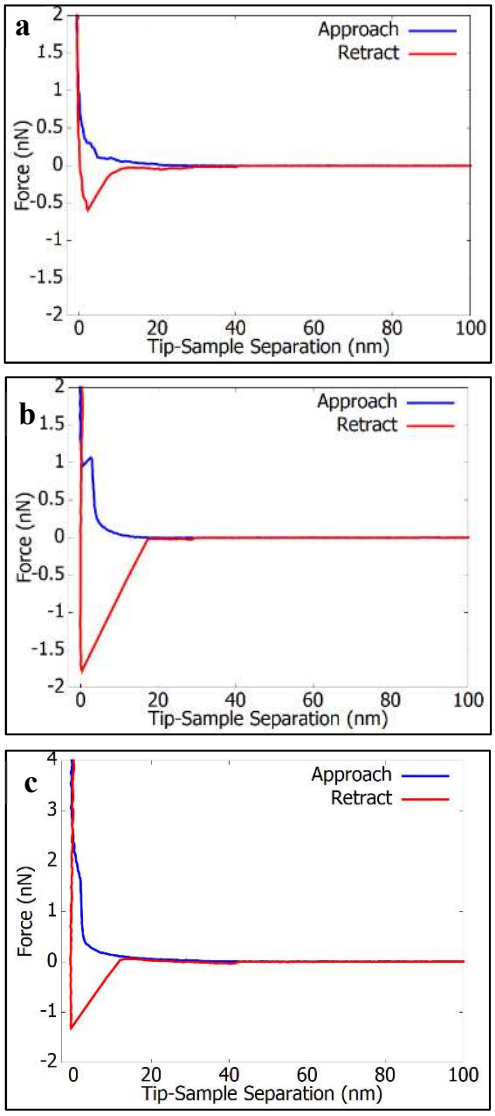

Figure 32. Force curves on (a) unconfined PMMA/MAA(8.5), (b) in the center of a PMMA/MAA(8.5) trench and, (c) in the center of a PMMA/MAA(17.5) trench.

3.4.3.2-10×CMC TTAB-PMMA/MAA

When polymer containing MAA was used there was no clear break-through event on either the PMMA/MAA(8.5), demonstrated in the force curve in Figure 32a, or

the PMMA/MAA(17.5) polymers. However, force curves collected on the exposed silica of the PMMA/MAA(8.5) sample, shown in Figure 32b, had clear break-through events. Force curves on the exposed silica on the PMMA/MAA(17.5) samples, represented in Figure 32c, did not have a sharp break-through event, but rather a repulsive force and then a "pseudo break-though", i.e. a region where the distance between the tip and sample was constant and at a certain point began to gradually decrease to zero.

Possible explanations for the resulting break-through event characteristics are that the MAA destabilizes the surfactant layer while also leaving behind a thin residue with some MAA content on the silica. This residue would have to be very thin because metal remained on the silica surface where the trenches were, which we would not expect if polymer remained at the bottom of the trench after e-beam lithography development. However, as this is a form of contamination we cannot account for the accuracy of the break-through event values and therefore have instead drawn conclusions regarding the interaction between the surfactant and the surface chemistry based on the location and occurrence of break-through events.

Destabilization of the surfactant layer by the MAA would explain why there is a sharp break-through event on the PMMA but not the PMMA/MAA polymers and if the MAA content of any residue left by the polymer was dependent on the polymer acid number it might explain why there are sharp break-through events in the PMMA/MAA(8.5) trenches but not on the PMMA/MAA(8.5) polymer itself (some MAA character on the silica but not enough to destabilize completely) and why the break-through event sharpness is decreased in the PMMA/MAA(17.5) trenches (more

MAA character on the silica so some destabilization but not enough to prevent generation of a repulsive layer).

The difference between the pure PMMA and PMMA/MAA polymer is also suggested by the interaction with the surfactant solution. While the pure PMMA was unchanged by immersion in solution, both types of the MAA containing polymer began to display bubbles on the surface after ~2-2.5 hours and within another 90 minutes noticeable swelling and some dissolution occurred. Therefore, all force curves shown here were collected prior to any signs of bubbles on the polymers. Also, as these effects appear to be isolated to the MAA containing polymers the same influences are not expected in the data collected using pure PMMA, hence why quantitative conclusions could be drawn.

3.4.3.3-10×CMC CPC-PMMA

When the PMMA wheel array was submersed in 10×CMC CPC there was no noticeable bubble formation until ~4 hours of exposure to the surfactant, slightly quicker than with TTAB. However, as with TTAB, even though there was no noticeable swelling even with the bubble formation, all data was collected at less than 3 hours after sample immersion. Clear break-through events, shown in Figure 33a and Figure 33b, occurred on the PMMA surface, indicating the presence of a stable layer on the surface of the polymer. Break-through events were found in all locations, and results are shown in Figure 33c-e. On the PMMA surface the

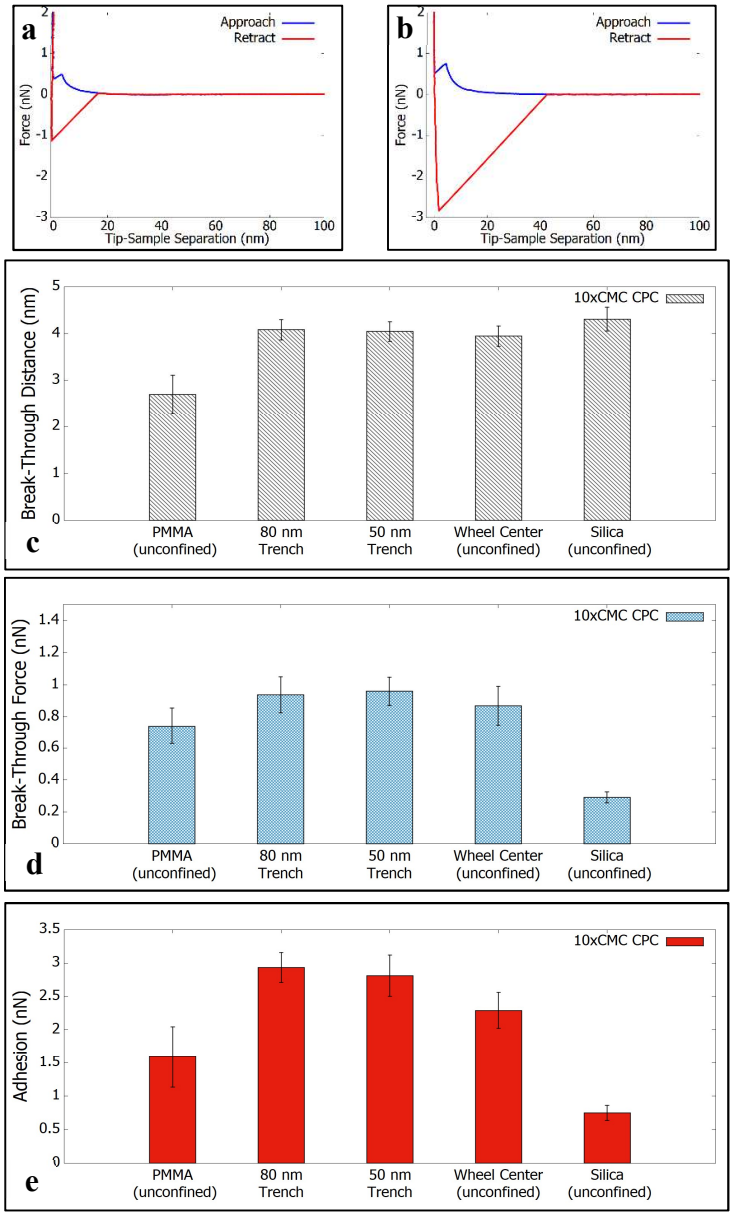

Figure 33. Force curves using 10×CMC CPC on (a) unconfined PMMA and (b) in a 50 nm PMMA trench and (c) break-through distance, (d) break-through force and (e) adhesion force values collected from force maps in various locations.

break-through distance was like that found for TTAB on the PMMA surface, approximately 2.1 nm. Again, as seen with TTAB, the break-through distance increases on surfaces where the polymer was removed, displaying values between 3.7 nm and 3.5 nm for the trench floors and wheel center. The break-through force and adhesion values showed increases from the PMMA to the trenches (0.8 nN to 1 nN for break-through force and 1.5 nN to 3 nN for adhesion, respectively) but the value remained roughly the same between the trenches and the wheel center for the break-through force. Adhesion force values were smaller for the unconfined surface. The force behavior is markedly different for the CPC vs. the TTAB; the latter showed substantially higher forces for the unconfined wheel center than for the trenches. These results indicate that the identity of the surfactant can affect the confinement effect.

3.4.3.4-10×CMC CPC-PMMA/MAA

When PMMA/MAA(8.5) copolymer was used, there was noticeable bubble formation with minutes of being exposed to the surfactant and swelling with 30 minutes of being exposed. Shortly after that, dissolution of the copolymer layer occurred, demonstrated in Figure 34b. After 1 hour in solution, wheel 1 had bubbles covering it while wheels 2 and 3 were visually unaltered. However, the middle width trenches (wheels 4 through 6) had signs of the polymer being removed from the surface and wheels 6-8 had larger sections missing. Lastly, wheels 9-12 were completely removed within the 90 minutes of immersion.

The swelling and dissolution appeared to be related to the beam dose, with the lowest beam dose (wheel 1) having bubbles on its

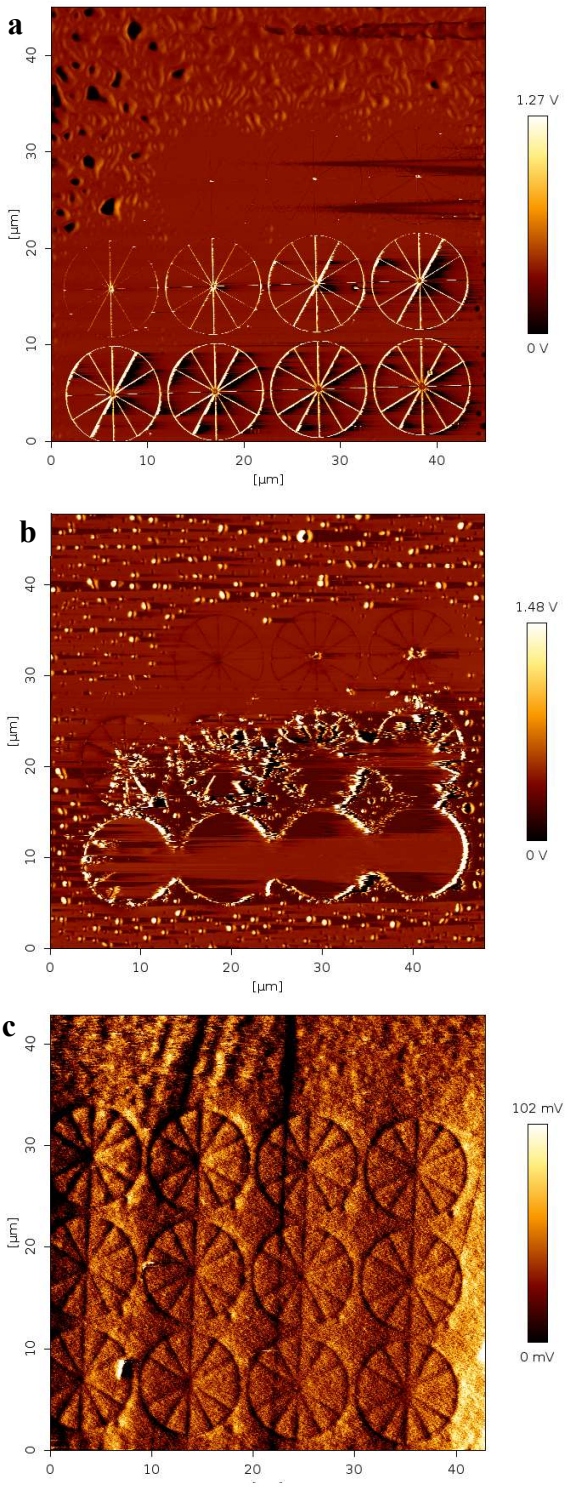

Figure 34. (a) PMMA wheel array at 5 hours, (b) PMMA/MAA(8.5) wheel array at 2 hours and (c) PMMA/MAA(17.5) wheel array at 2 hours in 10×CMC CPC at 2 hours of immersion in surfactant.

surface while high beam doses do not have bubbles but do experience swelling and dissolution. Dissolution is shown between the last two rows of wheels (wheels 5-8 and wheels 9-12) indicating that dissolution of the polymer is affected by e-beam exposure. Specifically, a higher beam dose extends dissolution further from the intended exposure points. The PMMA/MAA(17.5) polymer, shown in Figure 34c, had similar results in that swelling occurred within 30 minutes of immersion in surfactant but did not dissolve. After 2 hours, however, the polymer had not dissolved away from the surface as it did with PMMA/MAA(8.5).

The speed at which swelling and dissolution occurred was an unexpected outcome of increasing the MAA content of the polymer and did not allow for any measurements to be obtained in the trenches. The PMMA/MAA(8.5) and the PMMA/MAA(17.5) polymers dissolved and swelled while the pure PMMA experienced neither, suggesting that CPC is helping to dissolve the copolymer via interaction with the MAA units. Because the results appear to be dose dependent, CPC solution may act as a developer, i.e. removing the e-beam exposed polymer from the silica surface. Why the polymer dissolved for PMMA/MAA(8.5) and only swelled for PMMA/MAA(17.5) is unknown.

3.5-Pillars

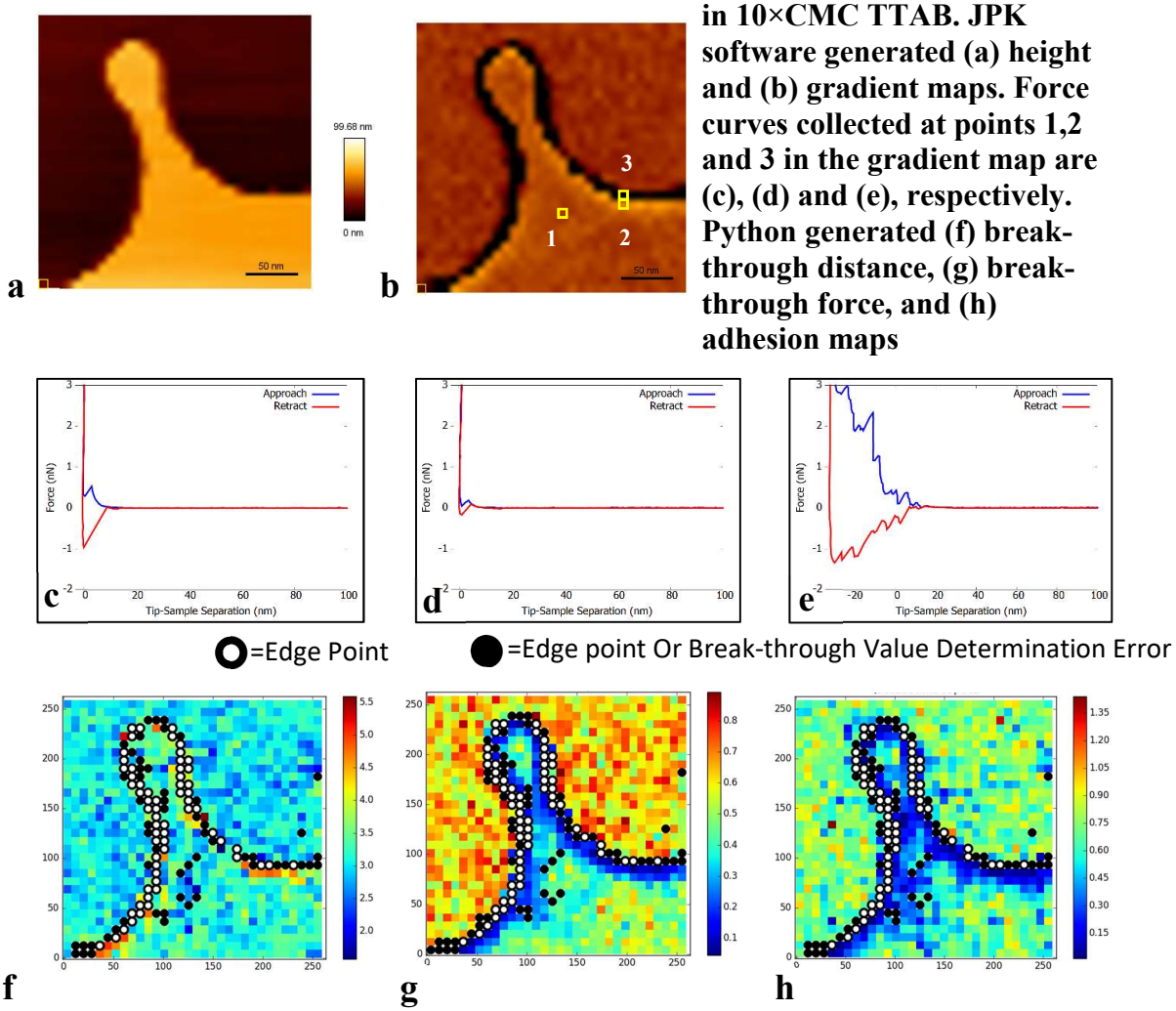

Figure 35. All data is collected in 10×CMC TTAB. JPK software generated (a) height and (b) gradient maps. Force curves collected at points 1,2 and 3 in the gradient map are (c), (d) and (e), respectively. Python generated (f) break-through distance, (g) break-through force, and (h) adhesion maps

The following section will demonstrate the effects of changes in surface topography on adsorbed surfactant using the break-through event characterization method used in the previous sections. The goal is to develop a method for characterizing controlled changes in surface topography in order to better understand how the random changes in surface topography imposed by surface roughness affect adsorbed surfactant.

First, the JPK software was used to create height measured and gradient maps (Figure 35a and Figure 35b) while break-through distance, break-through force and adhesion force maps, Figure 35f, g and h respectively, were created using scripts developed in Python. The force curves in Figure 35c, d and e are for a force curve in the center of the structure (far from an edge), just before the edge and on the edge, respectively. The curve in the center of the nano-structure shows a break-through distance of 3.5 nm, a break-through distance of 0.5 nN and an adhesion force of 1 nN. The force curve just before the edge shows a break-through distance like the unconfined region (3.5 nm) while the break-through and adhesion forces are significantly decreased (0.15 nN and 0.1 nN, respectively). Lastly,

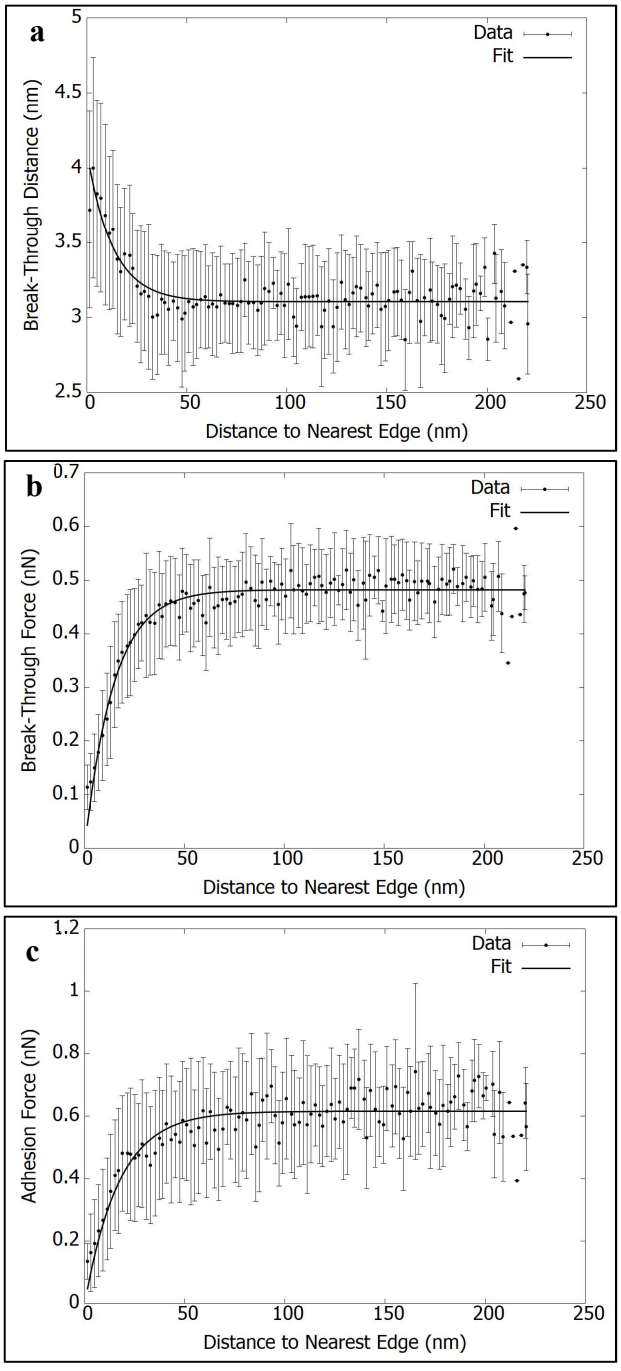

Figure 36. Break-through distance, break-through force and adhesion force values vs. distance from the nearest edge. Solid black line is exponential fitting.

the edge was determined by the erratic nature of the curve and the low gradient value in the map.

The curves were separated into curves on flat spots (colored squares), curves on edges (white circles with black edges), and curves where the break-through values could not be determined, possibly due to an error in the curve caused by debris or proximity to an edge, (black filled in circles). From the height map in Figure 35a, it is possible to distinguish between the upper surface of the nanostructure (light area), which was covered with metal mask during etching, and the lower surface which was etched (dark area). The gradient map (Figure 35b) shows the edges between the upper surface and lower surface but there is otherwise no variation in gradient across the surfaces.

The break-through distance map in Figure 35f shows values between approximately 2.5 nm and 5 nm, which are typical values found on silica in this paper and other literature.[26,73,77] Near the edge the break-through distance values are higher than those farther into the interior of the structure. In the case of the break-through force and adhesion maps, Figure 35g and Figure 35h, respectively, there were also differences between curves near to and far from the edges (points go from yellow and light green to dark blue on the colormap scale), as previously noted.

To more quantitatively investigate the relationship between the break-through event values and the distance to the nearest edge, the distance between a given force curve location and the closest edge was determined. Briefly, the procedure for finding the distance to an edge from a specific map index was to iteratively draw a series of circles on the index, each having a radius of 0.1 nm larger than the last and determining

the minimum radius where at least one edge point was touched by or encompassed in the circle. Break-through event values from these minimum radii were binned into 2 nm increments and the average and standard deviation of this binning are shown in Figure 36. All the data was clearly exponential in shape and therefore each break-through value was fit with the increasing or decreasing form of the exponential equation (given below) where y is the break-through value, x is the distance from the edge, τ is a decay length constant, and C and A are constants.

$$y = Ce^{-x/\tau} + A \qquad \text{Decrease}$$

$$y = C(1 - e^{-x/\tau}) \qquad \text{Increase}$$

The results of the fit for the break-through distance are shown in Figure 36a as the solid black line, where the values of C, τ and A were found to be 0.992±0.0941, 12.90±1.84 and 3.11±0.0126, respectively. Using these values, the maximum break-through distance, which occurs at the edge (x=0), is 4.10±0.0950 nm and the minimum (A) is 3.11±0.0126 nm.

The break-through force and adhesion force values, shown in Figure 36b and Figure 36c, were fit using the increasing form of the exponential equation. The values of C, which in this case is the value of y as x approaches infinity, and τ for break-through force were found to be 0.481 ± 0.00295 and 14.5 ± 0.663, respectively, and for adhesion force 0.615 ± 0.00651 and 17.1 ± 1.23, respectively. It would be interesting to determine if the parameters fitted here were dependent on not just the distance from an edge but also the structure dimensions, i.e. sizes on the order of the decay length distances. However, because there was some difficulty gathering data from the circular/ellipsoidal pillars, which were the smallest structures investigated, we were

unable to make definitive conclusions regarding the fitting parameter values as a function of structure size from the data collected.

However, a second sample was characterized using a second high aspect-ratio probe and the difference between the decay lengths was on the order of ~3-4 nm. As stated by the manufacturer and confirmed by SEM in our laboratory, the radius of curvature of the tip is ~10 nm but because the tip is expected to be irregular (rough) on the nanometer length scale, the actual part of the probe that contacts the surfactant is likely much less than 10 nm. Therefore, although some convolution of the tip with the measured decay lengths is likely occurring, its effects are minimal as evidenced by the relative reproducibility of the decay lengths between the two probes. For further discussion related to the AFM probe as well as the presentation of the data from the second sample refer to Appendix B.

In our experimental work on flat surfaces there was a change in the break-through values only by changing the surfactant concentration below the CMC and in that case the break-through values all increased as the concentration increased as expected.[121] With the invariance of the break-through distance measurement above the CMC to the underlying morphology of the surfactant layer (e.g. monolayer vs. bilayer), we concluded that the break-through distance was not a reliable measure of the true surfactant layer thickness but instead represented the thickness of a hemifused bilayer. Here, the break-through distance increase and decrease of the break-through force and adhesion force indicates a shift to an extended, less-dense hemifused layer with decreasing distance from the edges of nano-pillars.

In the previously mentioned molecular dynamic simulations of Suttipong, surfactant was shown to both form an aggregate that "turns the corner" of a step as well as forms only a single, slightly flat layer on the side of the step leaving the upper surface bare, depending on the height of the step.[50] The conclusion for both arrangements was that there is an energetic penalty to be paid in order to bend the surfactant layer around the edge, a conclusion also reached by Liu et al., Fragneto et al., and Macakova et al. using rough surface experiments.[14,17,28]

Qualitatively, our results are consistent with the former arrangement in Suttipong's simulations; a less dense and stretched surfactant layer was formed on the corner of a step, rather than a layer which is less extended near the edge. However, quantitatively our results are quite different than simulations because the effects extend over much larger distances as indicated by the decay length τ. From the FFT of the soft contact image of TTAB on silica the repeat distance representing the worm-like micelle diameters was found to be 6.62 ± 0.699 nm, which is similar to the values for TTAB on quartz found by Berr.[45] Comparing our FFT dimensions with the decay length from the fitting means that the edge effects extend for 2-3 micelle diameters, much farther than the values suggested in simulations.

This work also shows that the type of confinement matters. Specifically, large changes in adhesion force for the trenches are much larger than the ~25% drop that would be expected based on pillar results. However, as noted earlier, with trenches collecting data at different distances from the wall is not possible; for the 50 nm trench we are mapping only the center which is ~25 nm from each wall.

Chapter 4: Conclusions and Recommendations

Firstly, the gravimetric data presented here agreed with our hypothesis that increasing surface roughness would lead to a decrease in the amount of surfactant that adsorbed. In terms of surfactant morphology, the force mapping characterization also agreed with our hypothesis, which stated that the controlled lateral confinement would affect the adsorbed surfactant layer in thickness. However, our investigation was unable to reveal any changes in the surfactant aggregate shape (e.g. transitions from cylindrical to spherical).

4.1-Quartz Crystal Microbalance with Dissipation

Surfactant adsorption increased with an increase in bulk concentration below the critical micelle concentration (CMC) on both smooth and rough surfaces. At the CMC, on the smooth surface peaks in mass absorbed were found for all temperatures investigated, while on the rough surface a peak was found only at 50°C. The cause of peaks in mass adsorbed is the adsorption of surface-active impurities below the CMC, which we previously found to be much more significant.[10] However, here the peaks were almost eliminated due to helium sparging removing the apparently volatile impurities. To our knowledge, this work represents the first-time surfactant adsorption was studied using QCM at different temperatures, and we found that for this surfactant an increase in temperature caused a reduction in the final equilibrium adsorbed amount on both smooth and rough surfaces. As has been found previously, a reduction in amount adsorbed was observed due to roughness.[10,17]

Time dependent experiments revealed that at short times after a surface is exposed to surfactant concentrations far below the CMC there were 3 regions of adsorption. In the first region adsorption was diffusion controlled and occurred as the concentration is transitioning from zero (pure water) to 0.1×CMC within the measurement cell. Adsorption in the second region was enthalpically controlled, as the mechanism is single surfactant molecule adsorption via electrostatic interactions. The third region showed slow adsorption to a plateau representing the maximum adsorbed amount under the conditions far below surface saturation. The effect of increasing temperature and roughness was indistinguishable in the first and second regions of adsorption, while both reduced adsorption in the third region. To our knowledge, this kinetic behavior for temperature has never been published previously, while the roughness result is consistent with the room temperature result published previously by our group.[10]

At higher concentrations there were five observable regions, supporting three adsorption mechanisms. In the first and second regions adsorption occurred via a diffusion-controlled mechanism. The third region was the transition to an entropically controlled cooperative fourth region, which was then followed by the fifth region, where surface rearrangement occurred. This interpretation has been presented previously.[1,5] However, the interesting contribution made by this work is using the time based regional analysis of a single concentration increment at multiple temperatures. This analysis technique led to the unique conclusion that the decrease in mass adsorbed above the CMC with an increase in temperature was attributable to less adsorption in the cooperative fourth region.

4.2-AFM Force Curve Characterization of Adsorbed Surfactant on Flat Surfaces

Force mapping between two negatively charged silicon AFM tips verified the presence of a cationic surfactant layer on an AFM tip using a set-up which did not use a flat surface. Results from force mapping with a colloidal probe and a probe with a different force constant, respectively, demonstrated that the probe geometry and force constant influenced the break-through force and adhesion force but not break-through distance. Very slight differences, such as tip cleaning between trials, can alter force data values.

Gradient mapping was performed on flat HOPG, silica and silanated silica surfaces and the data showed patches of adsorbed surfactant below the CMC. While the results are consistent with others available in the literature, this is the first time AFM force curves with mapping are used to observe adsorbed surfactants at different times, which in turn gives information about the spatial nature of adsorption. Evidence of changing adsorption density with time is reported. Even at long times, where adsorption density did not change, spatial distribution of adsorbed surfactant patches continued to shift shape/position. With increasing concentration below the CMC, the break-through distance and break-through force increased while the adhesion force decreased.

Break-through force was maximum at the CMC, which was attributed to the well-known impurity effect found in some surface tension plots although further studies would be needed to confirm this conclusion. Very surprisingly, above the CMC the break-through distance did not depend on whether the surface was hydrophilic or hydrophobic. A qualitative phenomenological theory was developed analogous to a theory previously developed to explain surface force apparatus results from two

hydrophilic surfaces. Based on our interpretation, break-through events can be interpreted as a measure of the coverage or stability of the adsorbed layer although the quantitative values will depend on probe tip characteristics and the applied force. Further, the break-through distance does not necessarily represent the thickness of an isolated adsorbed bilayer due to hemifusion. In the case of a bilayer on a charged flat surface and a similarly charged AFM tip with an oppositely charged surfactant, the break-through distance corresponds to a bilayer but in the case of an uncharged flat surface with a monolayer covering of surfactant the break-through distance is not a monolayer.

4.3-Investigating the Effects of Lateral Confinement on Surfactant Adsorption

The effects of lateral confinement on adsorbed surfactant were investigated using AFM force mapping at the center of nano-scale trenches and on the confined upper surfaces of nano-scale pillar structures. With trenches, the cationic surfactant TTAB showed substantial reductions in break-through force and adhesion force with confinement while the cationic surfactant CPC showed a slight increase in these two forces with confinement indicating that the effects of confinement can vary depending on the surfactant. The break-through distance was not affected by any changes in confinement dimension but was smaller on polymer vs. silica, indicating the break-through distance was affected by surface chemistry but not confinement.

Pillar nanostructures revealed the interesting result that with increasing distance from the edge of the nanostructure the break-through distance decreased while the break-through force and adhesion force increased. In all cases the data was well-described with a single exponential model, with decay lengths (τ) varying from 12.9-

17.1 nm. These distances are much larger than expected, given the characteristic 2-3 nm length of a typical surfactant molecule, and may suggest why no strong confinement effects were observed with trenches (distance between wall and surfactant ~25 nm minimum). Trends observed on the pillars indicate that an edge induces an extension of the surfactant layer due to the micelles having to form at the corner between the upper and side surfaces of the nanostructure. A decrease in break-through force and adhesion force close to the edge indicates that this extension is coupled with a reduction in layer density, a conclusion that agrees well with molecular dynamic simulations.

The work presented here, to our knowledge, is the first quantitative evidence of the effect of edges on an adsorbed surfactant layer and confirms that edges can affect adsorbed surfactant for tens of nanometers, or several micelle diameters, from the edge itself. This supports the theory that roughness leads to an extended, more poorly packed surfactant layer as the surfactant attempts to traverse the "peaks" which make up the rough surface and in the most severe case of a topography change, surfactant adsorption will be reduced when that change occurs within a distance of ~50 nm.

Taken from a simulation perspective, this work indicates that the molecular dynamics modelling qualitatively was correct, but quantitatively the predictions grossly underpredicted the length scale while from an applications perspective, roughening a surface is a way to reduce adsorption. Continued development of the methods and analyses developed here could potentially be used to predict surfactant layer properties on surfaces of different roughness if the scale of the features induced by the roughness are known.

Recommendations

These recommendations seek to inform about possible future experiments that could be performed using the methods implemented as part of this work and further the understanding of surfactant adsorption on rough surfaces and surfaces of different surface chemistry.

1. The first recommended study would be to examine the break-through distance using a negatively charged surfactant, a negatively charged surface and a positively charged AFM probe. If there is a break-through event, then the layer on the tip is the most likely source of the stable layer and the value of the break-through distance will further investigate the hypothesis of layer dependent hemifusion.
2. Because the force values depend on tip characteristics, force values could not be compared between different surfaces. A simple experiment that would help further elucidate on the matter of random roughness would be to use multiple different surfaces in the same surfactant solution dish using the same probe and see how the roughness and surface chemistry affects the break-through forces. For example, placing a gold surface, silica surface, and etched silica surface (to vary the roughness) in the same dish filled with surfactant solution and performing a force map on all three. This would allow for the same solution conditions and probe, to remove the effects of tip cleaning, while varying the sample roughness for comparison.
3. Next, study break-through events collected with a chemically modified tip, then a chemically modified surface, then both chemically modified. The work of Pera et al. showed that when various combinations of chemically modified tip and/or samples

were used the force curves displayed corresponding changes in the number of break-through events.[84] Using force mapping, a much larger data set could be collected and compared using the automated method in the force mapping of flat surfaces work. Comparison of the break-through distances of the individual break-through events would be very interesting in the context of compression and the hypothesis of layer dependent hemifusion.

4. The topic of surfactant on the AFM tip could also be investigated using neutron scattering to confirm surfactant orientation and organization. In principle, one could contrast match out the tip-surfactant solution contrast. The examination of surfactant adsorbed to the surface of a carbon nanotube has been performed and demonstrated experimentally the effects of lateral confinement on a curved surface. Examining the surfactant adsorbed on an AFM tip with neutron scattering would allow the study of the orientation and organization of the surfactant. Whether enough signal could be obtained with the very small beam required is very unlikely however.

5. Moving towards patterned surface experiments, an extremely interesting experiment would be to investigate how surfactant adsorbs to hydrophobically patterned surfaces. Nanopatterning has been accomplished using OTS on a silica surface and has been shown to have little effect on the surface topography (i.e. a flat surface is obtained).[122] This patterning would be very interesting with both soft contact imaging and force mapping, especially the transition region from hydrophobic to hydrophilic surface areas. Soft contact imaging would potentially demonstrate differences in morphology while force mapping would provide changes in layer packing, layer

thickness/hemifusion occurrence, and the distance over which the change affects the surfactant layers.

6. Another avenue that should be pursued is the “half-distance” found on the PMMA surface compared to other surfaces. In the beginning when the effects of layer dependent hemifusion were not known it was expected that a break-through distance on a hydrophobic surface would be half that on a hydrophilic surface. However, that was not found to be the case. Therefore, it is especially interesting that out of all the flat surfaces studied in this work, PMMA was the only one which should a distance roughly half that found on other surfaces.

The proposed experiment would essentially involve covering a silica colloidal sphere in PMMA and then performing a force curve against a flat PMMA covered surface and a plain silica surface, respectively. If the PMMA covered sphere and surface have no surfactant adsorbed, then likely the force curves will have a snap to contact instead of a repulsive force. Conversely, if there is surfactant adsorbed then there should be a repulsive force. However, it would be difficult to say whether the repulsive force was generated by surfactant lying flat or the presence of an electrical double layer present due to adsorption of counter-ions. Either way, it would be a first step in explaining if the half-distance on the polymer was caused by surfactant on the tip or a variation of the surfactant layer on the PMMA surface.

7. Lastly, the trench experiments could be repeated using trenches not made of polymer; the use of the polymer was both beneficial and detrimental. The benefits were that the trench walls were a different material with a different surface chemistry than the trench floor. This allowed for the testing of two surface chemistries under the same

conditions. In addition, the polymer was also softer than the silica, thus tip contact with the walls was less abrasive and easier on the tip retaining its high aspect ratio nature longer. However, the use of polymer was also detrimental because as the polymer began to swell, it provided a source of contamination as well as an uncontrolled source of trench width variability.

In a future experiment the trenches could be made completely out of silica by using electron beam lithography in the same manner used to create the polymer trenches in the first place. E-beam lithography would be used to create the mask in the PMMA and then reactive ion etching would be used to etch the exposed silica floor. Using the Teflon coated sample holder should ensure that the effects of undercutting are minimized. The vertical sides of the pillars have already demonstrated the effectiveness of this fabrication method. Then, removal of the polymer would be accomplished using the PG remover, similar to the metal lift-off experiments.

This method would undoubtedly alter the roughness of the trench floor, as the etched silica used in the pillar experiments was rougher than unetched. Reducing the roughness however could be done by growing an oxide layer on the etched surface. Also, it would be simple to clear a larger portion of the polymer on the same sample or use the wheel centers as the unconfined surfaces. These areas would theoretically have the same history and roughness as the floor of the trenches and provide a good surface for comparison to the confined trench floors.

References

(1) Paria, S.; Khilar, K. C. A review on experimental studies of surfactant adsorption at the hydrophilic solid-water interface. *Adv. Colloid Interface Sci.* **2004**, *110*, 75-95.

(2) Claesson, P. M.; Kjellin, M.; Rojas, O. J.; Stubenrauch, C. Short-range interactions between non-ionic surfactant layers. *PCCP* **2006**, *8*, 5501-5514.

(3)Romsted, L. S. *Surfactant Science and Technology: Retrospects and Prospects*; Taylor & Francis, 2014.

(4)Berg, J. C. *An Introduction to Interfaces & Colloids: The Bridge to Nanoscience*; World Scientific, 2010.

(5) Atkin, R.; Craig, V. S. J.; Wanless, E. J.; Biggs, S. Mechanism of cationic surfactant adsorption at the solid–aqueous interface. *Adv. Colloid Interface Sci.* **2003**, *103*, 219-304.

(6) Nagarajan, R. Molecular Packing Parameter and Surfactant Self-Assembly: The Neglected Role of the Surfactant Tail. *Langmuir* **2002**, *18*, 31-38.

(7) Tiberg, F.; Brinck, J.; Grant, L. Adsorption and surface-induced self-assembly of surfactants at the solid–aqueous interface. *Current Opinion in Colloid & Interface Science* **1999**, *4*, 411-419.

(8) Salari, Z.; Ahmadi, M. A.; Kharrat, R.; Shahri, A. A. Experimental Studies of Cationic Surfactant Adsorption onto Carbonate Rocks. *Australian Journal of Applied Sciences* **2011**, *5*, 808-813.

(9) Dixit, S. G.; Vanjara, A. K.; Nagarkar, J.; Nikoorazm, M.; Desai, T. Co-adsorption of quaternary ammonium compounds—nonionic surfactants on solid–liquid interface. *Colloids and Surfaces A: Physicochemical and Engineering Aspects* **2002**, *205*, 39-46.

(10) Wu, S. Q.; Shi, L.; Garfield, L. B.; Tabor, R. F.; Striolo, A.; Grady, B. P. Influence of Surface Roughness on Cetyltrimethylammonium Bromide Adsorption from Aqueous Solution. *Langmuir* **2011**, *27*, 6091-6098.

(11) Marsalek, R.; Pospisil, J.; Taraba, B. The influence of temperature on the adsorption of CTAB on coals. *Colloids and Surfaces A: Physicochemical and Engineering Aspects* **2011**, *383*, 80-85.

(12) Alkan, M.; Karadaş, M.; Doğan, M.; Demirbaş, Ö. Adsorption of CTAB onto perlite samples from aqueous solutions. *J. Colloid Interface Sci.* **2005**, *291*, 309-318.

(13) Gutig, C.; Grady, B. P.; Striolo, A. Experimental studies on the adsorption of two surfactants on solid-aqueous interfaces: Adsorption isotherms and kinetics. *Langmuir* **2008**, *24*, 13814-13814.

(14) Macakova, L.; Blomberg, E.; Claesson, P. M. Effect of adsorbed layer surface roughness on the QCM-D response: Focus on trapped water. *Langmuir* **2007**, *23*, 12436-12444.

(15) Bordes, R.; Hook, F. Separation of Bulk Effects and Bound Mass during Adsorption of Surfactants Probed by Quartz Crystal Microbalance with Dissipation: Insight into Data Interpretation. *Anal. Chem.* **2010**, *82*, 9116-9121.

(16) Caruso, F.; Serizawa, T.; Furlong, D. N.; Okahata, Y. Quartz-Crystal Microbalance and Surface-Plasmon Resonance Study of Surfactant Adsorption onto Gold and Chromium-Oxide Surfaces. *Langmuir* **1995**, *11*, 1546-1552.

(17) Fragneto, G.; Thomas, R. K.; Rennie, A. R.; Penfold, J. Neutron reflection from hexadecyltrimethylammonium bromide adsorbed on smooth and rough silicon surfaces. *Langmuir* **1996**, *12*, 6036-6043.

(18) Tiberg, F. Physical characterization of non-ionic surfactant layers adsorbed at hydrophilic and hydrophobic solid surfaces by time-resolved ellipsometry. *J. Chem. Soc., Faraday Trans.* **1996**, *92*, 531-538.

(19) Berry, J. D.; Neeson, M. J.; Dagastine, R. R.; Chan, D. Y. C.; Tabor, R. F. Measurement of surface and interfacial tension using pendant drop tensiometry. *J. Colloid Interface Sci.* **2015**, *454*, 226-237.

(20) Yoon, R.-H.; Yordan, J. L. Zeta-potential measurements on microbubbles generated using various surfactants. *J. Colloid Interface Sci.* **1986**, *113*, 430-438.

(21) Sun, Z.; Nicolosi, V.; Rickard, D.; Bergin, S. D.; Aherne, D.; Coleman, J. N. Quantitative Evaluation of Surfactant-stabilized Single-walled Carbon Nanotubes: Dispersion Quality and Its Correlation with Zeta Potential. *J. Phys. Chem. C* **2008**, *112*, 10692-10699.

(22) Donaldson, S. H.; Lee, C. T.; Chmelka, B. F.; Israelachvili, J. N. General hydrophobic interaction potential for surfactant/lipid bilayers from direct force measurements between light-modulated bilayers. *Proc. Natl. Acad. Sci.* **2011**, *108*, 15699-15704.

(23) Manne, S.; Cleveland, J. P.; Gaub, H. E.; Stucky, G. D.; Hansma, P. K. Direct Visualization of Surfactant Hemimicelles by Force Microscopy of the Electrical Double Layer. *Langmuir* **1994**, *10*, 4409-4413.

(24) Furst, E. M.; Pagac, E. S.; Tilton, R. D. Coadsorption of Polylysine and the Cationic Surfactant Cetyltrimethylammonium Bromide on Silica. *Industrial & Engineering Chemistry Research* **1996**, *35*, 1566-1574.

(25) Wanless, E. J.; Ducker, W. A. Organization of Sodium Dodecyl Sulfate at the Graphite−Solution Interface. *J. Phys. Chem.* **1996**, *100*, 3207-3214.

(26) Velegol, S. B.; Fleming, B. D.; Biggs, S.; Wanless, E. J.; Tilton, R. D. Counterion Effects on Hexadecyltrimethylammonium Surfactant Adsorption and Self-Assembly on Silica. *Langmuir* **2000**, *16*, 2548-2556.

(27) Wanless, E. J.; Davey, T. W.; Ducker, W. A. Surface Aggregate Phase Transition. *Langmuir* **1997**, *13*, 4223-4228.

(28) Liu, J.-F.; Ducker, W. A. Surface-Induced Phase Behavior of Alkyltrimethylammonium Bromide Surfactants Adsorbed to Mica, Silica, and Graphite. *J. Phys. Chem. B* **1999**, *103*, 8558-8567.

(29) Subramanian, V.; Ducker, W. A. Counterion Effects on Adsorbed Micellar Shape: Experimental Study of the Role of Polarizability and Charge. *Langmuir* **2000**, *16*, 4447-4454.

(30) Panya, P.; Arquero, O.-a.; Franks, G. V.; Wanless, E. J. Dispersion stability of a ceramic glaze achieved through ionic surfactant adsorption. *J. Colloid Interface Sci.* **2004**, *279*, 23-35.

(31) Partyka, S.; Lindheimer, M.; Faucompre, B. Aggregate Formation at the Solid-Liquid Interface-The Calorimetric Evidence. *Colloids and Surfaces a-Physicochemical and Engineering Aspects* **1993**, *76*, 267-281.

(32) Seidel, J.; Wittrock, C.; Kohler, H. H. Adsorption enthalpies of cationic and nonionic surfactants on silica gel. 2. Microcalorimetric determination of adsorption enthalpies. *Langmuir* **1996**, *12*, 5557-5562.

(33) Somasundaran, P.; Krishnakumar, S. Adsorption of surfactants and polymers at the solid-liquid interface. *Colloids and Surfaces a-Physicochemical and Engineering Aspects* **1997**, *123*, 491-513.

(34) Gürses, A.; Karaca, S.; Aksakal, F.; Açikyildiz, M. Monomer and micellar adsorptions of CTAB onto the clay/water interface. *Desalination* **2010**, *264*, 165-172.

(35) Meader, A. L.; Fries, B. A. Adsorption in the Detergent Process. *Ind. Eng. Chem.* **1952**, *44*, 1636-1648.

(36) Fava, A.; Eyring, H. Equilibrium and Kinetics of Detergent Adsorption-A Generalized Equilibration Theory. *J. Phys. Chem.* **1956**, *60*, 890-898.

(37) Pavan, P. C.; Crepaldi, E. L.; Gomes, G. D.; Valim, J. B. Adsorption of sodium dodecylsulfate on a hydrotalcite-like compound. Effect of temperature, pH and ionic strength. *Colloids and Surfaces a-Physicochemical and Engineering Aspects* **1999**, *154*, 399-410.

(38)Rosen, M. J. In *Surfactants and Interfacial Phenomena*; Wiley and Sons, Inc.: Hoboken, New Jersey, 2004.

(39)Myers, D. In *Surfactant Science and Technology*; John Wiley & Sons, Inc: Hoboken, New Jersey, 2006.

(40) Biswas, S. C.; Chattoraj, D. K. Kinetics of Adsorption of Cationic Surfactants at Silica-Water Interface. *J. Colloid Interface Sci.* **1998**, *205*, 12-20.

(41)Ruiz, C. C.; Molina-Bolivar, J. A. In *Sugar-Based Surfactants: Fundamentals and Applications*; Taylor & Francis: Boca Raton, Fl, 2010.

(42) Manojlovic, J. Ž. The Krafft Temperature of Surfactant Solutions. *Thermal Science* **2012**, *16*, S631-S640.

(43) Vautier-Giongo, C.; Bales, B. L. Estimate of the Ionization Degree of Ionic Micelles Based on Krafft Temperature Measurements. *J. Phys. Chem. B* **2003**, *107*, 5398-5403.

(44) Beyer, K.; Leine, D.; Blume, A. The demicellization of alkyltrimethylammonium bromides in 0.1M sodium chloride solution studied by isothermal titration calorimetry. *Colloids and Surfaces B: Biointerfaces* **2006**, *49*, 31-39.

(45) Schulz, J. C.; Warr, G. G. Adsorbed Layer Structure of Cationic and Anionic Surfactants on Mineral Oxide Surfaces. *Langmuir* **2002**, *18*, 3191-3197.

(46) Schniepp, H. C.; Shum, H. C.; Saville, D. A.; Aksay, I. A. Surfactant Aggregates at Rough Solid−Liquid Interfaces. *J. Phys. Chem. B* **2007**, *111*, 8708-8712.

(47) Tummala, N. R.; Striolo, A. SDS Surfactants on Carbon Nanotubes: Aggregate Morphology. *ACS Nano* **2009**, *3*, 595-602.

(48) Tummala, N. R.; Grady, B. P.; Striolo, A. Lateral confinement effects on the structural properties of surfactant aggregates: SDS on graphene. *PCCP* **2010**, *12*, 13137-13143.

(49) Suttipong, M.; Grady, B. P.; Striolo, A. Surfactant Aggregates Templated by Lateral Confinement. *J. Phys. Chem. B* **2015**, *119*, 5467-5474.

(50) Suttipong, M.; Grady, B. P.; Striolo, A. Surfactants adsorption on crossing stripes and steps. *Soft Matter* **2017**, *13*, 862-874.

(51) Marquez, M.; Patel, K.; Carswell, A. D. W.; Schmidtke, D. W.; Grady, B. P. Synthesis of Nanometer-Scale Polymeric Structures on Surfaces from Template Assisted Admicellar Polymerization: A Comparative Study with Protein Adsorption. *Langmuir* **2006**, *22*, 8010-8016.

(52) Kou, J.; Tao, D.; Xu, G. A study of adsorption of dodecylamine on quartz surface using quartz crystal microbalance with dissipation. *Colloids and Surfaces A: Physicochemical and Engineering Aspects* **2010**, *368*, 75-83.

(53) Smith, T. The hydrophilic nature of a clean gold surface. *J. Colloid Interface Sci.* **1980**, *75*, 51-55.

(54) Wall, J. F.; Zukoski, C. F. Alcohol-Induced Structural Transformations of Surfactant Aggregates. *Langmuir* **1999**, *15*, 7432-7437.

(55) Jaschke, M.; Butt, H. J.; Gaub, H. E.; Manne, S. Surfactant Aggregates at a Metal Surface. *Langmuir* **1997**, *13*, 1381-1384.

(56) Saphanuchart, W.; Saiwan, C.; O'Haver, J. H. Effect of adsolubilized solutes on 2-D structure of cationic admicelles. *Colloids and Surfaces A: Physicochemical and Engineering Aspects* **2007**, *307*, 71-76.

(57) Shi, L.; Ghezzi, M.; Caminati, G.; Lo Nostro, P.; Grady, B. P.; Striolo, A. Adsorption Isotherms of Aqueous C12E6 and Cetyltrimethylammonium Bromide Surfactants on Solid Surfaces in the Presence of Low Molecular Weight Coadsorbents. *Langmuir* **2009**, *25*, 5536-5544.

(58) Knag, M.; Sjöblom, J.; Gulbrandsen, E. The Effect of Straight Chain Alcohols and Ethylene Glycol on the Adsorption of CTAB on Gold. *J. Dispersion Sci. Technol.* **2005**, *26*, 207-215.

(59) Mivehi, L.; Bordes, R.; Holmberg, K. Adsorption of Cationic Gemini Surfactants at Solid Surfaces Studied by QCM-D and SPR: Effect of the Rigidity of the Spacer. *Langmuir* **2011**, *27*, 7549-7557.

(60)Hermansson, K.; Lindberg, U.; Hok, B.; Palmskog, G. In *Solid-State Sensors and Actuators, 1991. Digest of Technical Papers, , 1991 International Conference onTransducers*, 1991, pp 193-196.

(61)Cademartiri, L.; Ozin, G. A. In *Concepts of Nanochemistry*; Wiley-VCH GmbH & Co., 2009.

(62) Bordes, R.; Tropsch, J.; Holmberg, K. Adsorption of Dianionic Surfactants Based on Amino Acids at Different Surfaces Studied by QCM-D and SPR. *Langmuir* **2010**, *26*, 10935-10942.

(63) Howard, S. C.; Craig, V. S. J. Very slow surfactant adsorption at the solid-liquid interface is due to long lived surface aggregates. *Soft Matter* **2009**, *5*, 3061-3069.

(64) Stålgren, J. J.; Eriksson, J.; Boschkova, K. A Comparative Study of Surfactant Adsorption on Model Surfaces Using the Quartz Crystal Microbalance and the Ellipsometer. *J. Colloid Interface Sci.* **2002**, *253*, 190-195.

(65) Sakai, K.; Matsuhashi, K.; Honya, A.; Oguchi, T.; Sakai, H.; Abe, M. Adsorption Characteristics of Monomeric/Gemini Surfactant Mixtures at the Silica/Aqueous Solution Interface. *Langmuir* **2010**, *26*, 17119-17125.

(66) Somasundaran, P.; Huang, L. Adsorption/aggregation of surfactants and their mixtures at solid–liquid interfaces. *Adv. Colloid Interface Sci.* **2000**, *88*, 179-208.

(67) Lin, D. C.; Dimitriadis, E. K.; Horkay, F. Robust Strategies for Automated AFM Force Curve Analysis—I. Non-adhesive Indentation of Soft, Inhomogeneous Materials. *J. Biomech. Eng.* **2006**, *129*, 430-440.

(68) Saville, D. A.; Chun, J.; Li, J. L.; Schniepp, H. C.; Car, R.; Aksay, I. A. Orientational Order of Molecular Assemblies on Inorganic Crystals. *Phys. Rev. Lett.* **2006**, *96*, 018301.

(69) Wanless, E. J.; Ducker, W. A. Weak Influence of Divalent Ions on Anionic Surfactant Surface-Aggregation. *Langmuir* **1997**, *13*, 1463-1474.

(70) Manne, S.; Gaub, H. E. Molecular-Organization of Surfactants at Solid-Liquid Interfaces. *Science* **1995**, *270*, 1480-1482.

(71) Blom, A.; Warr, G. G.; Wanless, E. J. Morphology Transitions in Nonionic Surfactant Adsorbed Layers near Their Cloud Points. *Langmuir* **2005**, *21*, 11850-11855.

(72) Schniepp, H. C.; Saville, D. A.; Aksay, I. A. Tip-Induced Orientational Order of Surfactant Micelles on Gold. *Langmuir* **2008**, *24*, 626-631.

(73) Liu, J.-F.; Min, G.; Ducker, W. A. AFM Study of Adsorption of Cationic Surfactants and Cationic Polyelectrolytes at the Silica−Water Interface. *Langmuir* **2001**, *17*, 4895-4903.

(74) Künneke, S.; Krüger, D.; Janshoff, A. Scrutiny of the Failure of Lipid Membranes as a Function of Headgroups, Chain Length, and Lamellarity Measured by Scanning Force Microscopy. *Biophys. J.* **2004**, *86*, 1545-1553.

(75) Lima, L. M. C.; Giannotti, M. I.; Redondo-Morata, L.; Vale, M. L. C.; Marques, E. F.; Sanz, F. Morphological and Nanomechanical Behavior of Supported Lipid Bilayers on Addition of Cationic Surfactants. *Langmuir* **2013**, *29*, 9352-9361.

(76) Senden, T. J.; Drummond, C. J.; Kekicheff, P. Atomic Force Microscopy: Imaging with Electrical Double Layer Interactions. *Langmuir* **1994**, *10*, 358-362.

(77) Li, J.; Zhang, C.; Cheng, P.; Chen, X.; Wang, W.; Luo, J. AFM Studies on Liquid Superlubricity between Silica Surfaces Achieved with Surfactant Micelles. *Langmuir* **2016**, *32*, 5593-5599.

(78) Butt, H.-J.; Franz, V. Rupture of molecular thin films observed in atomic force microscopy. I. Theory. *Phys. Rev. E.* **2002**, *66*, 031601.

(79) Micklavzina, B. L.; Zhang, S.; He, H.; Longo, M. L. Nanomechanical Characterization of Micellar Surfactant Films via Atomic Force Microscopy at a Graphite Surface. *Langmuir* **2017**, *33*, 2122-2132.

(80) Li, J. K.; Sullan, R. M. A.; Zou, S. Atomic Force Microscopy Force Mapping in the Study of Supported Lipid Bilayers. *Langmuir* **2011**, *27*, 1308-1313.

(81) Kobayashi, N.; Saitoh, H.; Kawamura, R.; Yoshikawa, H. Y.; Nakabayashi, S. Structural change of nonionic surfactant self-assembling at electrochemically controlled HOPG/electrolyte interface. *J. Electroanal. Chem.* **2017**, *799*, 444-450.

(82) Franz, V.; Loi, S.; Müller, H.; Bamberg, E.; Butt, H.-J. Tip penetration through lipid bilayers in atomic force microscopy. *Colloids and Surfaces B: Biointerfaces* **2002**, *23*, 191-200.

(83) Loi, S.; Sun, G.; Franz, V.; Butt, H. J. Rupture of molecular thin films observed in atomic force microscopy. II. Experiment. *Phys. Rev. E.* **2002**, *66*, 031602.

(84) Pera, I.; Stark, R.; Kappl, M.; Butt, H.-J.; Benfenati, F. Using the Atomic Force Microscope to Study the Interaction between Two Solid Supported Lipid Bilayers and the Influence of Synapsin I. *Biophys. J.* **2004**, *87*, 2446-2455.

(85) Zou, Y.; Jayasuriya, S.; Manke, C. W.; Mao, G. Influence of Nanoscale Surface Roughness on Colloidal Force Measurements. *Langmuir* **2015**, *31*, 10341-10350.

(86) Garcia-Manyes, S.; Redondo-Morata, L.; Oncins, G.; Sanz, F. Nanomechanics of Lipid Bilayers: Heads or Tails? *J. Am. Chem. Soc.* **2010**, *132*, 12874-12886.

(87) Stiernstedt, J.; Fröberg, J. C.; Tiberg, F.; Rutland, M. W. Forces between Silica Surfaces with Adsorbed Cationic Surfactants: Influence of Salt and Added Nonionic Surfactants. *Langmuir* **2005**, *21*, 1875-1883.

(88) Manna, K.; Panda, A. Physicochemical Studies on the Interfacial and Micellization Behavior of CTAB in Aqueous Polyethylene Glycol Media. *Journal of Surfactants and Detergents* **2011**, *14*, 563-576.

(89) Mata, J.; Varade, D.; Bahadur, P. Aggregation behavior of quaternary salt based cationic surfactants. *Thermochim. Acta* **2005**, *428*, 147-155.

(90) Dominguez, A.; Fernandez, A.; Gonzalez, N.; Iglesias, E.; Montenegro, L. Determination of Critical Micelle Concentration of Some Surfactants by Three Techniques. *J. Chem. Educ.* **1997**, *74*, 1227.

(91)Mukerjee, P.; Mysels, K. J. *Critical micelle concentrations of aqueous surfactant systems*; U.S. National Bureau of Standards; for sale by the Supt. of Docs., U.S. Govt. Print. Off., 1971.

(92)In *Q-Sense QSX 301 Product Specificiations Pamphlet*

(93)In *Q-sense Cleaning and Immobilization Protocol*.

(94) Kozbial, A.; Trouba, C.; Liu, H.; Li, L. Characterization of the Intrinsic Water Wettability of Graphite Using Contact Angle Measurements: Effect of Defects on Static and Dynamic Contact Angles. *Langmuir* **2017**, *33*, 959-967.

(95) Vold, R. D.; Sivaramakrishnan, N. H. The Origin of the Maximum in the Adsorption Isotherms of Association Colloids. *J. Phys. Chem.* **1958**, *62*, 984-989.

(96) Sexsmith, F. H.; White Jr, H. J. The absorption of cationic surfactants by cellulosic materials: III. A theoretical model for the absorption process and a discussion of maxima in absorption isotherms for surfactants. *Journal of Colloid Science* **1959**, *14*, 630-639.

(97) Paria, S.; Manohar, C.; Khilar, K. C. Adsorption of anionic and non-ionic surfactants on a cellulosic surface. *Colloids and Surfaces A: Physicochemical and Engineering Aspects* **2005**, *252*, 221-229.

(98) Scamehorn, J. F.; Schechter, R. S.; Wade, W. H. Adsorption of surfactants on mineral oxide surfaces from aqueous solutions: I: Isomerically pure anionic surfactants. *J. Colloid Interface Sci.* **1982**, *85*, 463-478.

(99) Somasundaran, P.; Fuerstenau, D. W. Mechanisms of Alkyl Sulfonate Adsorption at the Alumina-Water Interface. *J. Phys. Chem.* **1966**, *70*, 90-96.

(100) Ning, H.; Kita, R.; Kriegs, H.; Luettmer-Strathmann, J.; Wiegand, S. Thermal Diffusion Behavior of Nonionic Surfactants in Water. *J. Phys. Chem. B* **2006**, *110*, 10746-10756.

(101) Danov, K.; Kralchevsky, P. The standard free energy of surfactant adsorption at air/water and oil/water interfaces: Theoretical vs. empirical approaches. *Colloid J.* **2012**, *74*, 172-185.

(102)Fong, P. A. *Colloid and Surface Research Trends*; Nova Science Publishers, 2007.

(103) Ducker, W. A.; Grant, L. M. Effect of Substrate Hydrophobicity on Surfactant Surface−Aggregate Geometry. *J. Phys. Chem.* **1996**, *100*, 11507-11511.

(104) Butt, H.-J.; Cappella, B.; Kappl, M. Force measurements with the atomic force microscope: Technique, interpretation and applications. *Surf. Sci. Rep.* **2005**, *59*, 1-152.

(105)Biggs, S.; Mulvaney, P. In *Surfactant Adsorption and Surface Solubilization*; American Chemical Society, 1996, pp 255-266.

(106) Podgornik, R.; Parsegian, V. A. Forces between CTAB-Covered Glass Surfaces Interpreted as an Interaction-Driven Surface Instability. *J. Phys. Chem.* **1995**, *99*, 9491-9496.

(107) Helm, C. A.; Israelachvili, J. N.; McGuiggan, P. M. Molecular mechanisms and forces involved in the adhesion and fusion of amphiphilic bilayers. *Science* **1989**, *246*, 919-922.

(108) Subramanian, V.; Ducker, W. Proximal Adsorption of Cationic Surfactant on Silica at Equilibrium. *J. Phys. Chem. B* **2001**, *105*, 1389-1402.

(109) Chun, J.; Li, J.-L.; Car, R.; Aksay, I. A.; Saville, D. A. Anisotropic Adsorption of Molecular Assemblies on Crystalline Surfaces. *J. Phys. Chem. B* **2006**, *110*, 16624-16632.

(110) Warr, G. G. Surfactant adsorbed layer structure at solid/solution interfaces: impact and implications of AFM imaging studies. *Current Opinion in Colloid & Interface Science* **2000**, *5*, 88-94.

(111) Atkin, R.; Craig, V. S. J.; Biggs, S. Adsorption Kinetics and Structural Arrangements of Cationic Surfactants on Silica Surfaces. *Langmuir* **2000**, *16*, 9374-9380.

(112) Pagac, E. S.; Prieve, D. C.; Tilton, R. D. Kinetics and Mechanism of Cationic Surfactant Adsorption and Coadsorption with Cationic Polyelectrolytes at the Silica−Water Interface. *Langmuir* **1998**, *14*, 2333-2342.

(113) Woods, D. A.; Petkov, J.; Bain, C. D. Surfactant Adsorption Kinetics by Total Internal Reflection Raman Spectroscopy. 1. Pure Surfactants on Silica. *J. Phys. Chem. B* **2011**, *115*, 7341-7352.

(114) Howard, S. C.; Craig, V. S. J. Adsorption of the Cationic Surfactant Cetyltrimethylammonium Bromide to Silica in the Presence of Sodium Salicylate: Surface Excess and Kinetics. *Langmuir* **2009**, *25*, 13015-13024.

(115) Lajtar, L.; Narkiewicz-Michalek, J.; Rudzinski, W.; Partyka, S. A New Theoretical Approach to Adsorption of Ionic Surfactants at Water/Oxide Interfaces: Studies of the Mechanism of Cationic Surfactant Adsorption. *Langmuir* **1994**, *10*, 3754-3764.

(116) Rabinovich, Y. I.; Pandey, S.; Shah, D. O.; Moudgil, B. M. Effect of the Chain-Length Compatibility of Surfactants and Mechanical Properties of Mixed Micelles on Surfaces. *Langmuir* **2006**, *22*, 6858-6862.

(117) Lokar, W. J.; Ducker, W. A. Forces between Glass Surfaces in Mixed Cationic−Zwitterionic Surfactant Systems. *Langmuir* **2004**, *20*, 4553-4558.

(118) Rennie, A. R.; Lee, E. M.; Simister, E. A.; Thomas, R. K. Structure of a cationic surfactant layer at the silica-water interface. *Langmuir* **1990**, *6*, 1031-1034.

(119) Király, Z.; Findenegg, G. H. Pulsed-Flow Microcalorimetric Study of the Template-Monolayer Region of Nonionic Surfactants Adsorbed at the Graphite/Water Interface. *Langmuir* **2005**, *21*, 5047-5054.

(120) Hu, K.; Bard, A. J. Characterization of Adsorption of Sodium Dodecyl Sulfate on Charge-Regulated Substrates by Atomic Force Microscopy Force Measurements. *Langmuir* **1997**, *13*, 5418-5425.

(121) Hamon, J. J.; Tabor, R. F.; Striolo, A.; Grady, B. P. Atomic Force Microscopy Force Mapping Analysis of an Adsorbed Surfactant above and below the Critical Micelle Concentration. *Langmuir* **2018**, *34*, 7223-7239.

(122) Checco, A.; Gang, O.; Ocko, B. M. Liquid Nanostripes. *Phys. Rev. Lett.* **2006**, *96*, 056104.

(123) Taylor, Z. R.; Patel, K.; Spain, T. G.; Keay, J. C.; Jernigen, J. D.; Sanchez, E. S.; Grady, B. P.; Johnson, M. B.; Schmidtke, D. W. Fabrication of Protein Dot Arrays via Particle Lithography. *Langmuir* **2009**, *25*, 10932-10938.

(124) Kawata, H.; Yasuda, M.; Hirai, Y. Fabrication of Si mold with smooth side wall by new plasma etching process. *Microelectron. Eng.* **2007**, *84*, 1140-1143.

(125) Kosiorek, A.; Kandulski, W.; Glaczynska, H.; Giersig, M. Fabrication of nanoscale rings, dots, and rods by combining shadow nanosphere lithography and annealed polystyrene nanosphere masks. *Small* **2005**, *1*, 439-444.

(126) Cui, A.; Li, W.; Luo, Q.; Liu, Z.; Gu, C. Controllable three dimensional deformation of platinum nanopillars by focused-ion-beam irradiation. *Microelectron. Eng.* **2012**, *98*, 409-413.

(127) Cui, A.; Li, W.; Shen, T. H.; Yao, Y.; Fenton, J. C.; Peng, Y.; Liu, Z.; Zhang, J.; Gu, C. Thermally induced shape modification of free-standing nanostructures for advanced functionalities. *Scientific reports* **2013**, *3*, 2429.

(128)In *Q-Sense E4 Operator Manual*.

(129)Rodahl, M.; Kasemo, B. *A simple setup to simultaneously measure the resonant frequency and the absolute dissipation factor of a quartz crystal microbalance*, 1996; Vol. 67, p 3238-3241.

(130) Dunér, G.; Thormann, E.; Dėdinaitė, A. Quartz Crystal Microbalance with Dissipation (QCM-D) studies of the viscoelastic response from a continuously growing grafted polyelectrolyte layer. *J. Colloid Interface Sci.* **2013**, *408*, 229-234.

(131) Lennard-Jones, J. E. On the determination of molecular fields. —II. From the equation of state of a gas. *Proceedings of the Royal Society of London. Series A* **1924**, *106*, 463-477.

(132)Dobryden, I. *Scanning probe microscopy studies of interaction forces between particles: emphasis on magnetite, bentonite and silica*, 2014.

(133) Haugstad, G.; Jones, R. R. Mechanisms of dynamic force microscopy on polyvinyl alcohol: region-specific non-contact and intermittent contact regimes. *Ultramicroscopy* **1999**, *76*, 77-86.

Appendix A: List of Equations

Appendix B: Pillar Fabrication Methods

B.1-Polystyrene Latex Microsphere Preparation

Polystyrene latex microspheres with diameter 200 nm were received as a 2.5wt% dispersion in water from Alfa Aesar. Aliquots of the solution were rinsed by first centrifuging 3 mL (2 Eppendorf tubes each with 1.5 mL of the suspension) at 20,817G for 20 min in an Eppendorf 5430 centrifuge to create a pellet. Then 1.5 mL of the supernatant was removed from each tube and replaced with the same volume of Milli-Q H_2O. The microspheres were dispersed via vortex shaker and the centrifuging and supernatant replacement process was repeated once more. The microsphere dispersion was then diluted to 1.5wt% and stored in a sealed container to prevent evaporation.

B.2-PDMS Mask Fabrication and Sphere Deposition

The method for depositing the spheres on the surface was adapted from the work of Taylor et al.[123] Poly dimethyl siloxane (PDMS) was prepared in a plastic dish using a 10:1 weight ratio of Dow Corning silicone:curing agent which was cured in an oven overnight. Thinner layers were preferred over thicker layers and showed no noticeable difference in masking efficiency. The cured PDMS layer was removed from the dish by razor blade and cut into 1 cm×1 cm squares before a 3 mm hole was cut into each square using a leather punch. Prior to each use, the PDMS mask was rinsed with methanol and water and then set onto the surface of a silica sample (which had been stored for a minimum of 24 hours after being cleaned). Care was taken not to let any liquid leak into the center of the mask and contact the area not covered by the mask. The masked sample was then placed in the Harrick Plasma Cleaner (PDC-32G) for 30 seconds on the 'low' setting before being removed. The area in the hole of the PDMS mask was exposed to the plasma and became hydrophilic while the rest of the sample underneath the PDMS remained hydrophobic. Then the PDMS mask was removed from the silica surface and 3 μL of the microsphere solution was applied via pipette to the hydrophilic area on the silica surface, confined to this area via the surrounding hydrophobic area. The process was repeated for each sample in a set and the samples were placed in a closed container and allowed to dry overnight at approximately 4°C before being removed and stored.

B.3-Nanosphere Heating, Metal Evaporation and Nanosphere Removal

Following the drying process, samples were stored for 48 hours at room temperature to allow further evaporation before heating in a vacuum oven at 112°C for

3 hours. This heating step caused the shapes of the interstitial apertures between the microspheres to go from triangular to circular and decreased the aperture diameter. The samples were removed from the oven once their time elapsed and were allowed to cool to room temperature.

Thermal evaporation into the interstitial spaces was performed as follows. A standard chrome coated tungsten rod (R.D. Mathis *Vacuum* Evaporation Sources) was installed as the metal source in the evaporator and the apparatus bell jar was put in place. The chamber was pumped down for 24 hours before performing a 20 minute degas to clean the source and further decrease the pressure before bringing the source to operating current to begin the evaporation. During evaporation, the metal thickness on the sample was monitored using a quartz crystal microbalance (QCM) crystal inside the chamber and for an evaporation time of 40 seconds the metal thickness was ~20 nm. The samples were removed from the evaporator and placed in toluene and sonicated for 1 hour to remove the nanosphere mask, leaving behind a metal masked silica surface.

B.4-Teflon® Covered Aluminum RIE Sample Holder Fabrication

The Teflon® covered RIE sample holder was proposed and developed for reactive ion etching (RIE) by Kawata et al.[124] Our version of their sample holder was 104 mm×104 mm and 6.35 mm thick. A square recess was milled in the center of the holder to be 2 mm deep and 15 mm x 15 mm. The recess was made using a 1/8”

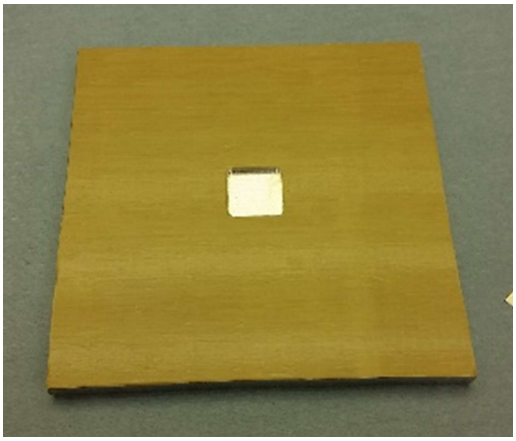

Figure 37. Teflon tape covered aluminum plate with glass stub in center hole.

drill bit. Plate glass 3 mm thick was cut to 15 mm x 15 mm with a glass cutting tool. The corners were rounded to the same radius of curvature as the recess in the aluminum plate (formed from the drill bit) using a grinder. Extruded 4 mil brown Teflon® tape (obtained from Grainger Inc.) was applied to the aluminum plate and any air bubbles were removed by hand before pressing the cut glass stub into the tape covering the hole to first weaken the tape and make sure it covered the edges of the hole completely. The glass stub was removed, and the tape was cut away from the hole with a razor blade. Cool grease thermal paste was applied to the bottom of the hole and the glass piece was fitted into the hole, held in place by the paste. The final product is shown in Figure 37.

B.5-Reactive Ion Etching of the Metal Masked Silica Sample

Recipe	RIE (W)	ICP (W)	Gas 1(sccm)	Gas 2(sccm)	Gas 3(sccm)	Pressure(mT)
De-scum	40	100	O_2=50	N/A	N/A	25
Etching	75	300	Ar=75	SF_6=25	CHF_3=25	15

Table 4. De-scum and etching recipes for metal masked silica surfaces attached to Teflon coated aluminum sample holder

The RIE procedure and recipes were also adapted from Kawata et al.,[124] although RIE power, inductively coupled plasma (ICP) power and etching times given here were determined experimentally using our etching equipment. The sample was affixed to the glass stub on the RIE sample holder using Cool Grease™ thermal paste. The sample holder was fixed to the RIE platen using the same thermal paste and the platen was placed in a Trion Mini-Lock II reactive ion etcher. A de-scum recipe was performed for 30 seconds once the etching chamber had pumped down and the RIE recipe was used to etch the silica surface immediately after. The recipes used for the de-scum and RIE processes can be found in Table 1.

The advantage of using the Teflon® coated sample holder was etching could be performed without the need of a switching process to introduce etching and passivation gases. Argon and the etch gases, SF_6 and CHF_3, were introduced to the chamber simultaneously. The recipe gas flowrates and power settings and etch time were kept constant for each sample respectively, but the etch time was varied between 30 seconds and 2 minutes to vary the etch depth between samples.

After the time had elapsed the sample was removed from the chamber and placed in toluene to remove the thermal paste and then the metal mask was removed using CR 9051 chrome etchant (obtained from Transene Co.), at 50 °C. The sample was immersed in the etchant overnight and then moved to a room temperature water bath to stop the etching process before a final rinse using a water stream and then drying under a nitrogen stream.

B.6-Pillar Fabrication Step-by-Step Results

B.6.1-Sphere Deposition

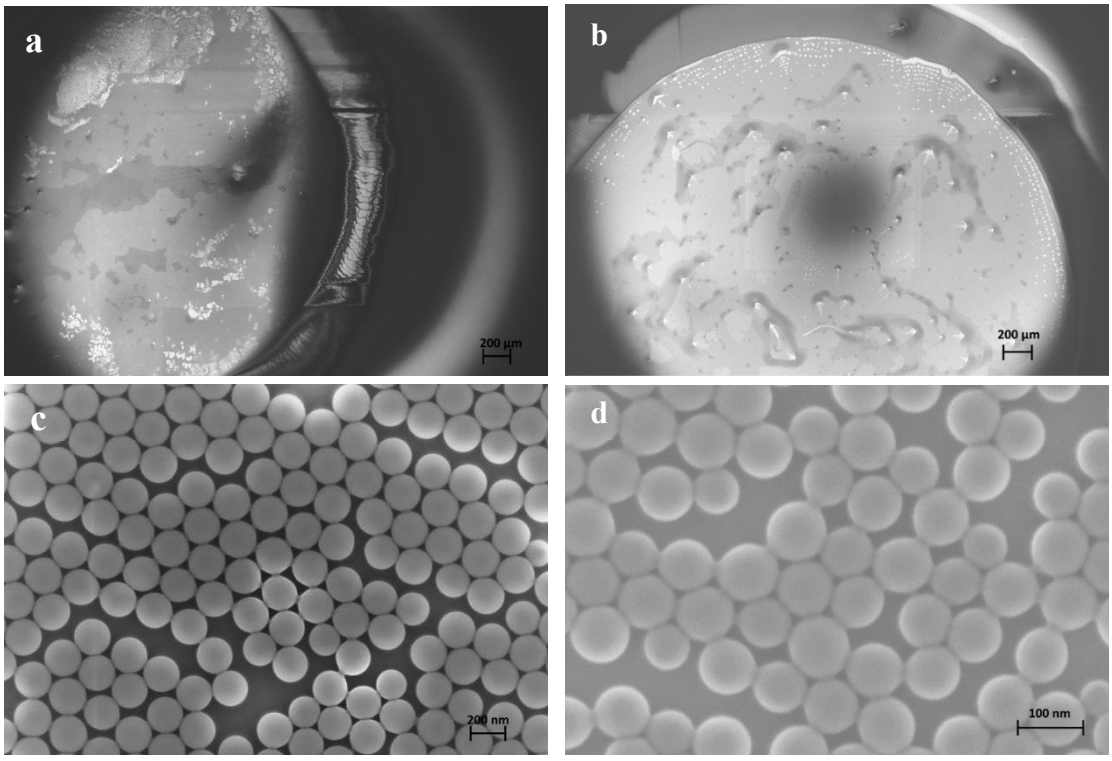

Figure 38. Low magnification micrograph of silica surface layered with 200 nm and 100 nm polystyrene nanospheres (a and b, respectively). High magnification micrograph of patch of single layer of 200 nm and 100 nm nanospheres (c and d, respectively).

The bead layer resulting from using the hydrophobic confinement technique with 200 nm and 100 nm nanospheres are shown in Figure 38a and Figure 38b, respectively. These are low magnification SEM micrographs, displaying a ring of material around an area of mono- and multi-layer polystyrene nanospheres on the respective samples. The lightest colored areas (~10% of the surface within the ring) are those of silica not covered with spheres while the lightest grey areas (~80% of the surface within the ring) have a sphere monolayer. Areas with the even darker shading (~10% of the surface within) are those with 2 or more layers of spheres.

The micrographs in Figure 38c and Figure 38d are high magnification images of the same surfaces with their respective nanosphere sizes and are representative of the appearance of the nanosphere monolayers found on each surface. Although the layers are disconnected in areas, with slightly less connectivity between the 100 nm spheres, each surface still has significant hexagonal packing present, which was all that was necessary for the formation of the apertures used as the metal deposition mask.

B.6.2-Sphere Heating

Heating caused the apertures between hexagonally packed spheres to become circular as the spheres grew larger in the direction parallel to the surface plane, as shown in Figure 39. The apertures had diameters between 20 nm and 40 nm for the 200 nm spheres and between 12 nm and 20 nm for the 100 nm spheres. Varying aperture size indicates the oven provided non-uniform heating of the sphere layer and there may have also been a gradient effect caused by sphere patches with different configurations (spheres on the

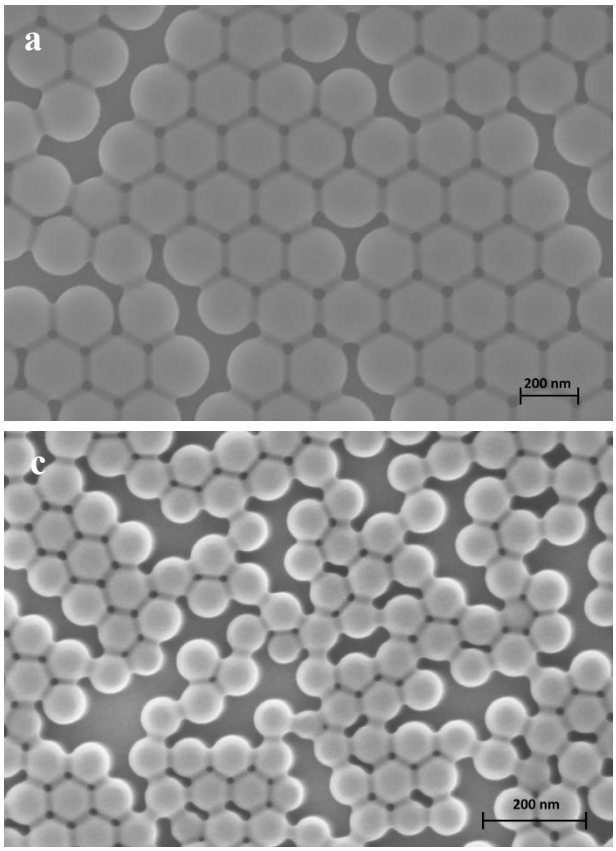

Figure 39. (a) Monolayer of 200 nm nanospheres on silica surface post heating in oven for 2 hours at 160°C. (b)

outer edge of a patch heating differently than those in the center). The presence of various aperture sizes was beneficial to these experiments (variation in final confinement dimensions) but if the need arose it has been shown in the literature that the use of microwave pulses has led to more a uniform and precise reduction of aperture sizes.[125]

B.6.3-Chrome Deposition and PS Sphere Removal

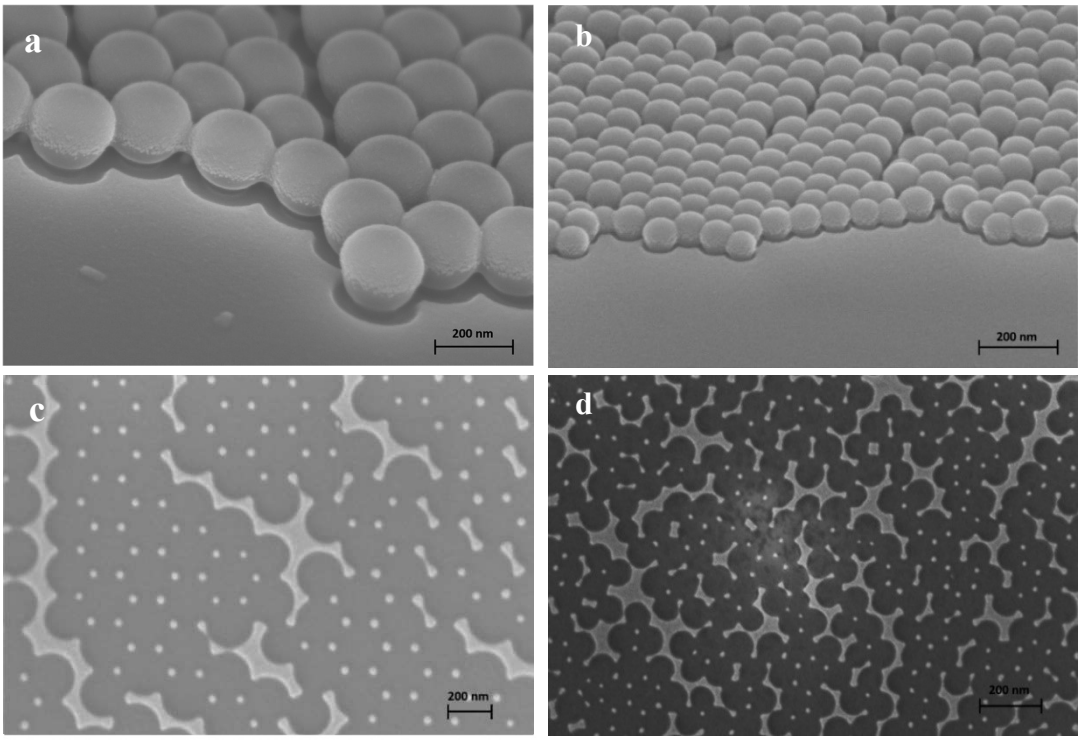

Figure 40. SEM micrograph of (a) 200 nm nanosphere and (b) 100 nm nanosphere layers covered in chrome post evaporation. There is metal into the interstitial spaces between the beads. The resulting metal dots serving as the etching mask post nanosphere removal in toluene (c is 200 nm nanosphere sample and d is 100 nm nanosphere sample.

SEM micrographs showing the results of the metal mask application and sphere removal are shown Figure 40. Due to the directionality of the thermal evaporation the metal coated only the upper half of the spheres and the unmasked silica (upper micrographs in Figure 40). Toluene sonication was able to effectively remove the spheres while leaving the secondary chrome mask on the surface for RIE (lower

micrographs in Figure 40). This secondary mask displayed chrome dots with sharp interfaces at the silica surface with the dots arranged in the expected hexagonal pattern. There were also areas of metal lace (large, connected metal islands resulting from the open areas between sphere patches) and other larger areas of metal where the silica was not covered by spheres. Some areas which were covered by multilayers spheres also had chrome dots, but they were not the clean circular dots obtained in areas covered by a monolayer.

B.6.4-Teflon ® Covered Aluminum Sample Holder Results

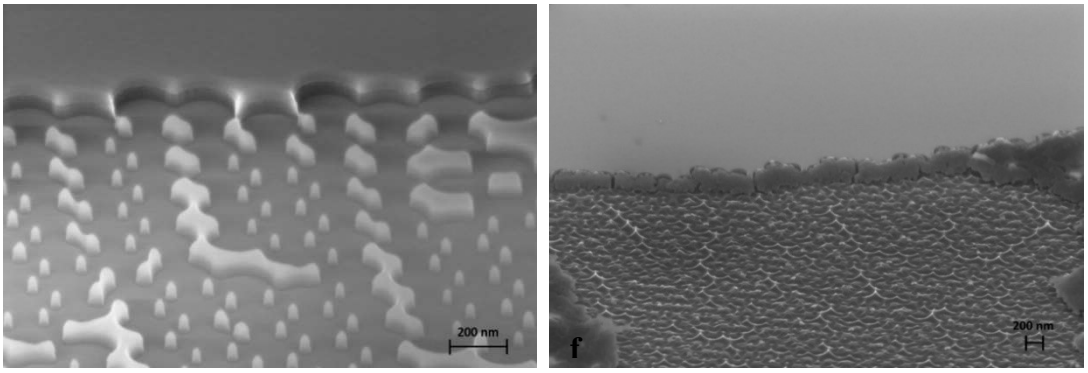

Figure 41. Silica surface masked by chrome post etching with (left) and without (right) the Teflon® covered sample holder.

A single silica surface masked by chrome dots was cleaved in half and the two resulting surfaces underwent the same RIE etching procedure for 30 seconds, in two separate etching trials, but one surface was placed on the glass stub on the Teflon® coated sample holder while the other was placed directly on the etcher platen. The results of this experiment are in Figure 41 and show that the surface produced using the passivating sample holder (left micrograph in Figure 41) has pillar and plateau features one would expect from a vertical etch while the surface etched directly on the platen (right micrograph in Figure 41) has features that have been etched down to small

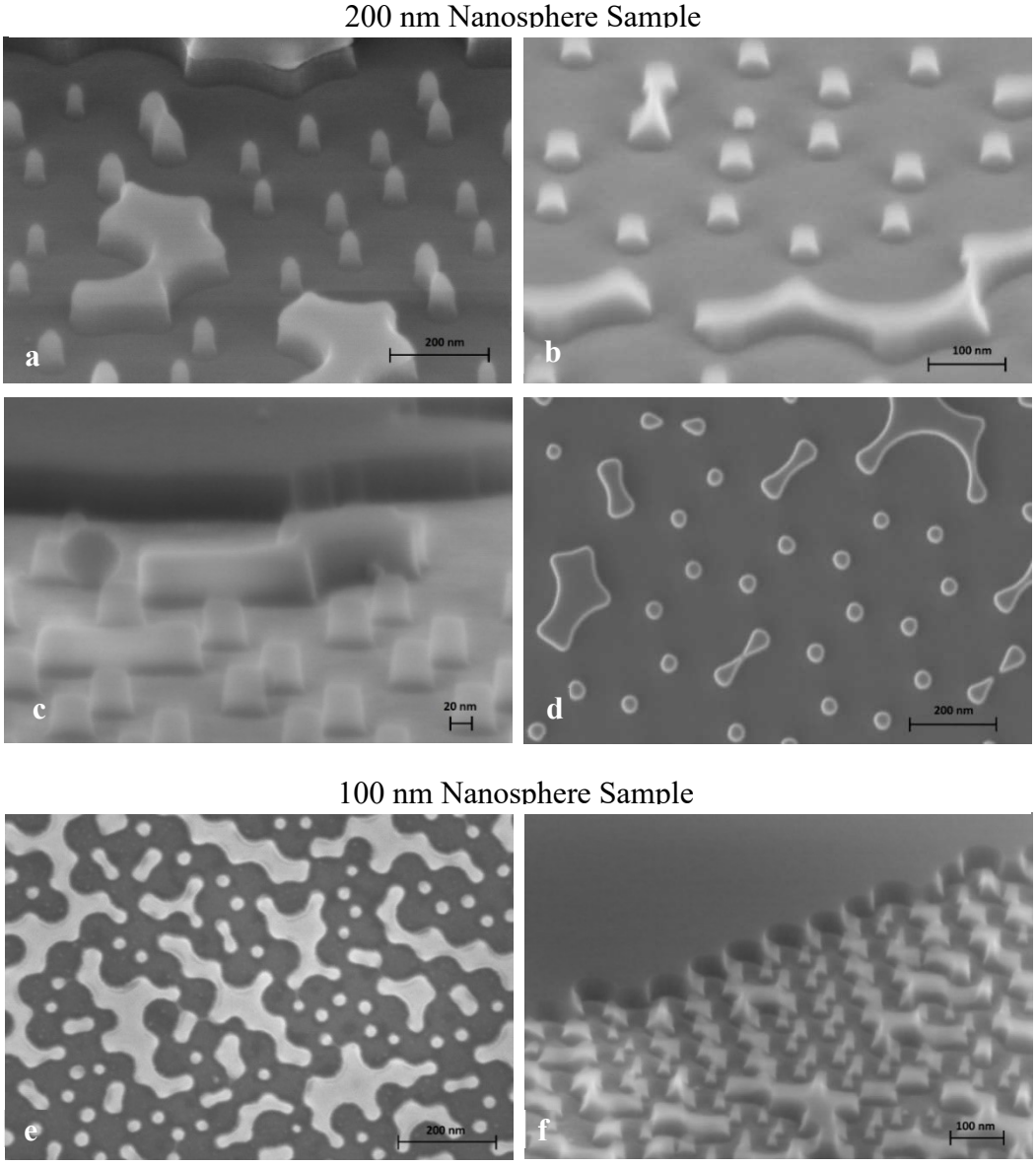

Figure 42. 200 nm Nanosphere Sample: (a) Metal masked silica surface post RIE. (b) Silica surface after exposure to CR9051 metal etchant overnight. (c) Silica pillars side on showing vertical sidewalls (d) Plan view of nanostructures 100 nm Nanosphere Sample: (e) Plan view of metal masked silica surface post RIE. (f) Silica surface after exposure to CR9051 metal etchant overnight

pointed cones. This comparison demonstrates the quality of structures that can be produced using this simple sample holder which is able to achieve the similar effects as a gas switching process. The Teflon® coated aluminum plate was employed to

fabricate all the samples used in this work, without ever having to replace the Teflon® tape.

B.6.5-Metal Mask Removal and Pillar Characterization

Nanostructures resulting from 30 seconds of RIE are shown in Figure 42. The chrome mask is still in place in Figure 42a (200 nm nanospheres) and Figure 42e (100 nm nanospheres), which gives the upper surfaces a rounded appearance. The CR9051 etchant was used to remove the mask, after which flat upper surfaces were obtained, shown in Figure 42b and Figure 42c using 200 nm nanospheres and Figure 42f using 100 nm nanospheres, which also shows the vertical side walls, indicating a mostly anisotropic etch. The plan views in Figure 42d and e show pillars with diameters between 15 nm and 35 nm for the 200 nm nanosphere sample and between 20 and 40 nm for the 100 nm nanosphere sample. From the height of the structures, ~45 nm, the etch rate was found to be 1.5 nm/sec.

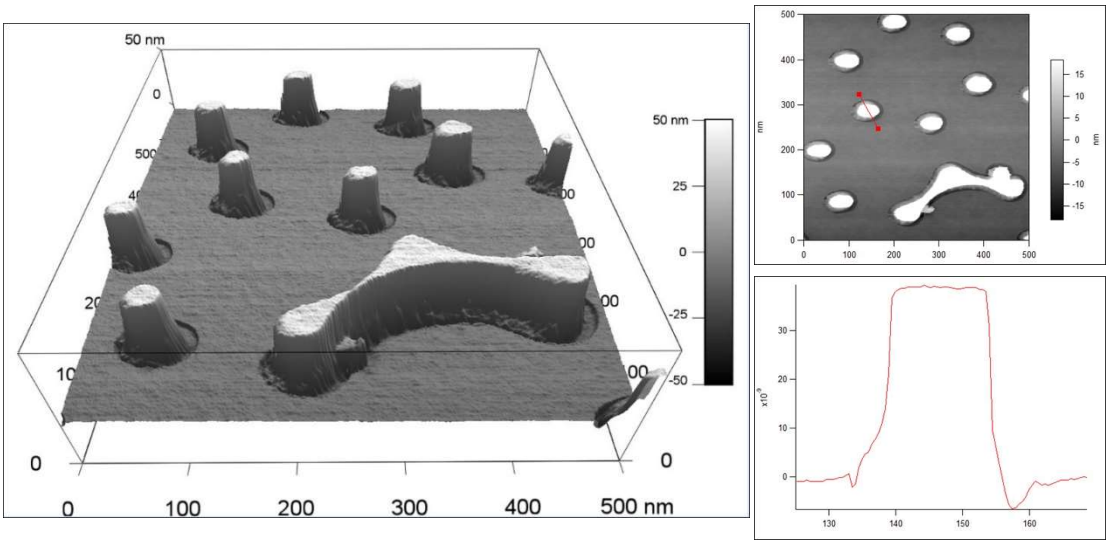

Figure 43. AFM characterization of nanostructures. 3D rendering and line profile confirm vertical sidewalls and heights from SEM.

The results in Figure 43 show a 3D rendering of a surface covered with nanostructures, a 500 nm×500 nm section of the same sample, and a line profile of a pillar. These images support the conclusions drawn from SEM micrographs regarding the vertical nature of the pillar sidewalls as well as showing a flat upper pillar surface. The left edge of the pillars shown in the 3D rendering show an image artifact caused by the shape of the tip used to image the pillars. A measurement made using the line profile from where the upper surface meets the sidewall showed an upper surface diameter of 14 nm, although there is most likely some convolution of this measurement by the AFM tip. Similar measurements made from different sections of the same sample revealed dimensions as large as 35 nm, which agrees with the measurements taken from SEM micrographs.

The nanostructures shown here, and others produced using the same procedure, were used to characterize surfactant adsorbed under lateral confinement, induced on the upper surfaces of the nanostructures via the structure edges. Break-through force maps

for several different nanostructures are shown below, demonstrating the same edge effects were obtained, even with varying shapes and sizes.

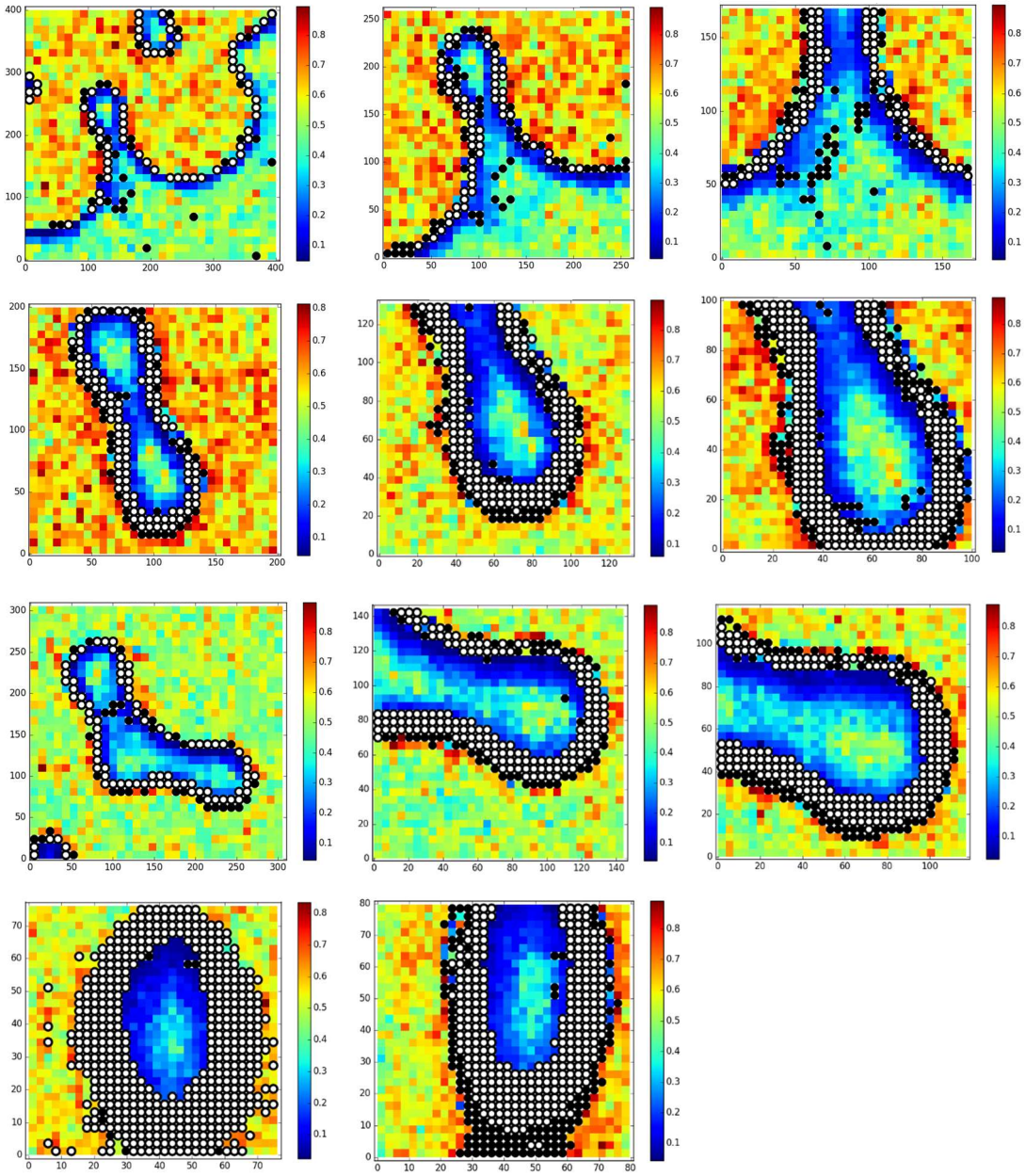

Figure 44. AFM Break-through force map on nanostructures of various shapes and sizes. White circles are edge point and black circles are indices where a value could not be measured (either due to an error or edge proximity).

B.6.6 Second Pillar Sample and Data

A second pillar sample and tip were characterized with 10×CMC of TTAB to confirm the trends observed as a function of distance to the nearest edge. The results are shown below using break-through force maps.

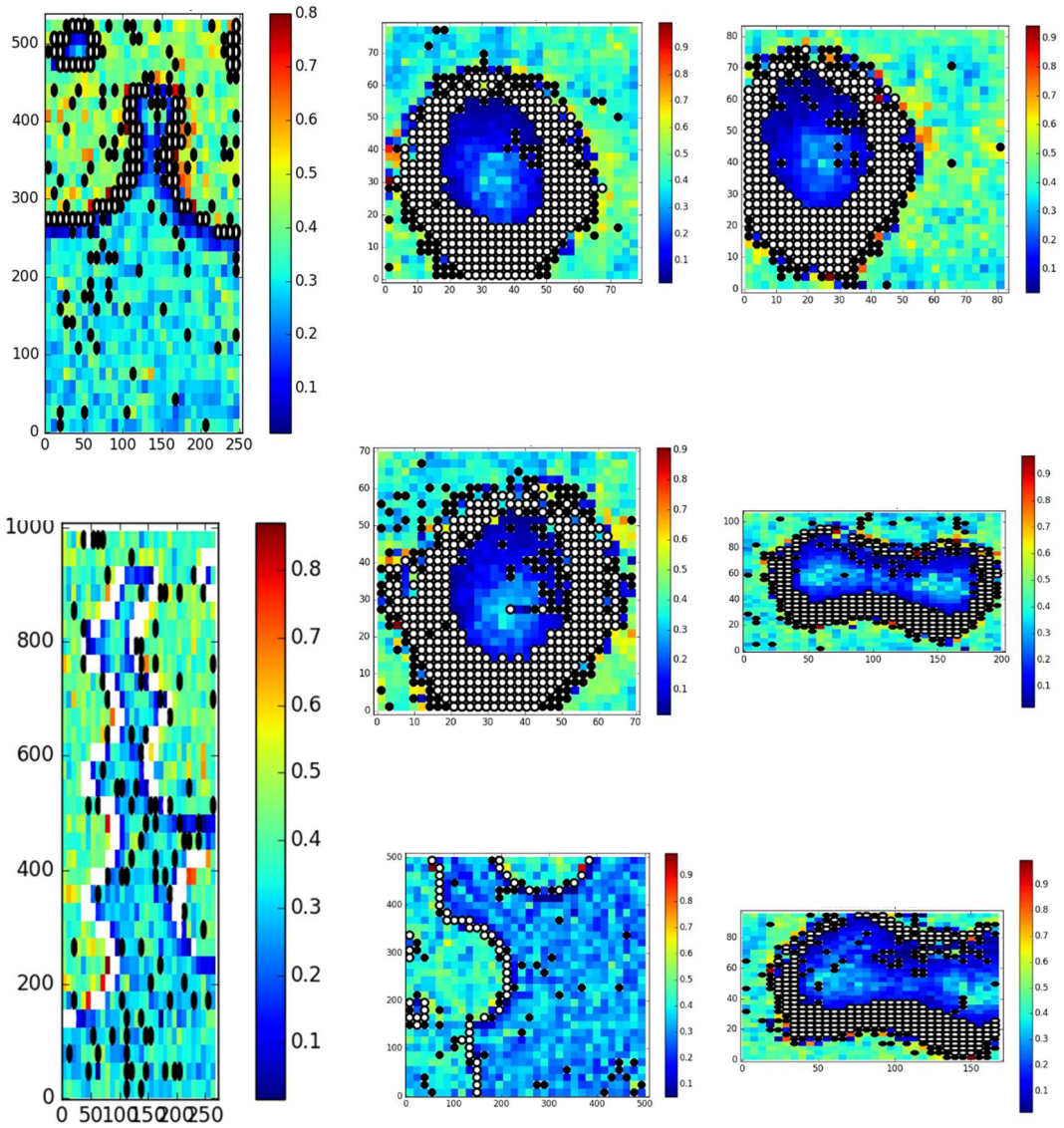

Figure 45. Break-through force maps collected on a second pillar sample and a second high-aspect ratio AFM probe.

The maps shown in Figure 45 show the same trend of decreasing break-through force with increasing distance to the nearest edge as was found on the first sample. The same method of determining the distance to the nearest edge was used and the break-through event values were plotted against distance and are shown in Figure 46.

The results of the exponential equation fitting, using the increasing and decreasing forms presented in section 3.5 of the main text, are shown as the solid black line, where the values of C, τ and A for break-through distance were found to be 1.08±0.304 nm, 8.35±2.86 nm and 3.06±0.0154 nm, respectively. The values for the break-through force fitting parameters were 0.368±0.00581 nN for C and 11.5±2.04 nm for τ. Lastly, the parameters for adhesion force were 0.327±0.00260 nN for C and 14.5±1.15 nm for τ. The τ value for this second sample are slightly lower than the first sample, between 3 nm and 4 nm for all break-through events, which could be a function of the tip shape at a

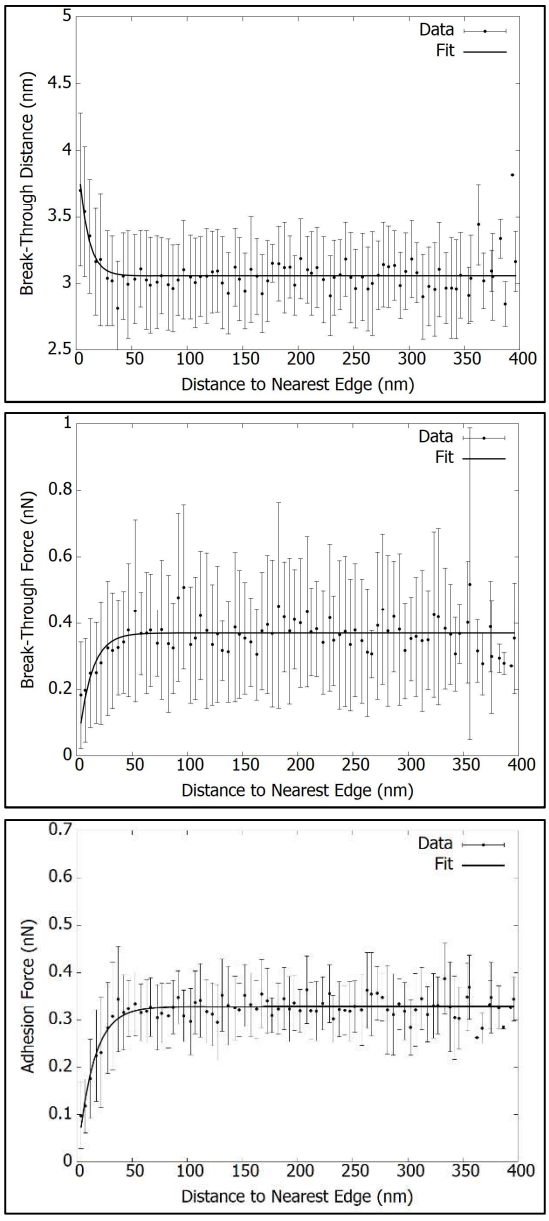

Figure 46. Break-through event values vs distance from nearest edge collected on a second sample and using a second high-aspect ratio AFM tip at 10×CMC TTAB

nanoscopic level or perhaps slight variations of the edge shapes between samples that decreased the distance over which the edge effects extend.

The former is possible because two different AFM tips were used between the two characterization sessions and we have showed that slight variations in tips can cause a difference in break-through force and adhesion force values. However, due to the size of the tips (~20 nm diameter of curvature as verified by SEM and shown in Figure 47) the distance over which the distance effects extend are larger than the diameter at the very tip (more than twice this value on the first sample) and therefore the tip size may have a slight effect but, in our opinion, does not call into question the source of the edge effects but only suggests what is already know: that AFM tip sizes can convolute data to a certain extent and accounting for the tip size can increase measurement accuracy.

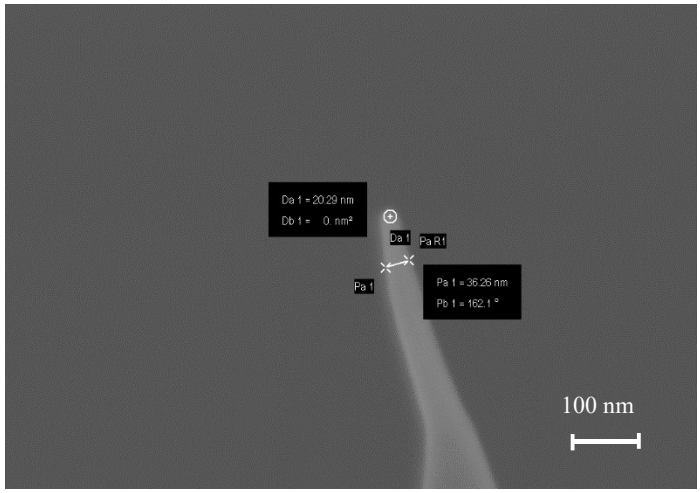

Figure 47. SEM image of high aspect-ratio AFM tip and annotated circle with comparable radius of curvature of the AFM tip (radius=10.145 nm)

As for the second possibility related to the angle of the edge, these samples were two halves of a larger sample and were therefore fabricated under the exact same conditions, and therefore the latter possibility seems unlikely. That said, a more in-depth investigation into the response of these values for edges with different angles between the side wall and upper pillar surface would help to clear up the issue.

In either case, however, the trend with decreasing distance from an edge was the same for both samples. Again, it was found that as distance from the nearest edge decreased the break-through distance values increased, indicating an extended hemifused layer, while the break-through force and adhesion force values decreased, which suggests a decrease in packing or stability.

B.6.7-Longer Etching Times and Pillar Bending

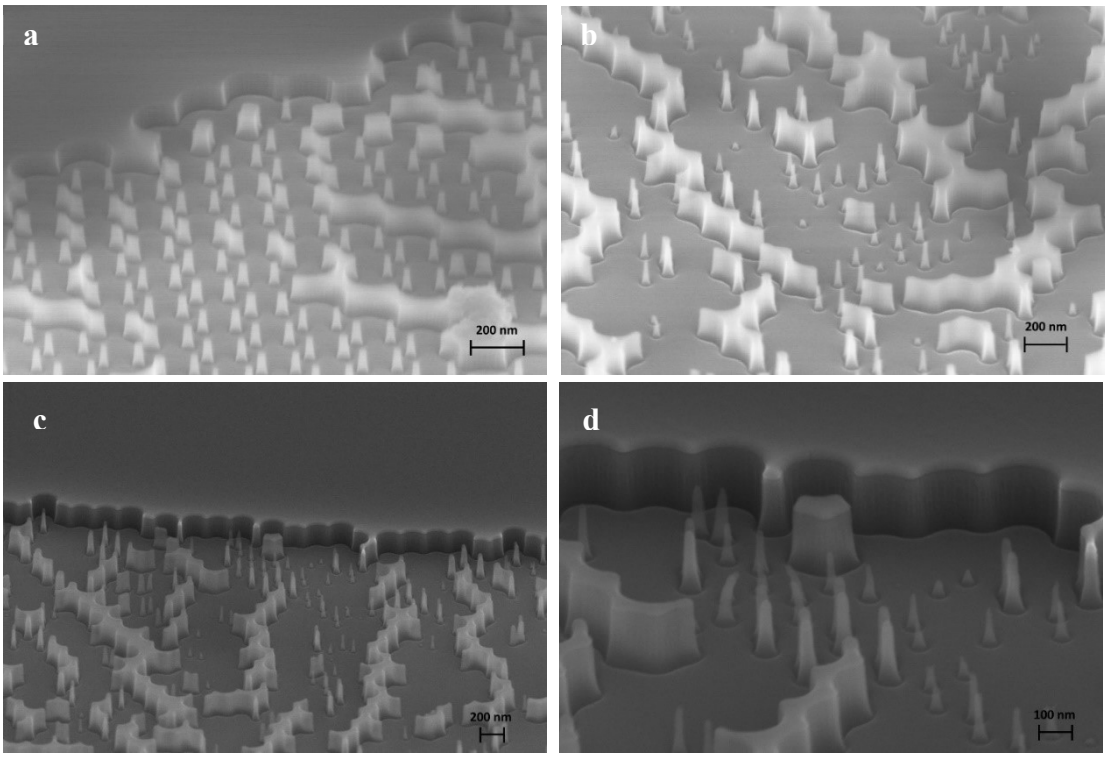

Figure 48. 200 nm nanosphere sample after (a) Sixty second RIE, (b) 90 second RIE and (c and d) 120 second RIE. The micrograph in (d) also shows pillar bending caused by SEM scanning.

The structures in Figure 48 are the result of RIE for 60-120 seconds on a silica surface where the primary mask was 200 nm nanospheres. The structures still have their metal mask in these images but have clean sidewalls with a slight slope (wider at the base than the top). Using the height of the plateaus the etch rate of the silica was found to be roughly 1.5 nm/sec, the same as that found for the 30 second etch, indicating etch times longer than 30 seconds did not affect the etch rate. It was noted that the number of

pillars on the surface is decreased as the etch rate was increased, most likely due to etching of the chrome masks. A slight dip in the surface between the open silica floor and a surface feature side wall suggests faster etching occurs on sloped surfaces not protected by the mask or at the very least at the intersection between the etched floor and a sidewall.

Another interesting note is the deformation of the pillars during electron microscopy imaging, shown in Figure 48d. The pillars in the upper left of the figure were vertical until a reduced size SEM scan was performed there for image focusing. After the larger size scan was resumed it was found that the pillars had bent inwards towards one another. The cause of this phenomena is unknown but might be related to the bending induced when EBD produced platinum nano-rods are deformed through high temperature annealing.[126,127] Although interesting the cause of the bending was deemed outside the scope of this research.

Appendix C: How QCM Works

The QCM sensor is made of a thin quartz crystal coated with the desired surface such as gold, silica, HOPG, metals, polymers, and many others.[128] The quartz is piezoelectric, which means that it will expand and contract very quickly when an electric current is applied, causing the crystal to oscillate. The oscillation frequency and amplitude can be measured to determine if the mass applied to the crystal is changing, such as if a surfactant is adsorbing or desorbing to the surface. If the mass on the crystal increases (due to surfactant adsorption) the frequency will decrease, and amplitude will increase while if the mass on the surface decreases (due to surfactant desorption) the frequency will increase, and the amplitude will decrease.

QCM can also be used to monitor the viscoelastic characteristics of the adsorbed film by measuring a property known as dissipation, D. Dissipation is often described using the equations below

$$D = \frac{E_{dissipate}}{2 * \pi * E_{stored}} = \frac{1}{\pi * f * \tau}$$

Equation 4. QCM Crystal Dissipation

$$U(t) = A_o e^{-t/\tau} * \sin(2 * \pi * f * t + \varphi)$$

Equation 5. QCM Oscillation Decay

where $E_{dissipated}$ and E_{stored} are the energy dissipated by the crystal-film system and the energy stored by the crystal-film system during one oscillation period, *f* is the frequency of the oscillation and τ is the decay time constant.[64,129] To measure dissipation the circuit providing the quartz crystal with current is opened briefly, causing the crystal oscillation to stop oscillating. The oscillations dampen out through energy loss to the film and the surroundings and the resulting signal is fit to Equation 5,
where A_0 is the amplitude at time=0 and φ is the phase. [129]

The faster the dissipation occurs (smaller τ) the more viscoelastic the response and the larger the dissipation value.

$$\Delta m = -\frac{C * \Delta f}{n}$$ **Equation 6. Sauerbrey Equation**

If the adsorbed material is rigidly bound to the substrate, meaning there is a small dissipation, there is a linear relationship between the change in frequency and the mass adsorbed to the crystal, given in the Sauerbrey equation

where Δm is the change in areal mass (mass per unit area), C is a constant with value of -17.7 ng·cm^{-2}·Hz^{-1} for AT cut crystals with a nominal frequency (f^0) of 5 MHz, and n is the overtone number (1,3,5,7,9,11, or 13).[64] The overtone numbers are related to the frequencies achieved by the oscillating crystal, such as a note played on an instrument will also have overtones. The fundamental frequency is at overtone n=0 while higher frequencies are at n=3,5,7… etc. The frequency of each overtone is found by multiplying the overtone number by the fundamental frequency, e.g. for an f^0 of 5MHz the n=3 overtone will have a frequency of 15 MHz, the n=5 will have a frequency of 25 MHz, and so on. The higher frequencies are useful for a few different reasons, the first being that higher frequencies probe farther above the crystal surface, which helps to investigate different heights above the crystal. Higher overtones are also less prone to noise and are more often used for analysis that the fundamental frequency.[128]

However, the film adsorbed to the crystal is not always rigidly bound to the surface. Long surfactants, surfactants that form loose aggregates, or solutions with high viscoelasticity can have large dissipations and in these cases the frequency change does not scale linearly with the overtone number[15]. Using the Saurebrey equation with highly viscoelastic films will lead to overestimated surfactant film masses.[64] In these instances,

a multivariable viscoelastic model such as the Voigt model must be used.[130] Estimates of the film thickness, density and viscosity are input into the model and the data from various overtones are used to determine the correct mass of the film on the surface.

Appendix D: How Atomic Force Microscopy Works

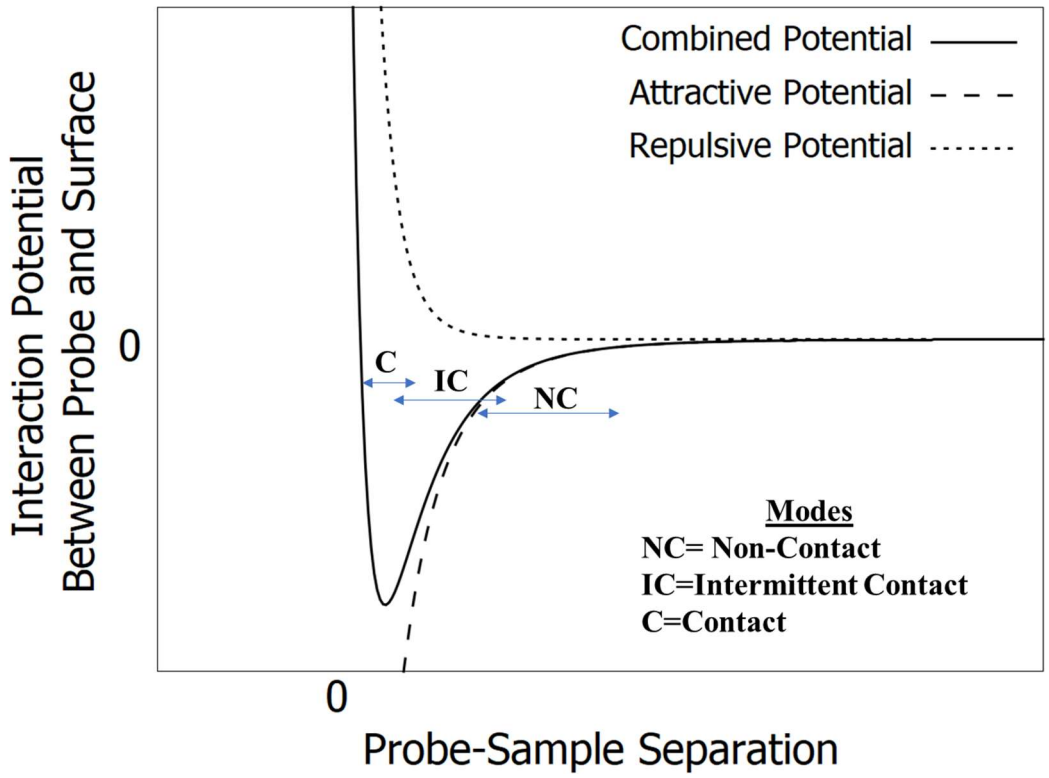

Figure 49. Interaction potential between two atoms and the regions of the curve utilized in the different AFM imaging modes

When two atoms (one on an AFM tip and one on a surface, for instance) are brought close together in air (separation of a few nanometers or less) there will be an interaction potential between them, demonstrated in Figure 49. The potentials in this figure were generated using the Lennard-Jones potential equation, given in Equation 7.[131]

$$U(r) = 4 * \varepsilon * \left(\left(\frac{\sigma}{r}\right)^{12} - \left(\frac{\sigma}{r}\right)^{6}\right)$$

Equation 7. Lennard-Jones Interaction Potential

Force = $\frac{d}{dx}\left(U(r)\right) = -\frac{24*\varepsilon}{r} * \left(2 * \left(\frac{\sigma}{r}\right)^{12} - \left(\frac{\sigma}{r}\right)^{6}\right)$ **Equation 8. Force Between Two Atoms**

The interaction potential is the more common way AFM and force interactions in air are described but the force equation can be obtained by taking the derivative of the interaction potential, given in Equation 8. This force has both attractive (Van der Waals) and repulsive (Pauli exclusion) portions. AFM takes advantage of this force by using piezoelectric micromanipulators to position the tip/cantilever assembly (hereafter referred to as the probe) within a few nanometers above a surface desired to be characterized. The probe is then moved in the x and y directions over the surface and changes in the surface topography will push or pull the tip, which turn will deflect (bend) the cantilever (e.g. increases in surface feature height bend the cantilever upwards and decreases bend the cantilever downwards). The cantilever deflection is measured by positioning a laser on the backside of the cantilever and registering the distance the reflected laser moves using a photodetector. Tip shape and dimensions can be very important in AFM because the tip size typically limits the size of the surfaces features which can be imaged while the tip shape can distort the surface features in the scanned image.

In liquid, the imaging mode are the same but there are other forces that may need to be addressed, especially if surfactant or charged species are present. In this case the tip and surface are treated as one would approaching colloidal surfaces. The attractive force is still the Van der Waals force but now the repulsive force may now arise from the 'electrical double layer' (EDL).[23,132] The force interactions involving

$$Force/Radius = 128\pi c k_B T \kappa^{-1} \tanh\left(\frac{e\psi_0}{4k_B T}\right) e^{-\kappa D} - A_H/6D^2$$

Equation 9. DLVO Force Between Sphere and Plate Normalized by Radius

EDL are well described using DLVO theory and the equation for the force between a sphere (often used to model an AFM tip) and a flat plate is given in Equation 9,

where Radius is the radius of the AFM tip, k_B is the Boltzmann constant (1.38×10^{23}), T is the temperature, c is the concentration of the surfactant or charged species, κ^{-1} is the Debye screening length, ψ_0 is the surface potential, *e* is the electronic charge (charge of the surfactant headgroup or other ionic species) and A_H is the Hamaker constant (dependent on the materials of the two approaching surfaces).[77] This all that will be covered on DLVO theory in this text but if the reader is interested they are referred to the chapter on colloidal interactions in Berg et al and the works of Paria et al.[1,7] The three main AFM imaging modes are non-contact, intermittent contact and contact. Each mode accesses a different region of the potential curve between two objects or surfaces, demonstrated in Figure 49. The first two modes, non-contact and intermittent contact, are achieved by oscillating the tip with a specific frequency and amplitude. To accomplish this, the probe is first 'tuned' by oscillating the AFM head (to which the probe is attached) at a range of frequencies and recording the resulting probe oscillation amplitude and phase. The resonant frequency (f_0) of the probe is found where the phase between the head and probe are approximately zero, which is also where the amplitude in the probe oscillation amplitude will be a maximum. A very good explanation of this process is given by Haugstad et al.[133]

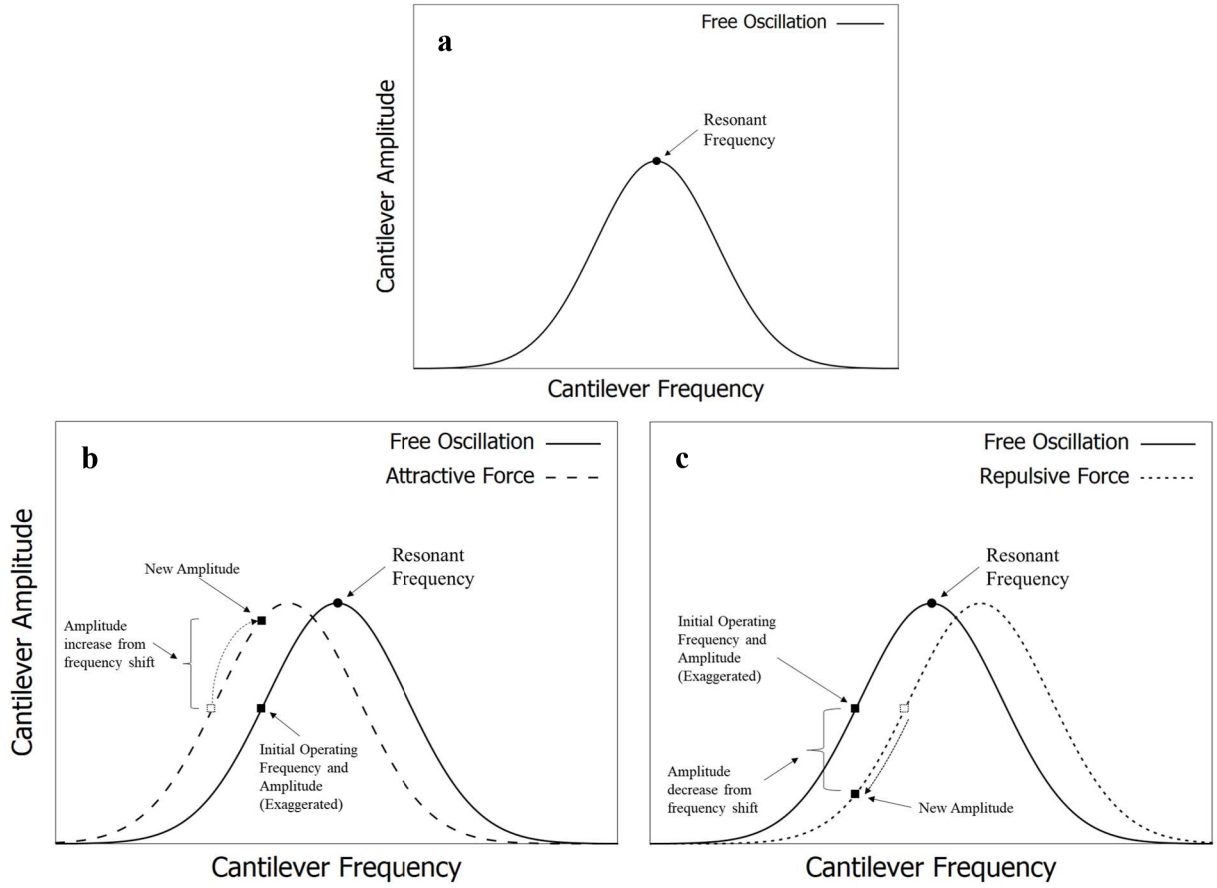

Figure 50. (a) Measured cantilever oscillation amplitude at different driving cantilever oscillation frequencies, annotated with resonant frequency (f_0). (b) Measured cantilever oscillation amplitude at different driving cantilever oscillation frequencies under attractive force. Square denotes setpoint frequency. (c) Measured cantilever oscillation amplitude at different driving cantilever oscillation frequencies under repulsive force.

Once f_0 is known, the operating frequency of the probe can be set to be either above, at, or below this frequency. Setting the operating frequency above or below f_0 (usually a few hundred Hz) will result in a decrease in the oscillation amplitude as you move farther from the maximum in either direction. However, if the operating frequency is set below f_0 then the phase of the probe oscillation will increase, while setting the operating frequency above f_0 will move towards a lower phase value.

Therefore, by choosing the operating frequency above or below f_0 will determine whether the AFM is operating in non-contact or intermittent contact mode, respectively. In non-contact mode the probe will only access the first part of the force curve and therefore will not touch the surface. In intermittent contact mode the probe will have access to the first two regions of the force curve, contacting the surface only briefly at the bottom of each oscillation of the probe.

Once the mode is chosen, setting the operating frequency will determine the probe 'free amplitude' which is the amplitude the probe achieves without interaction with forces from the surface. As the probe gets closer to the surface the amplitude will increase slightly due to the initial attractive forces from the surface pulling the probe downwards (analogously increasing the mass of the probe leading to a decrease in oscillation frequency but an increase in amplitude). As the probe is scanned over the surface the surface features increase or decrease the amplitude of the probe oscillation, which, again, is registered by the laser reflected on the backside of the cantilever. The amplitude is normally what is used to set the operating distance between the probe and the surface. If the user increases or decreases the setpoint the AFM head will move the probe away from or closer to the surface. In most cases the largest amplitude available

which still allows for the collection of the desired height information from the surface is chosen because there is less damage to the probe and/or surface. Lastly, the phase of the oscillation can also be used as an imaging tool because the phase will vary based on the material being scanned. It can therefore be used for determining areas on the surface made of or covered with different materials.

The last imaging mode in AFM is contact mode where the tip is initially positioned a specified height, ‘h’, above the surface and the objective is to maintain ‘h’ by moving the AFM head up or down using the AFM piezoelectric manipulators. The surface feature heights are then calculated by determining how far the head had to be moved to maintain ‘h’. Contact mode is simple and is less susceptible to oscillation interference found in non-contact and intermittent contact modes, such as feedback from imaging elastic samples or when imaging in liquids. The drawbacks of contact mode are that the tip is in more or less direct contact with the surface and the action of scanning can damage the tip causing it to change size or shape over time. Tip damage can also occur if the AFM head attempts to move the tip over large height changes over short distances and therefore knowing the relative height of the surface features may help in determining if contact mode should be used. Another drawback is that in normal humidity at atmospheric conditions a meniscus of water can form between the tip and the surface, leading to a decrease in image resolution. Therefore prior to non-contact and intermittent contact modes AFM was typically performed under vacuum to reach atomic resolution.

Another useful aspect of AFM is the ability to collect force curves, which were demonstrated in the main text previously. AFM force curves are collected by lowering

the probe towards a surface at a set speed and recording the deflection (not force) of the cantilever as the tip comes close to and eventually contacts the surface. The AFM head continues to move towards the surface for a set distance and then retracts, while still recording the cantilever deflection, until the tip is removed from the surface and the AFM head returns to its starting height. The cantilever deflection and AFM head height must then be converted into force and tip-sample separation using the AFM probe force constant, which is how much force is takes to deflect the cantilever a certain distance, and the deflection sensitivity, which is the change in voltage registered by the photodetector for a certain distance deflected.

While the force constant is nominally known from the dimensions of the cantilever, it is good practice to measure the force constant prior to using an AFM probe for force measurements. The deflection sensitivity is a property of the cantilever, laser and photodetector and therefore must be measured for each AFM setup used. Most commercial AFM software will have methods for converting raw cantilever deflection/AFM head movement into force vs tip-sample separation (distance) curves. However, the user must provide the measured force constant and deflection sensitivity for accurate conversion and therefore these values must be measured at the time of the force curve collection. For a more thorough explanation of the math required to obtain force and tip-sample separation distance please see the work of Butt et al.[104]